



THE UNIVERSITY *of* EDINBURGH

This thesis has been submitted in fulfilment of the requirements for a postgraduate degree (e.g. PhD, MPhil, DClinPsychol) at the University of Edinburgh. Please note the following terms and conditions of use:

This work is protected by copyright and other intellectual property rights, which are retained by the thesis author, unless otherwise stated.

A copy can be downloaded for personal non-commercial research or study, without prior permission or charge.

This thesis cannot be reproduced or quoted extensively from without first obtaining permission in writing from the author.

The content must not be changed in any way or sold commercially in any format or medium without the formal permission of the author.

When referring to this work, full bibliographic details including the author, title, awarding institution and date of the thesis must be given.

Co-crystallisation of Energetic Materials –
a Step-Change in the Control of Properties
and Performance of Munitions



Hayleigh J. Lloyd
University of Edinburgh

Submitted for the degree of Doctor of Philosophy
September 2016

Abstract

The research described in this thesis seeks to explore a concept that has the potential to make a step-change for the control of the properties of energetic materials (sensitivity, long-term storage, processability, performance, etc.), resulting in safer munitions with enhanced performance. This concept is co-crystallisation and involves crystallisation of the energetic material with one or more molecular components in order to modify the properties of the composition. The concept has been demonstrated in the pharmaceutical sector as a successful means of altering the physical properties of active pharmaceutical ingredients, e.g. solubility, bioavailability, stability to humidity. This project therefore aims to exploit the concepts of crystal engineering and co-crystallisation as applied to selected energetic materials in order to achieve the following objectives: (i) develop an enhanced understanding of how structure influences key properties such as sensitivity, (ii) control the sensitivity of existing, approved energetic materials, and (iii) identify new energetic materials with enhanced properties, e.g. reduced sensitivity, higher performance, and increased thermal stability.

The compound 3,5-nitrotriazolone (NTO) was crystallised with a selection of co-formers to produce salts and co-crystals. The structure properties of these materials were explored using single-crystal and powder X-ray diffraction, and structural features were correlated with properties such as crystal density, difference in pK_a of co-formers, thermal properties, and sensitivity to impact. Detonation velocities of the co-crystals were calculated based on densities, chemical composition, and heats of formation.

Co-former molecules included a series of substituted anilines, substituted pyridines (including 4,4'-bipyridine, 2-pyridone), and substituted triazoles. A co-crystal was formed between NTO and 4,4'-bipyridine on crystallisation from ethanol, whilst a salt was formed when crystallised from water. Upon heating the salt to 50°C, the co-crystal was formed.

Structural differences between the salts formed by NTO with 3,5-DAT and 3,4-DAT were correlated with structural features. 3,5-DAT.NTO is substantially less

impact sensitive than 3,4-DAT.NTO, and this is attributed to the layered structure of 3,5-DAT.NTO. An investigation into triazole-based NTO salts under high pressure was conducted. A new polymorph of 3,5-DAT.NTO was discovered upon increasing the pressure to 2.89 GPa. The high-pressure phase appears to retain the layered structure and remains in this phase up to 5.33 GPa, although it was not recoverable upon decompression to atmospheric pressure. The compression behaviour of the unit cell volume for phase I of 3,5-DAT.NTO has been fitted to a 3rd-order Birch-Murnaghan equation of state (EoS) with $V_0 = 957.7 \text{ \AA}^3$, $B_0 = 8.2 \text{ GPa}$ and $B'_0 = 14.7$. The unit cell was found to be most compressible in the a and c directions. Under high pressure 3,4-DAT.NTO does not give any indication of a phase change occurring up to 6.08 GPa. The coefficients of the 3rd-order Birch-Murnaghan EoS have been determined to be $V_0 = 915.9 \text{ \AA}^3$, $B_0 = 12.6 \text{ GPa}$ and $B'_0 = 6.5$.

Lay Summary

The research described in this thesis seeks to explore a concept that has the potential to make a step-change for the control of the properties of explosives, propellants and pyrotechnics (sensitivity, damage resistance, long-term storage, processability, performance, etc.), resulting in safer munitions with enhanced performance. This concept is co-crystallisation and involves crystallisation of the two or more chemicals into one crystal. The concept has been seen in the pharmaceutical industry as a successful means of altering the physical properties of active pharmaceutical ingredients, e.g. solubility, bioavailability, stability to humidity. This project therefore aims to exploit the concepts of designing explosives crystals to achieve the following objectives: (i) develop an enhanced understanding of how crystal properties influence key properties such as sensitivity, (ii) control the sensitivity of existing, approved explosives, and (iii) identify new explosives with enhanced properties, e.g. reduced sensitivity, higher performance, and increased thermal stability.

The explosive (NTO) was crystallised with a selection of materials to produce salts and co-crystals. The crystal structure properties of these materials were explored using X-ray diffraction methods, and structural features of the crystals were correlated with physical properties such as crystal density, difference in acidity of the two chemicals, thermal properties, and sensitivity to impact. Detonation velocities, a value which determines the “power” of the explosive, was calculated based on densities, chemical composition, and heats of formation.

The first NTO co-crystal was found and reported. Structural differences between the salts formed by NTO with 3,5-DAT and 3,4-DAT were correlated with structural features. 3,5-DAT.NTO is substantially less impact sensitive than 3,4-DAT.NTO, and this is attributed to the layered structure of 3,5-DAT.NTO. An investigation into triazole-based NTO salts under high pressure was conducted. A new polymorph of 3,5-DAT.NTO was discovered upon increasing the pressure to 2.89 GPa. The high-pressure phase appears to retain the layered structure and remains in this phase up to 5.33 GPa, although it was not recoverable upon decompression to atmospheric pressure.

Declaration

I declare that this thesis was written by myself and that the work detailed in this thesis is my own, or I have contributed substantially to such work, except where specific reference is made to the work of another.

Hayleigh Lloyd

Acknowledgements

I would like to thank everyone who helped me in the course of this PhD. *In primis*, Prof. Colin Pulham for being an incredibly supportive, enthusiastic and diligent supervisor.

Prof. Adam Cumming for the boundless useful knowledge and discussions, in particular on energetic materials. Alison Scott for her kind cooperation and input. Dr. Craig Bull for his tolerance and good humour, in addition for helping with neutron experiments at ISIS along with Dr. Nick Funnell. Dr. Annette Kleppe and Dr Chiu Tang for their help with X-ray experiments at ISIS. Dr. Bill proud, Dr. Andy Jardine, Dr. David Williamson and Sue Gymer for their help with all things that go boom.

Dr. Stephen Moggach for his endless encouragement, perseverance and advice. Dr. Carole Morrison for her interesting and heartfelt discussions. Dr. Ruth Doherty for her generous recommendations and guidance.

I would like to thank the Defence Science and Technology Laboratory (DSTL) for providing me with funding for this PhD.

Xiaojiao Liu, Daniel Ward, Rowan Clark, Karl Hope, Adam Michalchuk, Dr. Sumit Konar and Dr. Stuart Kennedy for your invaluable help, unwavering friendship and travel companionship. The remaining members of the Pulham group for a nice working environment. Stephanie Corless, Peter Wheatley and Bronte Richli, for being a pleasure to supervise.

My incredible Grandparents and family who motivate and support me unconditionally. James Brown for his relentless motivational speeches. Dr. Lorna Murray and Mary Healy for all the coffee breaks, fun and friendship. Dr. Eleanor Whitaker and Dr. Joseph van 't Hoff for keeping a smile on my face and for preparing many delicious meals that fed a run-down thesis writer.

This thesis is dedicated to my parents, who are my lasting source of love,
encouragement and motivation.

“Chaos was the law of nature; Order was the dream of man.”

- *Henry Adams*

Contents

Abstract	1
Lay Summary	3
Declaration	4
Acknowledgements	5
Abbreviations	12
Chapter 1	1
Introduction	1
1.1 Energetic materials	1
1.1.1 Definition	1
1.1.2 Background	2
1.1.3 Insensitive Explosives	4
1.1.4 Summary	6
1.2 Crystal Engineering.....	7
1.2.1 Intermolecular Interactions and Hydrogen-Bonding	7
1.2.2 Halogen-Bonding	9
1.2.3 π Interactions	10
1.2.4 Polymorphism	10
1.2.5 Co-crystallisation	11
1.2.5 Co-crystals and Salts in Pharmaceutical	13
1.2.6 Co-crystals and Salts in Energetic Materials	16
1.2.7 Co-crystals and Salts of NTO	20
1.4 Aims	21
1.5 References	22
Chapter 2	28

Experimental Techniques.....	28
2.1 Synthesis of Nitrotriazolone.....	28
2.2 Preparation Routes to Co-crystals.....	28
2.3 Single Crystal and Powder X-ray Diffraction.....	29
2.4 Powder X-ray diffraction	31
2.5 X-ray Sources: Laboratory versus Synchrotron.....	32
2.6 Powder Neutron Diffraction.....	33
2.7 High-pressure X-ray Diffraction – Diamond Anvil Cell	34
2.8 High-pressure Neutron Diffraction – Paris-Edinburgh Cell	37
2.9 Equation of State	38
2.10 Environmental scanning electron microscopy (ESEM).....	39
2.11 Sensitivity Testing.....	40
2.12 Differential Scanning Calorimetry (DSC)	42
2.13 Calculations of Detonation parameters	43
2.14 References	45
Chapter 3	47
Structural Studies of Salts Formed Between Nitrotriazolone and Substituted Aniline and N-Heterocyclic Compounds	47
3.1 Introduction.....	47
3.2 Aims	49
3.3 Experimental	49
3.3.1 Materials.....	49
3.3.2 Powder X-ray Diffraction	50
3.3.3 Single Crystal X-Ray Diffraction	50
3.3.4 Environmental Scanning Electron Microscopy	51
3.3.5 Differential Scanning Calorimetry	51
3.3.6 BAM Fall Hammer	51

3.3.7 Detonation Parameter Calculations.....	52
3.3 Results and Discussion.....	52
3.3.1 Salts formed between NTO and Arylamine	52
3.3.1.1 Asymmetric Units	53
3.3.1.2 Intermolecular Bonding and Structural Arrangements	55
3.3.2 Salts formed between NTO and N-heterocycles.....	59
3.3.2.1 Asymmetric Units	60
3.3.2.1 Intermolecular Bonding and Structural Arrangements	63
3.3.3 Property Testing	70
3.3.4 Trends and Relationships	76
3.4 Conclusions	78
3.5 Suggestions for Further Work.....	79
3.6 Reference.....	80
Chapter 4	82
Structural Studies of Co-crystals Formed by NTO with 4,4'-Bipyridine and 2-Pyridone	82
4.1 Introduction.....	82
4.2 Aims	82
4.3 Experimental	82
4.3.1 Materials.....	82
4.3.2 Powder X-ray Diffraction	83
4.3.3 Single Crystal X-Ray Diffraction	83
4.3.4 DSC.....	83
4.3.5 BAM Hammer.....	84
4.3.6 VoD Calculations	84
4.4 Results and Discussion.....	84
4.4.1 Asymmetric Unit.....	86
4.4.2 Intermolecular Bonding and Structural Arrangements	89

4.4.5 Polymorph Investigation of BiPy.NTO	92
4.4.5.1 Variable Temperature Diffraction Studies - I11, Diamond	93
4.4.6 Properties	94
4.5 Conclusions	98
4.6 Suggestions for Further Work.....	99
4.7 References	99
Chapter 5	101
Structural Studies of Salts Formed Between NTO and 3,5-Diamino-1,2,4-triazole and 3,4-Diamino-1,2,4-triazole	101
5.1. Introduction	101
5.2. Experimental	102
5.2.1. Materials.....	102
5.2.2. Single Crystal X-Ray Diffraction	103
5.2.3. Environmental Scanning Electron Microscopy (ESEM)	103
5.2.4. DSC	104
5.2.5. BAM Hammer.....	104
5.2.6. Calculation of Detonation Velocity	104
5.3 Results and Discussion.....	105
5.3.1 Salt of NTO and 3,5-Diamino-1,2,4-triazole	105
5.3.1.1 Structural Properties of 3,5-Diamino-1,2,4-triazole.NTO	106
5.3.1.2 Physical Properties of 3,5-Diamino-1,2,4-triazole.NTO	112
5.3.2 Salt of NTO and 3,4-Diamino-1,2,4-triazole	116
5.3.2.1 Introduction	116
5.3.2.2 Structural Properties of 3,4-Diamino-1,2,4-triazole.NTO.....	117
5.3.2.3 Physical Properties of 3,4-Diamino-1,2,4-triazole.NTO	126
5.4 Conclusions	129
5.5 Suggestions for Further Work.....	130
5.6 References	132

Chapter 6	134
High-Pressure Structural Studies of 3,4-DATNTO and 3,5-DATNTO.....	134
6.1 Introduction	134
6.1.1 Structure and Polymorphism of 3,4-DAT.NTO and 3,5-DAT.NTO ..	134
6.2 Experimental	135
6.2.1 Materials.....	135
6.2.2 High-Pressure X-ray Powder Diffraction.....	136
6.2.3 High-Pressure Neutron Powder Diffraction.....	137
6.2.4 Ambient-Pressure Single-Crystal X-Ray Diffraction	137
6.3 Results and Discussion.....	138
6.3.1 Compression of the salt 3,5-diamino-1,2,-triazole.NTO.....	138
6.3.2 Compression of the salt 3,4-diamino-1,2,-triazole.NTO.....	144
6.4 Conclusions	148
6.5 Suggestions for Future Work	149
6.6 References	149
Summary	151
Appendices	Error! Bookmark not defined.

Abbreviations

3,4-DAT	3,4-Diamino-1,2,4-triazole
3,5-DAT	3,5-Diamino-1,2,4-triazole
An	Aniline
Ani	p-Anisidine
AP	2-Amino-3-picoline
API	Active Pharmaceutical Ingredient
BiPy	4,4'-Bipyridine
BrPy	3-Bromopyridine
BTF	Benzotrifuroxan
CBZ	Carbamazepine
CIPy	3-Chloropyridine
CSD	Cambridge Structural Database
DAC	Diamond Anvil Cell
DNAN	2,4-Dinitroanisole
DNB	1,3-Dinitrobenzene
DSC	Differential Scanning Calorimetry
ESEM	Environmental Scanning Electron Microscopy
iRDX	Insensitive RDX
MDNT	1-Methyl-3,5-dinitro-1,2,4-triazole
Mel	Melamine
NTO	3-Nitro-1, 2, 4-triazol-5-one
PBX	Polymer Binder Explosives
PE-Cell	Paris-Edinburgh Cell
Pip	Piperazine
PXRD	Powder X-ray Diffraction
Py	Pyridine
PyO	2-Pyridone
TATB	Triaminotrinitrobenzene
TGA	Thermogravimetric Analysis
TNT	Trinitotoluene

Tol

VoD

XRD

p-Toluidine

Velocity of Detonation

X-ray Diffraction

Chapter 1

Introduction

1.1 Energetic materials

1.1.1 Definition

Energetic materials (explosives and propellants) contain stored chemical energy that can be reproducibly and rapidly released in the form of large quantities of heat and gas upon stimuli such as shock and impact. These properties make energetic materials of both industrial and military interest [1]. Initiation and the manner in which energy is released differ between energetic materials. There are three main ways the energy can be released; combustion, deflagration and detonation. Combustion is an exothermic chemical reaction which proceeds sub-sonically, and is often initiated by heat, which raises the temperature of the material, leading to ignition. Deflagration represents a faster rate of burning that results in spark, and a more intense flame. Peak pressures of only a few atmospheres are observed and reaction rates are sub-sonic. Detonation is a violent, supersonic combustion process that is associated with “high explosives”. The rate of reaction results in a shockwave that moves rapidly through the material and which results in decomposition. The shockwave generally proceeds at velocities in the range of 1500 and 9000 ms^{-1} and this speed dictates the rate of decomposition of the material. Two main initiation routes for the onset of detonation are, (i) deflagration to detonation - in which a material is ignited at one end whilst confined in a pipe, and (ii) shock-induced detonation, principally used for the initiation of secondary explosives. In the first instance (i), the material decomposes producing gases that become trapped within the pipe. This causes an increase in pressure at the burning surface, the consequence of which is an increase in the linear burning rate. Eventually the linear burning rate may exceed the velocity of sound and detonation occurs. A high velocity shockwave, produced by primary explosive (mercury(II) fulminate, lead azide, *etc.*), is used to initiate secondary explosives (TNT, RDX, *etc.*). The shockwave causes rapid heating of the sample through adiabatic compression resulting in its very rapid

decomposition and the progression of a self-sustaining supersonic shock-wave through the sample.

1.1.2 Background

Ever since the accidental discovery of black powder in 220 BC by Chinese alchemists, energetic materials have presented a range of challenges. Well-known explosives, such as HMX, RDX and CL-20 (shown in Figure 1.1) have been widely used in military applications, due to their high explosive performance. However, these materials are becoming less attractive on account of the number of incidents involving accidental initiation by shock or impact aboard ships, in storage facilities and in battlefield environments. Thus developments in energetic materials are now focused on the requirements for safer, yet still powerful materials. These are termed “insensitive explosives”.

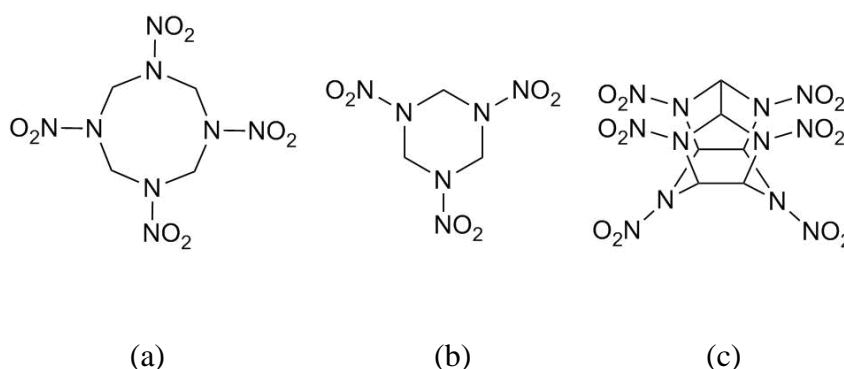


Fig 1.1 Molecular structures of the explosives (a) HMX, (b) RDX and (c) CL-20.

Although energetic materials have been extensively used throughout much of history, the evolution of explosives has been relatively slow. Their first appearance of explosives in the UK was in the form of black powder. This was utilised in mining applications from 1870 onwards and in small guns and hand grenades during the 15th-16th centuries [2]. However, several disastrous explosions occurred and its unreliability in munitions became notorious, thereby limiting applications. Various attempts were made to reduce its sensitivity, such as adding starch, paraffin, *etc.* but these attempts proved to be unsuccessful [2]. The invention of nitroglycerine and nitrocellulose seemed a promising alternative, until they were found to be unsuitable in gaseous coal

mines [3]. Alfred Nobel found the answer to a majority of mining issues by developing both *dynamite* and *blasting gelatine*. Dynamite revolutionised all aspects of the industry, yet it was still inherently hazardous with increasing numbers of accidents involving substantial numbers of casualties. Some governments took action to mitigate these issues and appointed scientists and commissions to investigate better alternatives, most of which were based on ammonium nitrate. Ammonium nitrate was relatively cheap, so the explosives industry added more of it to compositions in order to reduce costs, but at the expense of increased hygroscopicity of the explosive. More recent developments include the use of picric acid and TNT, both of which were replacements for black powder in munitions. Picric acid was not ideal due to its solubility in water, resulting in acidic solutions that corroded metals. This corrosion was undesirable as the resulting picric salts were more sensitive than picric acid, making it less attractive for many applications [4]. To overcome this issue, TNT was developed as an alternative to picric acid. Both molecules are structurally similar, with the replacement of the OH group by a methyl group (Figure 1.2). Initially pure TNT could not be used widely in military applications as there was only a limited production capability due to the availability of starting materials.

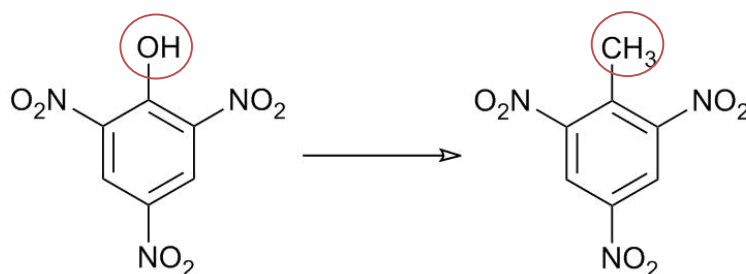


Fig 1.2 Structure of picric acid and TNT, emphasising the altered functional group.

By World War II a new high performance explosive, with reduced sensitivity was required to replace TNT. This came in the form of RDX which has a greater detonation velocity compared to TNT, but a similar sensitivity to impact. Initial difficulties in preparing large amounts of RDX hindered the use of pure RDX in munitions, thus compositions of TNT and RDX with other materials were frequently used [5]. HMX was developed as a more powerful alternative to RDX, although was more expensive to manufacture [6].

After, the demand for safer explosives became apparent once more. The concept of plastic explosives (PBXs) emerged in which the polycrystalline explosive is embedded in a polymer matrix. These polymer binders cushion the crystallites from impact and friction, thereby minimising the likelihood of accidental detonation. Other benefits include better processability and mechanical properties [2].

In 1987 the high density material, CL-20 (hexanitrohexaazaisowurtzitane), was synthesised as part of an investigation into minimising the available space within a crystal structure. Cage nitramines have a significantly greater densities than their ring counterparts. High density is of importance as the detonation velocity of the material is directly proportional to the crystal density [8]. There are a number of disadvantages with CL-20 including its cost of synthesis and sensitivity to stimuli.

Besides high performance, the environmental impact of energetic materials also requires consideration since nitro-based compounds are generally toxic on account of the organo-nitro groups (C-NO₂). To avoid this, nitrogen-rich materials have been developed that can decompose rapidly with the formation of N₂ gas. Examples of such molecules are shown in Figure 1.3.

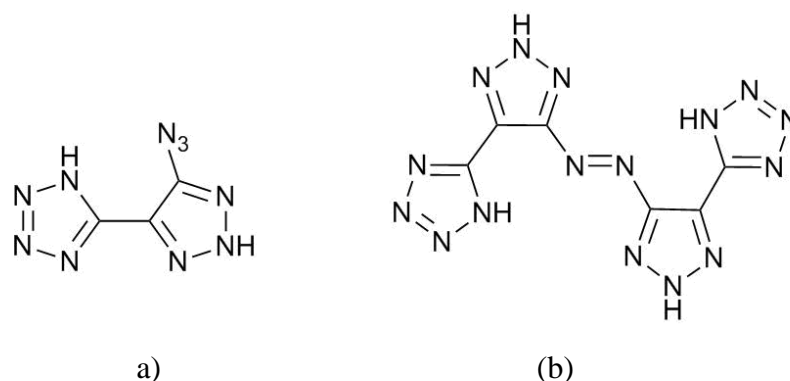


Fig 1.3 Molecular structures of nitrogen-rich energetic materials **(a)** 5-(5-azido-2H-1,2,3-triazol-4-yl)-1H-tetrazole and **(b)** 1,2-bis(4H-tetrazol-5-yl)-2H-1,2,3-triazol-5-yl)diazene [9]

1.1.3 Insensitive Explosives

Another strategy for decreasing the risk of accidental detonation is the development of compounds that are initially less sensitive to initiation. Examples include 2, 4-dinitroanisole (DNAN), triaminotrinitrobenzene (TATB) and nitrotriazolone (NTO),

(Figure 1.4) that have reduced sensitivity due to a large number of reasons [7]. Insensitive munitions (IM), which contain insensitive explosives, are of increasing importance on account of the requirement for increased safety in the storage and development of explosives and propellants that do not sacrifice combat readiness or effectiveness.

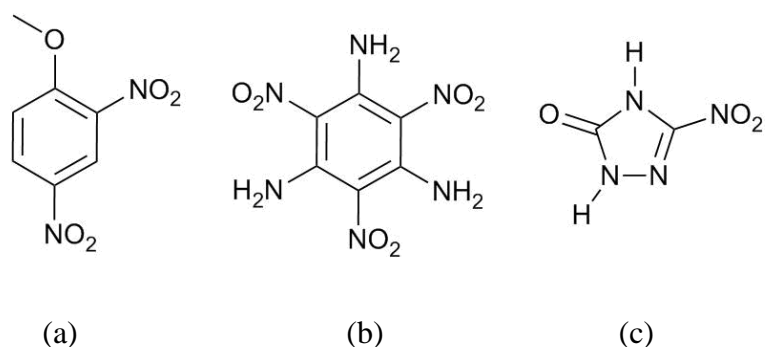


Fig 1.4 Molecular structures of insensitive explosives (a) DNAN, (b) TATB and (c) NTO.

IM-compliant munitions also minimise materials costs and casualties from accidents caused by sympathetic detonation, caused by heat, shock or impact. NTO is currently used in the formulations IMX-101 and IMX-104 with compositions DNAN/NTO/nitroguanidine and DNAN/NTO/RDX, respectively. These are used in artillery projectiles and mortar cartridges in order to improve some properties and reduce costs. NTO is becoming increasingly popular as an ingredient in compositions in order to ensure that their munitions comply with IM requirements.

NTO is a good example of a successful IM. It has a comparable detonation velocity to RDX [10], yet its sensitivity is close to that of TATB in all aspects (electrostatic, friction, impact) [11-13]. NTO can be synthesised in a simple two-step route and can be processed straightforwardly by pressing or casting techniques [14]. In addition, NTO crystallises as only two polymorphs, the α -form and the β -form - the α -form is the more stable of the two under normal conditions [15]. Another benefit include its high thermal stabilities, although its decomposition pathway is unknown, and a consensus has not yet been reached on the initial step of thermal decomposition. Studies of NTO show a maximum, single exothermic peak in the range of 253 - 279 °C, depending on experimental conditions [1,15]. In addition small peaks as high as

335 and 504 °C have been observed [16]. A large volume of gas is produced upon decomposition of NTO, and so it has been investigated for applications such as airbags in automotive vehicles [17]. The main gases evolved during decomposition have been found to include N₂, N₂O, NO and HCN. The majority of the gaseous N₂ evolved is derived from adjacent ring nitrogen atoms (~68 %), with smaller percentages evolved from the nitro-group and the other ring nitrogen atom [18].

However, NTO does possess some disadvantages, and these include, high solubility in water, toxicity and acidic nature. These properties can lead to environmental concerns for aquatic and plant life. Metal salts can easily be formed that could have increased sensitivity. In addition, NTO does not melt before decomposition and so must be added to a molten mixture in order to produce melt cast composition. Although straightforward, the synthetic procedure does not give high yields and so it's expensive and has a low-yield synthesis.

1.1.4 Summary

A major current priority is the development of less sensitive compositions that are less prone to accidental initiation, but which retain explosive performance. Current strategies include the synthesis of new molecules, but this approach is becoming increasingly limited because of the need for cost-effective production methods, extensive validation, and the requirement to meet increasingly challenging performance targets. Another approach is to develop formulations that are physical mixtures or blends of individual energetic components. Polymer binders are also extensively used to reduce sensitivity and serve the purpose of dissipating the energy of impact/friction and reduce the likelihood of initiation *via* hot-spots. It has also been shown that factors such as crystal quality, surface defects, pore collapse, and fracture of crystals all contribute to sensitivity [19]. Hence by paying attention to purity and crystal quality in the production process, materials such as iRDX (insensitive RDX) have been developed, and weapons systems containing this material are much easier to qualify as insensitive munitions. Despite all of these advances, there remains a pressing need to reduce sensitivity still further in order to comply with both current and future legislative needs over the munition's lifetime. At the same time there is a

need to provide the key enabling technology to permit warhead designers to produce novel, high-performance systems with tailored effects, e.g. tuneable blast effects.

1.2 Crystal Engineering

Crystal engineering has been described as the design of a crystal structure with the aim of generating a structure exhibiting a desired property [20, 21]. It is a relatively new branch of chemistry, having only originated in the 1970s and has become increasingly popular over the last 15 years. The first crystallographer to coin the phrase “crystal engineering” was Ray Pepinsky in a 1955 [22]. To understand and create new complexes, the study of similar compounds which display comparable molecular structures is carried out, but this relationship is generally not a simple one. Part of this is the comparison of crystal structures and identifying correlations with their chemical and physical properties in order to recognise the possible cause for these properties [21]. It is believed that supramolecular chemistry and crystal engineering are closely interlinked, as both areas focus on non-covalent bonding, such as intermolecular interactions. However, crystal engineering relates to the supramolecular chemistry of the solid-state [23]. The start of this process is to identify the building blocks of many structures, which were first described by Desiraju as “supramolecular synthons” [24], and hence use them to form a hypothesis for structure formation in the solid state. The understanding of crystal engineering is centred on the observations and links between the intermolecular interactions, the packing of the crystal and the crystal properties [24]. The driving force behind crystal engineering is therefore a knowledge and understanding of intermolecular interactions [25].

1.2.1 Intermolecular Interactions and Hydrogen-Bonding

A wide range of intermolecular interactions have been studied, including van der Waals interactions and halogen bonds [26], but the most studied type is represented by hydrogen bonding, which can be found in purely organic solids.

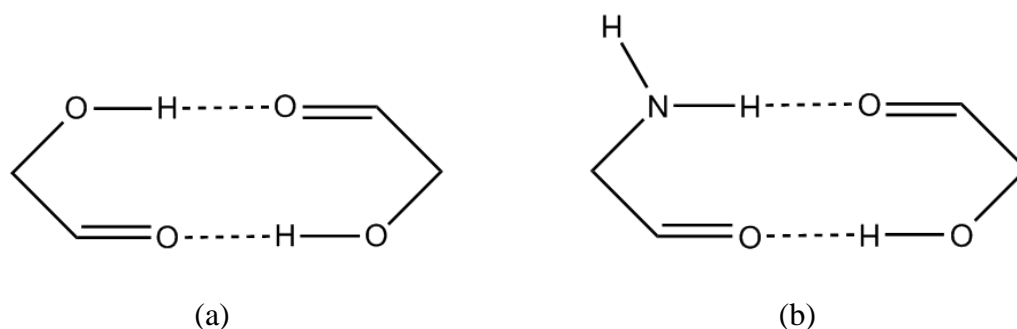


Fig 1.5 (a) A homosynthon, and (b) a heterosynthon both displaying two hydrogen bonds

According to IUPAC, the definition of a hydrogen bond is: “*an attractive interaction between a hydrogen atom from a molecule or a molecular fragment X–H in which X is more electronegative than H, and an atom or a group of atoms in the same or a different molecule, in which there is evidence of bond formation*” [27]. However, it is sometimes difficult to define hydrogen bonds due to their diverse nature. The most valued quality of a hydrogen bond is its directionality and versatility, due to varying bond strength and possible donors and acceptors [25].

Table 1.1 Classes of hydrogen bond for an D–H...A system

	Strong	Moderate	Weak
Interaction	Mostly covalent	Mostly electrostatic	Electrostatic
Bond Lengths	D–H \approx H...A	D–H < H...A	D–H \ll H...A
H...A (Å)	1.2 – 1.5	1.5 – 2.2	2.2 – 3.2
D...A (Å)	2.2 – 2.5	2.5 – 3.2	3.2 – 4.0
Bond Angles (°)	175 – 180	130 – 180	90 – 150
Examples	HF complexes Proton sponges	Acids Alcohols/Amines	C–H...O bonds O–H... π bonds

The strongest hydrogen bonds are unusual in being symmetrical – the hydrogen atom is positioned half way along hydrogen bond between D (donor atom covalently bonded to hydrogen, H) and A (electronegative acceptor atom) and tend to occur in ions. In depth analysis of crystal structures of hydrogen bonded complexes [28] has shown that strong hydrogen bonds can only occur in molecular patterns, which are known as “chemical leitmotifs” [29]. The one of most interest to this report is called the “positive/negative charge-assisted hydrogen bond” [30] and it is the association of acid-base pairs, with matching pK_a that can easily exchange the proton. This produces nearly symmetric and strong $D \cdots H \cdots A$ bonds that are quite rare and which have been studied accurately on relatively a few occasions using neutron diffraction [31].

Most common hydrogen bonds generally fit into the moderate hydrogen bond category and tend to be more asymmetrical. Weak hydrogen bonds are similar to van der Waals’ forces in energies and geometries, yet can be distinguished from them by the directional involvement of the D–H bond [25]

1.2.2 Halogen-Bonding

Halogen bonding is similar to hydrogen bonding in the sense that it involves non-covalent interactions that have high directionality. However, the electron density acceptor in hydrogen bonding, the hydrogen atom, is replaced by a halogen atom, X [32]. This can occur on account of a halogen atom possessing regions of positive electron density (as shown in Figure 1.6), that can interact favourably with electron rich atoms or sites on other molecules. The geometry of these bonds are in the scheme $B \cdots X-Y$, where Y is a nitrogen, carbon or halogen atoms, B is the electron donor and X is the halogen. These interactions are used in crystal engineering as they are ideal crystal packing motifs [32, 33].

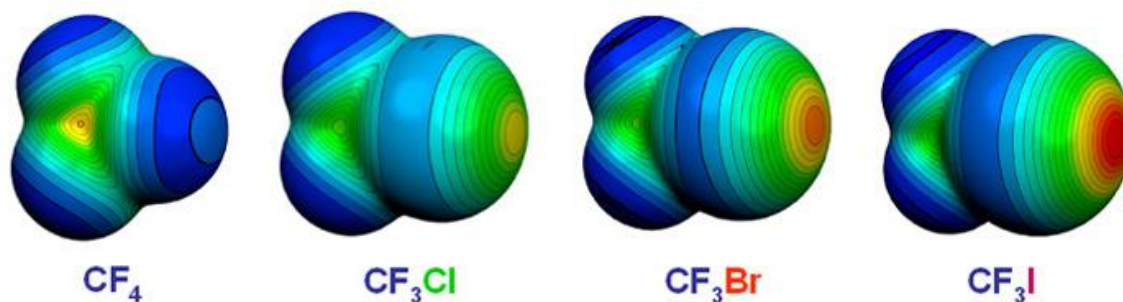


Fig 1.6 Electrostatic potential of molecules, displaying increased positive region with increased halogen size (in Hartrees) [34]

1.2.3 π Interactions

These are relatively weak, attractive interactions involving π electrons. The most common form involves $\pi \cdots \pi$ interactions, between aromatic rings, which can occur in three ways; (i) Sandwich conformation, (ii) T-shaped conformation, or (iii) a conformation in which stack are displaced in parallel [35]. It is also known for cations and hydrogen bonds to form attractive interactions to the face of an electron-rich π -system [36]. Anion $\cdots \pi$ interactions can also occur in supramolecular architectures, to a face of an electron deficient π system [37].

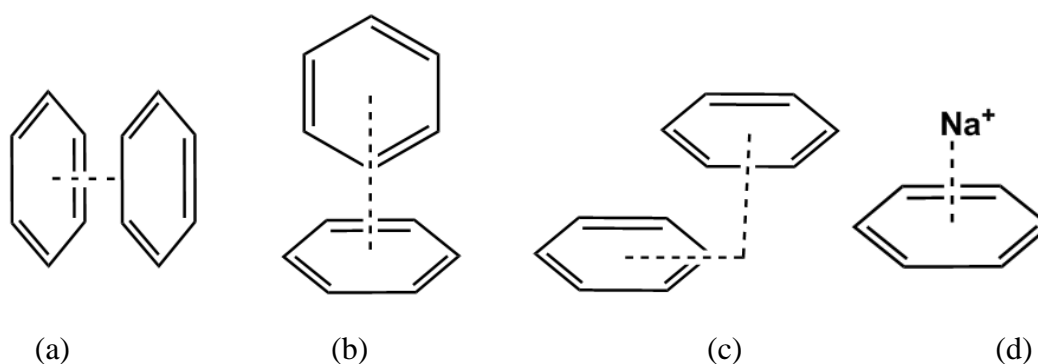


Fig 1.7 (a) Sandwich conformation, (b) T-shaped conformation, (c) parallel displaced conformation and (d) cation-face interactions.

1.2.4 Polymorphism

An important aspect of material property development for application is the investigation of polymorphism. Polymorphs of a material exhibit very different properties, such as solubility, bioavailability and morphology [38, 39]. McCrone stated a definition of polymorphism as “a solid crystalline phase of a given compound

resulting from the possibility of at least two different arrangements of the molecules of that compound in the solid state” [40]. Polymorphism is a very common occurrence which has been known and discussed for a substantial amount of time. The first publication of a polymorph was by Mitscherlich in 1822 [41] investigating a variety of different crystal structures of the same arsenate and phosphate salts. In the pharmaceutical industry, polymorphs of drugs are known as discrete materials that can be patented separately. Furthermore, polymorphism has also been widely studied in a few energetic materials, such as RDX and CL-20 under high pressure [42]. CL-20 exhibits a variety of property differences, such as density, thermal stability and sensitivity, depending on polymorphic form. It has four stable polymorphs; α -, β -, γ -, and ϵ -, which can be obtained via different synthetic methods and high pressure. The ϵ -form being the least sensitive form with the highest density and detonation velocity. [43].

1.2.5 Co-crystallisation

Co-crystals are crystals containing two or more neutral molecular components (co-formers) that rely on non-covalent interactions to form a regular arrangement in the solid state – see Figure 1.8. In contrast a salt is formed when proton transfer occurs between the two components. There has been extensive debate about whether solvates should be included in this category, i.e. where one of the components is liquid under ambient conditions. Herein, solvates are considered as co-crystal or salts, depending on the proton position.

When choosing a co-former several aspects must be taken into consideration in order to make an informed and intelligent estimation of the likelihood of success. A common method for choosing a particular component is synthon matching. This involves understanding what molecular synthons/functional groups produce intermolecular interactions with another group. A method used for pharmaceutical co-crystals is ΔpK_a see scheme 1.1. As a rule, a pair of materials that have a $\Delta pK_a < -1$ will form a co-crystal and $\Delta pK_a > 4$ will be a salt, with an indefinite result between -1 and 4 [44]. Other considerations include solubilities and electron density distribution in the constituent molecules. There are many methods for producing molecular

complexes, these include; melt co-crystallisation; liquid-assisted grinding; hot-stage microscopy; and solution crystallisation (also known as evaporative methods).

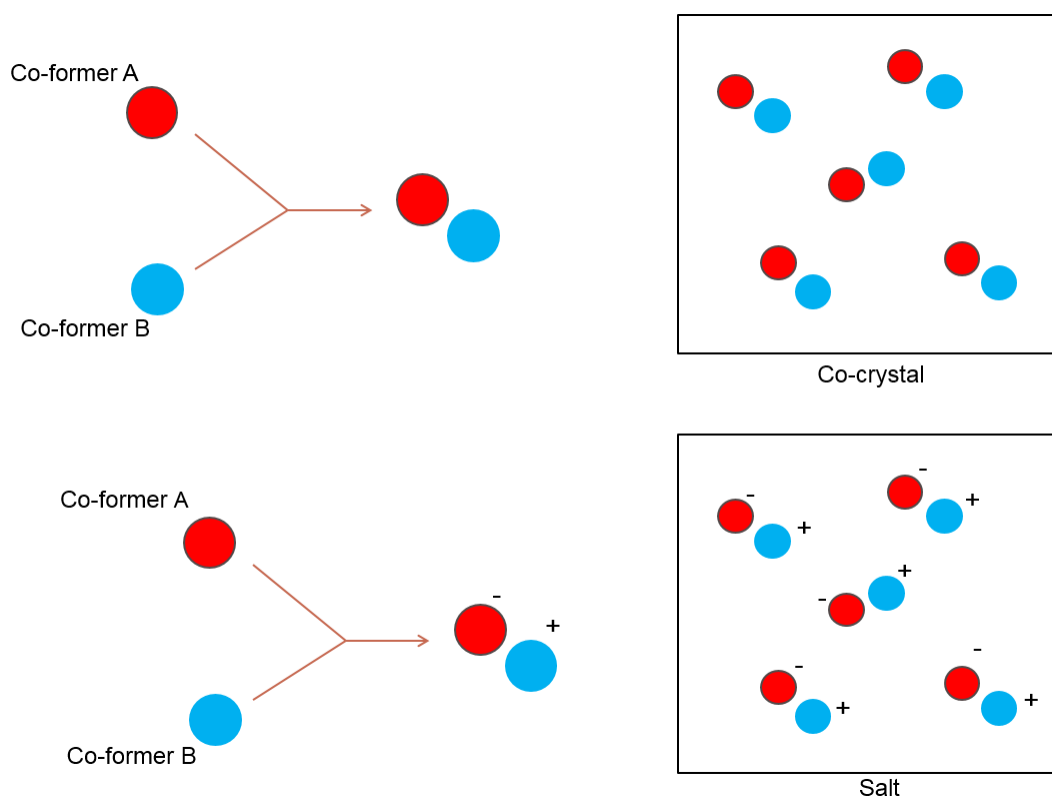
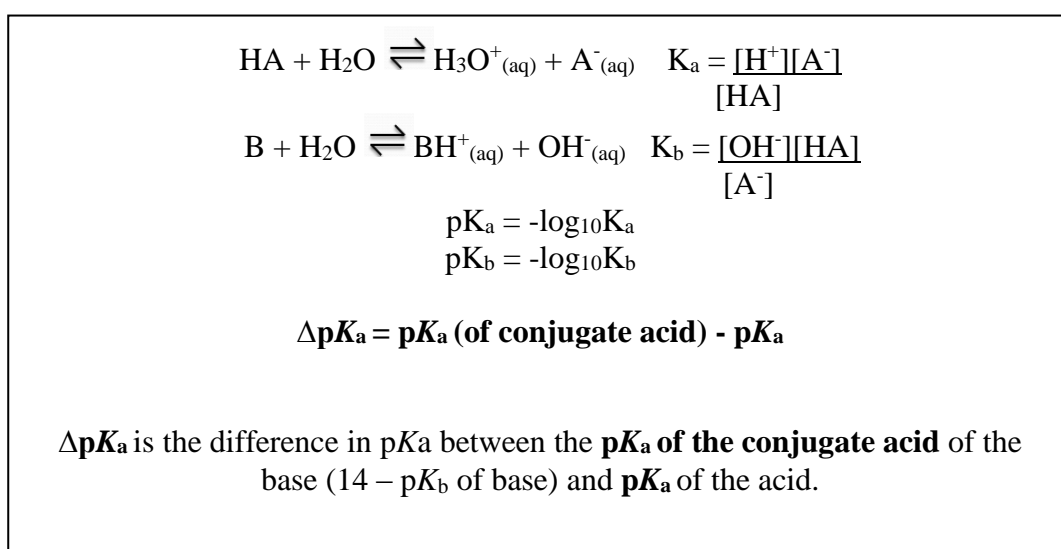


Fig 1.8 Diagram describing the basic concept of salt and co-crystal formation



Scheme 1.1 Equations for ΔpK_a

1.2.5 Co-crystals and Salts in the Pharmaceutical Industry

Co-crystallisation and the formation of salts can dramatically alter the properties of materials, which is why both have been an area heavily studied within the pharmaceutical sector. Active pharmaceutical ingredients (APIs) are generally delivered as solid, powders and are required to have the desired dissolution rate, stability and bioavailability [45,46]. Previous methods for changing such properties consisted of breaking and making covalent bonds in order to produce new compounds but this is a lengthy and costly process, and can affect the pharmacological effects of the drug. Investigations into adjusting the crystalline forms of APIs have become an attractive alternative, but this can also create new problems as multi-component systems do not always display ideal properties. Due to the clinical, legal and regulatory steps that must be taken, all aspects of APIs must be thoroughly explored before being placed on the market, including crystalline forms such as polymorphs and hydrates. This has given the pharmaceutical industry an advantage in understanding intermolecular motifs for designing new complexes. Numerous API salts have been reported and are currently used for common drugs, due to the large numbers of acids and bases suitable for pharmaceutical use [47, 48]. Salts, however, are limited to only acidic or basic APIs. In contrast, co-crystals can address multiple functional groups in a molecule. APIs frequently contain hydrogen-bonding moieties, such as amides, and so it can be relatively easy to form co-crystals. There are numerous examples demonstrating the benefits of co-crystallisation of APIs the main benefit being increased solubility [49-51].

Although there has been extensive research in the co-crystallisation of small organic molecules, it is still not possible to predict whether co-crystallisation will occur. However, a number of trends and rules have been established, that to aid design and reduce the length of the screening process. Primarily, the Cambridge Structural Database (CSD) [52] is utilised for its abundant source of structurally characterised molecular salts and co-crystals. Therefore it is possible to gain an understanding of synthon principles, graph sets and hydrogen bonding rules. One particular hydrogen-bonding rule that has wide applications is that by Etter *et. al.* This states that (i) all good proton donors and acceptors are used in hydrogen-bonding, (ii) six-membered-

ring intramolecular hydrogen bonds form in preference to intermolecular hydrogen bonds, and (iii) the best proton donor and acceptor remaining after intermolecular hydrogen-bond formation will form intermolecular hydrogen bonds to one another [53]. These rules help to overcome the issue of competing hydrogen bond assemblies when using a particular co-former.

As previously mentioned in section 1.2.4, a common rule of thumb involving the acid ionisation constant pK_a , is employed to establish whether a co-crystal or salt might be formed. This pK_a rule states that a salt should be expected when the difference is greater than 4 units, and a co-crystal when the difference is less than -1 [44]. However, proton transfer behaviour has been shown to be influenced by the crystalline environment, temperature, and solvent system so the rule should be treated with caution.

An interesting observation emerging from a database of multi-component systems is the trends in polymorphic behaviour. It has been reported that co-crystals show a greater polymorphic tendency (approximately 55%) than do salts (approximately 39% for salts) [54].

Finally, it is important to understand the comparison between the solubilities of co-formers. As shown in Fig 1.9, co-formers with similar solubilities will lead to the formation of the 1:1 co-crystal from solvent evaporation, whilst for components with differing solubilities it is a much more complicated picture. One approach for the production of a 1:1 co-crystal with components that show different solubilities is to have an excess of the co-former (supersaturated) to drive formation of the co-crystal or to make it the thermodynamically favoured solid phase relative to the components. This can be achieved by an experimental approach involving the evaporation of solutions which the solubilities of the individual co-formers are similar. [55]

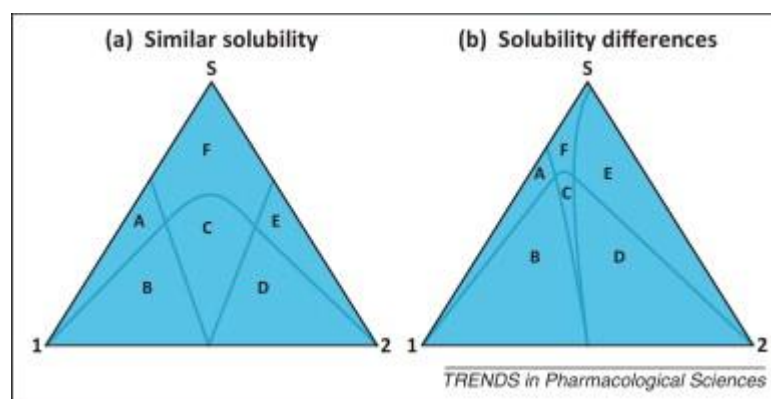


Fig 1.9 Schematic representations of isothermal ternary phase diagrams with (a) similar solubilities between components **1** and **2** in solvent **S** and (b) different solubilities of **1** and **2** in **S**. Region **A**= component **1** and solvent, **B**= component **1** + co-crystal, **C** = co-crystal, **D** = component **2** + co-crystal, **E**= component **2** and solvent, and **F**= solution [54, 55]

There have been many studies to explore how synthons, interaction strengths and packing arrangements have consequently altered physical properties [56, 57]. An example of such is the API, AMG517 which was co-crystallised with a variety of co-formers such as trans-cinnamic acid, glutaric acid and lactic acid; the resulting co-crystals possess vastly different melting points and solubility from the individual components [57]. An additional co-crystal of an API that shows altered physical properties is the carbamazepine (CBZ):saccharin co-crystal (Figure 1.10). Carbamazepine is a widely used drug for the treatment of epilepsy and trigeminal neuralgia, despite its poor dissolution rate and low bioavailability. It has been reported to have five polymorphs, an acetone solvate, a dihydrate and two ammonium salts [58]. Its main source of interaction is *via* its primary amide, a hydrogen bonding group [59]. CBZ exhibits self-complementary nature between the amide groups, making it favourable for co-crystallisation. The properties of the CBZ:Saccharin co-crystal have been studied: no polymorphs have been obtained, there is an increased bioavailability compared to anhydrous CBZ, and the co-crystal has a similar chemical stability to the different forms of CBZ [60]. However, due to the regulatory requirements and extensive trials and testing prior to drug launch very few pharmaceutical co-crystals have reached the market. Examples of marketed pharmaceutical co-crystals are caffeine citrate, for apnoea of prematurity and sodium valproate with valproic acid

(Depakote ®) for treatment of manic episodes associated with bipolar disorder. [61, 62, 63, 64]

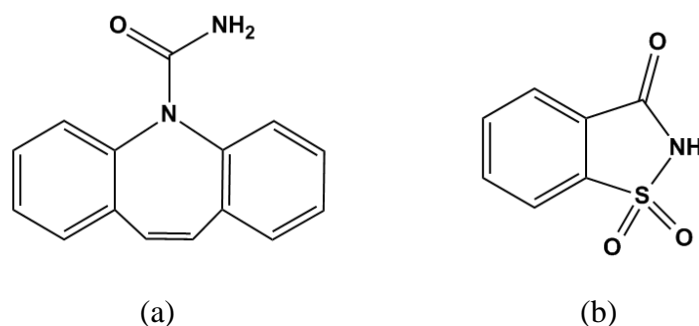


Fig 1.10 Molecular structures of carbamazepine, **a**, and saccharin, **b**.

1.2.6 Co-crystals and Salts in Energetic Materials

In comparison to the pharmaceutical industry, there has been much less research into energetic co-crystals. Hence understanding of structure-property relationships is not well advanced thereby making design and crystal engineering very difficult. Furthermore, the paucity of energetic co-crystals and salts in the CSD, presents problems for further design. However, it is possible to somewhat predict the potential interactions and hydrogen-bonding that can occur between co-formers by transferring rules and principles utilised for organic and pharmaceutical compounds, to energetic materials.

To date, there have been no systematic studies of structure-property relationships in energetic salts and co-crystals. However, there are strong indications that co-crystallisation is a potential method for altering properties, including crystal density and sensitivity to stimuli. Therefore a review of the sparse intermittent research previously reported on organic co-crystals and salts of energetic materials molecular is required. Organic salts and co-crystals of energetic materials typically contain non-energetic co-formers, but in some cases, they have been crystallised with other energetic materials. Both types of co-former have resulted in a variety of altered properties. In some cases co-crystallisation has been detrimental to energetic

performance, but in others it has been improved. Non-energetic co-formers have been studied in order to understand the potential interactions and synthons of conventional energetics. TNT, RDX, HMX and CL-20 have all been co-crystallised with non-energetic molecules. One feature shared between many conventional high explosives, described in Section 1.1, is the nitro functional group. Nitro-groups are rarely seen in pharmaceutical components, on account of the high toxicity. Hence this has caused a gap in our knowledge of potential interactions of nitro-groups with other functional groups. However, $-NO_2$ has been studied as a supramolecular synthon with halogen atoms such as bromine, forming three types of interactions and interesting network architectures [65].

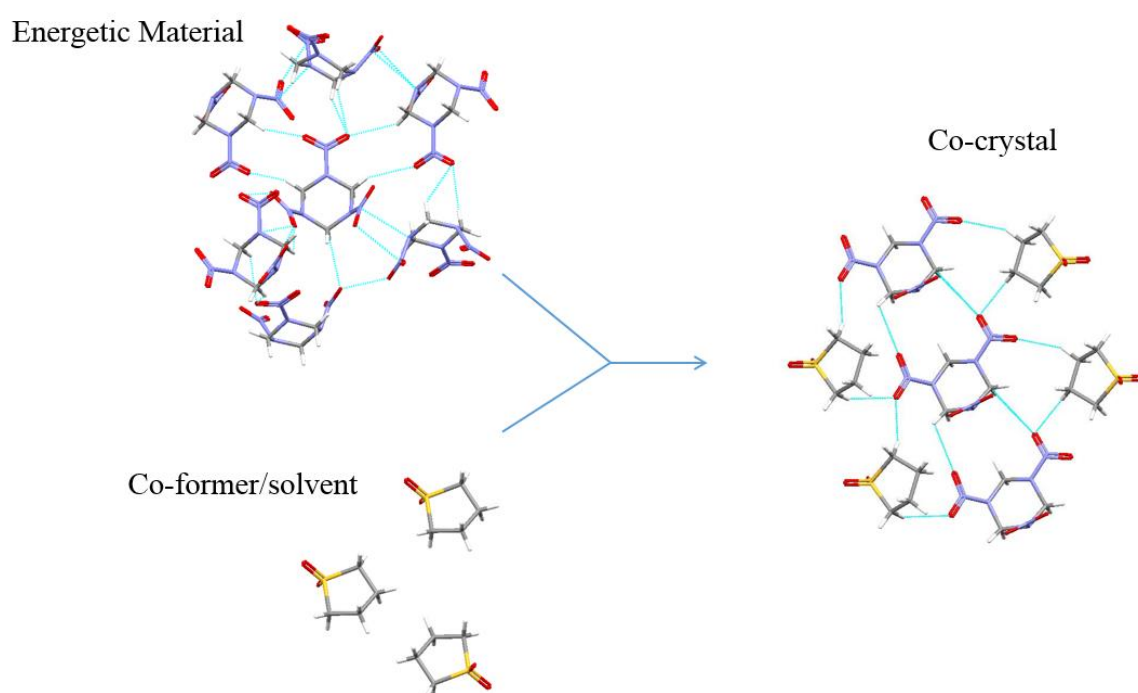


Fig 1.11 An example of an energetic material and co-former resulting in an energetic co-crystal

TNT co-crystals have been reported that contain co-formers such as anthracene, pyrene, phenothiazine and anthranilic acid [66-71]. Within these co-crystals, the electron-rich rings of co-formers interact with electron-poor rings of TNT holding the structure together. It is evident that the π -interactions are vital here, especially given the lack of functional groups for hydrogen bonding. Sparse data has been obtained for the physiochemical properties of these co-crystals, however it has been reported that the

melting point of the resultant co-crystals are different in comparison to TNT. Although the structures and some physical properties have been explored in detail, no relationships between interactions and properties of these co-crystals have been established.

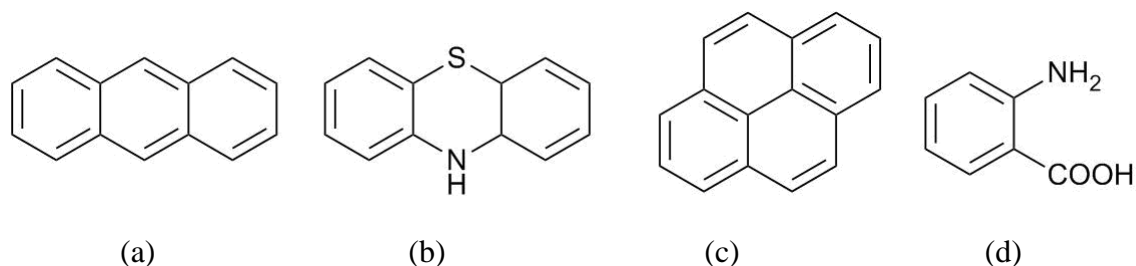


Fig 1.12 Molecular structures of (a) anthracene, (b) phenothiazine, (c) pyrene and (d) anthranilic acid

Some co-crystals exhibit reduced sensitivity to stimuli in comparison to single component. Benzotrifuroxan:1,3-dinitrobenzene (BTF:DNB) is an example of a co-crystal with an altered sensitivity. The sensitivity to impact of 1:1 BTF:DNB lies almost half way between the high power (but sensitive) BTF, and the lower power but insensitive dinitrobenzene, as shown in Figure 1.13 [72]. In contrast, a recent energetic co-crystal of CL-20 and 1-methyl-3,5-dinitro-1,2,4-triazole (MDNT) demonstrates a similar impact sensitivity to CL-20 rather than MDNT (>100 cm) [73]. It is also noteworthy that CL-20:MDNT exhibits a reduced sensitivity to friction.

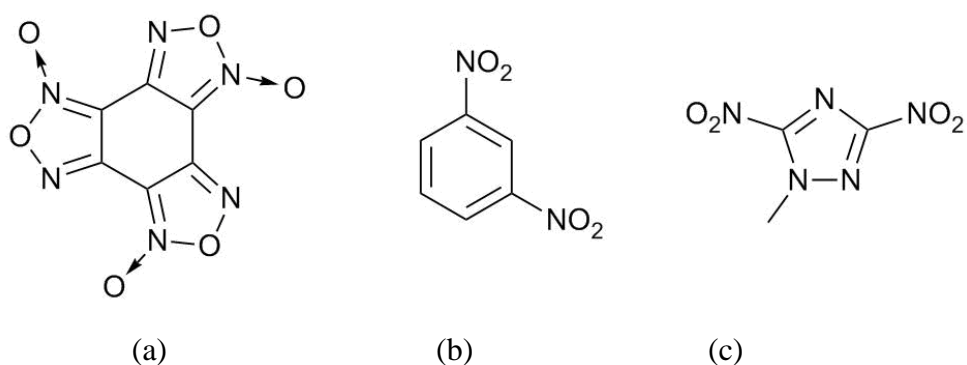


Fig 1.13 Molecular structures of (a) benzotrifuroxan, (b) 1,3-dinitrobenzene and (c) 1-methyl-3,5-dinitro-1,2,4-triazole

Not only is the melting point and sensitivity to stimuli altered when materials are co-crystallised, a range of energetic materials have been reported to exhibit altered crystal density, thermal decomposition, morphology and solubility. An example of a co-crystal which exhibits altered crystal density is CL-20:HMX. CL-20 crystallizes in several polymorphic forms depending on the solvent and conditions of crystallization. The densities of these polymorphs range from 1.92 to 2.04 g/cm³ [74, 75]. It is a very powerful explosive, however, its relatively high sensitivity makes it less than ideal for many applications. The 2:1 co-crystal CL-20/HMX was discovered with the aim of maintaining the high detonation velocity of CL-20 whilst incorporating the lower sensitivity of HMX. The co-crystal retains a relatively high calculated detonation velocity (9484 m/s) which sits midway between those of the two co-formers. The co-crystal was also shown to have a reduced sensitivity to impact compared to ϵ -CL-20 [76].

A possible real-world application of energetic co-crystals is that as a safe transportable material which can be manipulated to retrieve pure starting components. This material is described as a “smart material” which was coined by Matzger in recent papers, in which insensitivity co-crystals can be “activated” by heat to retrieve a certain co-former [77] TNT/CL-20 was reported to be a potential smart material with decreased sensitivity in comparison to CL-20. At 136 °C the TNT within the co-crystal melts to a liquid and produces either the β -form or γ -form of CL-20. The co-crystal cannot be recrystallized once the mixture is cooled. Therefore, impact insensitive TNT/CL-20 can be easily converted, through heating, into sensitive CL-20 when required. For a more in depth review of energetic co-crystals the reader is guided to Lloyd, NTREM conference paper 2015 [78].

It is clear that a proof of principle has been obtained and that co-crystallisation is an interesting method for altering physical and chemical properties of energetic materials. Hence, the work present herein is a systematic study of NTO crystallised with a range of co-formers with the aim of identifying and rationalising structure-property relationships.

Other well-known explosives (that have previously been mentioned Section 1.1, Figure 1.3) such as TATB and NTO have no reported co-crystals, and few organic salts, whilst DNAN only has one with 18-crown-6 [79]. TATB self-assembles to

produce a network of very strong hydrogen bonds; this is ideal for reducing the material's sensitivity and increasing stability, yet makes it very difficult to dissolve in solvents and hence it is not a good candidate for co-crystallisation. NTO is of interest due to its slightly acidic nature (pK_a 3.67) that is essential for making salts. It is nitrogen rich and contains additional functional groups suitable for forming interactions, such as hydrogen bonding.

1.2.7 Co-crystals and Salts of NTO

Firstly, NTO is slightly acidic in nature (pK_a 3.67) [12] possessing two ionisable hydrogen sites, which is essential for making salts and secondly it is soluble in water, ideal for evaporative crystallisation. In addition it is nitrogen rich and contains other functional groups suitable for interactions such as hydrogen bonding.

Currently there are no NTO co-crystals reported in the literature, but numerous salts of NTO have been described. The majority of these are contain metal elements and compounds, although ~ 24 organic salts have been reported. Interestingly, many of these organic salts have thermal decomposition data have been reported but structural information is sparse. NTO salts that have been reported for which both structural and thermolysis data are available includes: hydrazine (HNTO), ammonia (ANTO), ethylenediamine (ENTO), guanidine (GuNTO), aminoguanidine (AGuNTO), diaminoguanidine (DAGuNTO), and triaminoguanidine (TAGuNTO) . They were all characterised using ^{13}C NMR and IR spectroscopy with subsequent studies by single-crystal X-ray diffraction (XRD) [80-85]. The common feature of these salts is that the co-formers contain primary amines. Structural determination of these salts show that N(2) of the NTO deprotonate, in line with this being the more acidic hydrogen compared to the hydrogen on N(3) readily, whilst a primary amine on the amino co-former was protonated. This is the only trend identified in interactions between these salts, so no structure-property relationships have been established. ANTO and ENTO appeared to exhibit enough potential to be considered for use as explosives, yet it was concluded that they, along with similar non-energetic amine salts, did not qualify as primary explosives [86].

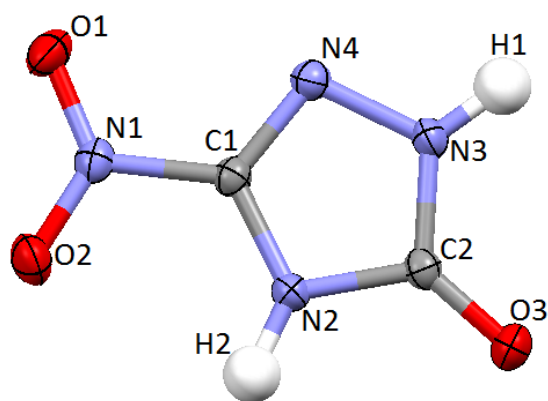


Fig 1.14 Labelled molecular structure of NTO

Other interesting amino-based salts of NTO that have also been well characterised are dimethylamine (DMNTO), 3,3-dinitroazetidine (DNAZNTO), and 2-azidoethylamine (AANTO) [87-90]. Dimethylamine and 3,3-dinitroazetidine are of note as they show protonation of a secondary amine, as well as how nitro-groups on DNAZ result in a lower decomposition temperature than for NTO. AANTO is desirable for its high nitrogen content. AANTO is similar to previous salts (amine is protonated).

The lack of property-structure relationships presents a challenge for the design of new NTO-based materials. The aim of this work is to explore structure-property relationships for a series of salts and co-crystals. The approach is to form salts and co-crystals of NTO with a range of co-formers and then test properties using calorimetric and impact studies.

1.4 Aims

The lack of structure-property relationships presents a challenge for the design of new NTO-based co-crystals and salts. Hence this work was conducted with the following aims:

- Gain crystal structures of a selection of NTO salts and co-crystals with a range of non-energetic co-formers: substituted anilines, N-heterocycles and triazoles.

- Investigate polymorphism of co-crystals and salts. Obtain equations of state of NTO salts to understand compression behaviour
- Analyse non-covalent interactions such as H-bonding, halogen bonding and π -stacking
- Explore physical properties such as thermal stability, morphology, impact sensitivity, calculated detonation parameters.
- Identify aspects and features of co-formers and crystal structures that link to property control.
- Develop an enhanced understanding of how structure influences key properties such as sensitivity and energy output
- Knowledge gained can be applied in the design and crystal engineering of new co-crystals and salts with enhanced properties

1.5 References

1. A. Becuwe and A. Delclos, *Propellants, Explosives, Pyrotechnics*, 2004, **18**, 1-10
2. J. Akhavan, *The Chemistry of Explosives*, 3rd edn., The Royal Society of Chemistry, 2011
3. C. E. Munroe and C. Hall, *A Primer on Explosives for Coal Miners*, U.S. Government Printing Office, 1909
4. L. Medard, *Accidental Explosions, Volume 2: Types of Explosive Substances*, John Wiley and Sons: New York, 1989
5. O. H. Johnson, Naval Ordnance Laboratory *report NAVORD-4371* (October 1956)
6. J. A. Zukas, W. Walters, *Explosive Effects and Applications*, Springer Verlag, New York, 1998
7. R. Vijayalakshmi, S. Radhakrishnan, Pooja Shitole, S. J. Pawar, V. S. Mishra, R. K. Garg, M. B. Talawar and A. K. Sikder, *RSC Adv.*, 2015, **5**, 101647–101655

8. J. Sarkar, *Sputtering Materials for VL SI and Thin Film Devices*, Butterworth-Heinemann, Elsevier, Amsterdam, 2014
9. D. Izsák, T. M. Klapötke and C. Pflüger, *Dalton Trans.*, 2015, **44**, 17054–1706
10. R. M. Doherty and R. L. Simpson, in *International Conference of ICT, 28th*, Karlsruhe, Federal Republic of Germany, 1997, pp. 32(1)-32(23)
11. K. Y. Lee and M. D. Coburn, *LA-10302-MS, Los Alamos National Laboratory*, 1985
12. K. Y. Lee, M. D. Coburn and L. B. Chapman, *Journal of Energetic Materials*, 1987, **5**, 27-33
13. T. N. Hall and J. R. Holden, *Part III. Properties of Explosives and Explosive Compositions*, NSWC MP 88-116, White Oak Laboratory, Naval Surface Warfare Centre, Maryland, USA, 1988
14. J. P. Agrawal, *High Energy Materials - Propellants, Explosives and Pyrotechniques*, Wiley-VCH, Padstow, Cornwall, 2010
15. K. Y. Lee and R. Gilardi, Materials Research Society Symposium, Massachusetts, USA, 1992
16. K. V. Prabhakaran, S. R. Naidu and E. M. Kurian, *Thermochimica Acta*, 1994, **241**, 199-212.
17. E. Enzmann and J. Huber, *Germany Pat.*, DE102011012773-A1, 2011
18. M. W. Smith, M. D. Cliff, *NTO-Based Explosive Formulations*, DSTO Aeronautical and Maritime Research Laboratory, Australia, 1999
19. S. M. Walley, J. E. Field, M. W. Greenaway, *Materials Science and Technology*, 2006, **22** (4), 402-413
20. G. R. Desiraju, *Angewandte Chemie International Edition in English*, 1995, **34**, 2311-2327
21. G. R. Desiraju, *Journal of Chemical Sciences*, 2010, **122**, 667-675.
22. R. Pepinsky, *Phys. Rev.* 1955, **100**, 971
23. D. V. Terekhova, S. I. Soldatov, *Journal of Structural Chemistry*, 2005, **46**, S1.
24. V. R. Thalladi, *Chem. Commun.*, 1996, **0**, 401-402.

25. G. Jeffrey, *An introduction to hydrogen bonding*, Oxford University Press, New York, Oxford, 1997.
26. C. B. Aakeroy, N.R. Champness, and C. Janiak, *CrystEngComm*, 2010, 22-43.
27. E. Arunan, *Pure and Applied Chemistry*, 2011, **83**, 1637-1641.
28. G. Paola, B. Valerio, P. Loretta, a. Valeria Ferretti and G. Gastone, *Journal of the American Chemical Society*, 2004, **126**, 3845-3855.
29. G. Gilli, P. Gilli, *Strength from Weakness: Structural Consequences of Weak Interactions in Molecules, Supramolecules and Crystals*, Dordrecht., 2001.
30. G. Paola, B. Valerio, a. Valeria Ferretti and G. Gastone, *Journal of the American Chemical Society*, 2000, **122**, 10405-10417.
31. P. G. Gilli, B. Valerio, F. Valeria and Gastone, *Journal of the American Chemical Society*, 1994, **116**, 909-915
32. P. Metrangolo and G. Resnati, *Science*, 2008, **321**, 918-919.
33. P. Politzer, J. S. Murray and M. C. Concha, *Journal of Molecular Modeling*, 2007, **13**, 643-650.
34. T. Clark, M. Hennemann, J. S. Murray and P. Politzer, *Journal of Molecular Modeling*, 2011, **18**, 2461–2469
35. C. A. H. Sanders and K. M. Jeremy, *Journal of American Chemical Society*, 1990, **112**, 5525-5534.
36. D. A. Dougherty, *Accounts of Chemical Research*, 2013, **46**, 885-893.
37. H. T. Chifotides and K. R. Dunbar, *Accounts of Chemical Research*, 2013, **46**, 894-906.
38. R. Censai. P. Di Martino, *Molecules*, 2015, **20**, 18759-18776
39. F. Tian, N. Sandler, J. Aaltonen, C. Lang, D. J. Saville, K. C. Gordon, C. J. Strachan, J. Rantanen, T. Rades, *J. Pharm. Sci.*, 2007, **96** (3), 584-94
40. W. C. McCrone, *Polymorphism. In Physics and Chemistry in the Organic Solid State*, Interscience Publishers, New York
41. E. Mitscherlich, *Ann. Chim. Phys.*, 1822, **19**, 350–419
42. D. I. A. Millar, *Energetic Material at Extreme Conditions*, Springer Theses, Springer-Verlag, Berlin Heidelberg, 2012
43. J. V. Viswanath, K. J. Venugopal, N. V. Srinivasa Rao, A. Venkataraman, *Defence Technology*, 2016, **12**, 401-418

44. A. J. Cruz-Cabeza, *Crystengcomm*, 2012, **14**, 6362-6365
45. D. J. Good, N. Rodríguez-Hornedo, *Cryst. Growth Des.*, 2009, **9**, 2252–2264.
46. P. Vishweshwar, J. A. McMahon, J. A. Bis and M. J. Zaworotko, *Journal of Pharmaceutical Sciences*, 2006, **95**, 499-516.
47. J. F. Remenar, J. M. MacPhee, K. L. Bridget, A. T. Viraj, H. H. Jason, A. M. David, B. H. Magali, *Organic Process Research & Development*, 2003, **7**, 990-996.
48. S. M. Berge, L. D. Bighley and D. C. Monkhouse, *Journal of Pharmaceutical Sciences*, 1977, **66**, 1-19.
49. J. F. Remenar, S. L. Morissette, M. L. Peterson, B. Moulton, J. M. MacPhee, *Journal of the American Chemical Society*, 2003, **125**, 8456–8457.
50. S. L. Morissette, *Advanced Drug Delivery Reviews*, 2004, **56**, 275–300.
51. K. Seefeldt, J. Miller, F. Alvarez-Núñez and N. Rodríguez-Hornedo, *Journal of Pharmaceutical Sciences*, 2007, **96**, 1147-1158
52. C. R. Groom, I. J. Bruno, M. P. Lightfoot and S. C. Ward, *Acta Cryst.*, 2016, **B72**, 171-179
53. M. C. Etter, *Acc. Chem. Res.*, 1990, **23**, 120–126
54. J. W. Steed, *Trends in Pharmacological Sciences*, 2013, **34**(3): 185-193
55. N. Blagden, D. J. Berry, A. Parkin, H. Javed, A. Ibrahim, P. T. Gavan, L. L. De Matos, and C. C. Seaton, *New J. Chem.*, 2008, **32**, 1659-1672
56. B. S. Sekhon, *Ars Pharm*, 2009, **50**:3, 99-117
57. N. Schultheiss, A. Newman, *Cryst Growth Des.*, 2009, **3**; **9**(6): 2950–2967.
58. J-B. Arlin, L. S. Price, S. L. Price, A. J. Florence, *Chem. Commun.*, 2011, **47**, 7074-7076.
59. P. Vishweshwar, J. A. McMahon, J. A. Bis and M. J. Zaworotko, *Journal of Pharmaceutical Sciences*, 2006, **95**, 499-516
60. M. B. Hickey, M. L. Peterson, L. A. Scoppettuolo, S. L. Morrisette, A. Vetter, H. Guzman, J. F. Remenar, Z. Zhang, M. D. Tawa, S. Haley, M. J. Zaworotko and O. Almarsson, *European Journal of Pharmaceutics and Biopharmaceutics*, 2007, **67**, 112-119
61. N. Blagden, S. J. Coles, D. J. Berry, *CrystEngComm*, 2014, **16**, 5753–5761
62. A. M. Comer, C. M. Perry, D. P. Figgitt, *Paediatr Drugs*, 2001, **3**, 61-79

63. B. C. Sherman, US Pat., 6,077,542, 2000.
64. N. K. Duggirala, M. L. Perry, O. Almarsson, M. J. Zaworotko, *Chem. Commun.*, 2016, **52**, 640-655
65. P. K. Thallapally, S. Basavoju, G. R. Desiraju, M. Bagieu-Beucher, R. Masse, J. F. Nicoud, *Curr. Sci.*, 2003, **85**, 995-1001
66. F. H. Herbstein and M. Kaftory, *Acta Crystallographica Section B: Structural Crystallography and Crystal Chemistry*, 1975, **31**, 60-67.
67. S. D. Purkayastha, and A. N. Talukdar, *Indian journal of pure and applied physics*, 1980, **18**, 702-703.
68. J. C. Barnes and W. Golnazarians, *Acta Crystallographica Section C: Crystal Structure Communications*, 1987, **43**, 549-552.
69. W. T. A. Harrison, M. A. Ashok, H. S. Yathirajan and B. Narayana Achar, *Acta Crystallographica Section E: Structure Reports Online*, 2007, **63**.
70. F. H. Herbstein and M. Kaftory, *Acta Crystallographica Section B: Structural Crystallography and Crystal Chemistry*, 1976, **32**, 387-396.
71. K. B. Landenberger and A. J. Matzger, *Cryst. Growth Des.*, 2010, **10**, 5341-5347
72. Z. Yang, Y. Wang, J. Zhou, H. Li, H. Huang, F. Nie, *Propellants Explos. Pyrotech.*, 2014, **39**, 9 –13
73. S. R. Anderson, P. Dube, M. Krawiec, J. S. Salan, D. J. am Ende, P. Samuels, 2016, DOI: 10.1002/prop.201600065
74. A.T.Nielsen, A. P. Chafin, S. L. Christian, D. W. Moore, M. P. Nadler, R. A. Nissan, D. J. Vanderah, R. D. Gilardi, C. F. George, J. L. Flippen-Anderson, *Tetrahedron*, 1998, **54**, 11793
75. G. Jacob, L. Toupet, L. Ricard, G. Cagnon, *Private Communication*, 1999
76. O. Bolton, L. R. Simke, P. F. Pagoria, A. J. Matzger, *Cryst. Growth Des.* 2012, **12**, 4311
77. O. Bolton, A. J. Matzger, *Angew. Chem., Int.Ed.* 2011, **50**, 8960
78. H. Lloyd, *Proceedings of the 18th Seminar on New Trends in Research of Energetic Materials*, University of Pardubice, Czech Republic, 2015, p.178.

79. S. T. Malinovskii, M. S. Fonar, Y. A. Simonov, A. A. Dvorkin, E. V. Ganin, N. G. Luk'yanenko and G. S. Musienko, *Soviet physics. Crystallography*, 1992, **37**, 352-355
80. K. Y. Lee and M. D. Coburn, *United States Pat.*, 1988.
81. K. Y. Lee and M. M. Stincipher, *Propellants, Explosives, Pyrotechnics*, 1989, **14**, 241-244.
82. D. T. Cromer, J. H. Hall, K. Y. Lee and R. R. Ryan, *Acta Crystallographica Section C: Crystal Structure Communications*, 1988, **44**, 1144-1147.
83. J. P. R. Lee, K. Y. Lee, D. T. Cromer, E. M. Kober and D. D., *The Journal of Organic Chemistry*, 1990, **55**, 1994-2000.
84. J. L. G. De Paz and J. Ciller, *Propellants, Explosives, Pyrotechnics*, 1994, **19**, 32-41.
85. L. Yang, T.-L. Zhang, C.-G. Feng and K.-B. Yu, *Acta Physico-Chimica Sinica*, 2001, **17**, 438-442
86. J. P. Ritchie, E. M. Kober, 9th International Symposium on Detonation, Portland, OR, USA, 1989.
87. H. M. Wen, S. Jirong, H. Rongzu, Z. Gaohong, X. Kangzhen and Zhenyi, *Journal of Molecular Structure*, 2004, **678**, 217-222.
88. Z. Li, H. Ma, B. Yan, Y. Guan and J. Song, *Chinese Journal of Chemistry*, 2009, **27**, 2284-2290.
89. S. Dong, G. Zhang, B. Chen, Y. Ou and H. Jai, *Acta Crystallographica Section C: Crystal Structure Communications*, 1996, **52**, 2057-2058.
90. Y. H. Ren, F. Q. Zhao, J. H. Yi, K. Z. Xu, H. X. Ma, R. Z. Hu and J. R. Song, *J. Iran Chem. Soc.*, 2012, **9**, 407-414

Chapter 2

Experimental Techniques

2.1 Synthesis of Nitrotriazolone

The synthesis of nitrotriazolone (NTO) was carried out in a simple two-step process: (i) the condensation of semicarbazide hydrochloride and formic acid, producing triazolone (TO), and (ii) the nitration of TO to form nitrotriazolone. This synthetic strategy has been described in many published works [1-4] and is only slightly altered from that reported in the late 1960's [5]. Solid semicarbazide hydrochloride (38.78 g, 0.3 mol) was added to 85 % formic acid (40 ml, 0.8 mol) and heated to 60 °C with stirring. Water was added to the mixture (90 ml) to remove excess formic acid *via* distillation. The contents of the reaction were filtered and recrystallized. 15 g of TO was added to 90 ml of nitric acid (70 %) and heated to a maintained temperature of 60-70 °C with constant stirring, for approximately 2 hours. Once the reaction is complete contents are immediately placed in an ice-bath (0-5 °C). Precipitate was then filtered and washed with water to remove excess nitric acid.

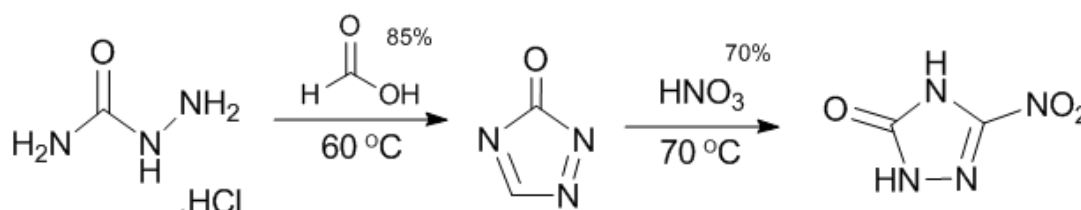


Fig 2.1 Reaction scheme of the synthesis of NTO

2.2 Preparation Routes to Co-crystals

The most common method for the preparation of co-crystals is evaporative crystallisation, in which the two components are dissolved in a suitable solvent that is then allowed to evaporate slowly. An alternative method is to exploit the different solubilities of the co-crystal and its components, and add one of the components to a saturated solution of the other component. In favourable cases this results in preferential precipitation of the co-crystal. This approach has been described and analysed in detail by Rodriguez-Hornedo *et al.* [6]. Other methods include: slurring of the two components; grinding of the two

solid components using a pestle and mortar, sometimes in the presence of a small amount of solvent (liquid-assisted grinding); and ball-milling. Clearly the application of grinding and milling techniques for energetic materials should be used with caution. A relatively new technique that is attracting attention is resonant acoustic mixing, which uses high-amplitude, low-frequency agitation to intimately mix solid or viscous components. Co-crystal formation using this technique has recently been demonstrated for pharmaceuticals [7] and energetic materials [8].

For most of the work described in this thesis the method of evaporative crystallisation from a super-saturated solution has been used. Detailed procedures with quantities and materials are described in the relevant chapters. The basic procedure of evaporative crystallisation involved weighing 1:1 molar ratios of energetic material and co-former into separate vials and adding minimal volumes of either cold or hot solvent. Solutions from each vial were then mixed and heated at 50°C for a particular length of time. On cooling crystallisation of polycrystalline powders usually occurred. For growth of single crystals, the solution was left to evaporate slowly at room temperature. In some cases solutions are placed in 5-10°C environments to slow further the evaporation process, with an aim of producing larger single crystals.

Deuterated samples were obtained by first obtaining protonated energetic material and co-former, ~ 0.5 g each, and then recrystallising both materials in a deuterated solvent. In the work presented here, the solvent was D₂O unless otherwise stated. Having deuterated the starting components, the above evaporative crystallisation procedure is followed using deuterium oxide as solvent.

2.3 Single Crystal and Powder X-ray Diffraction

Single crystal X-ray diffraction is the most definitive method for the determination of atomic positions within crystalline solids. When an X-ray beam passes through a crystal, the radiation interacts with the electron cloud within the atoms, creating X-ray scattering more commonly referred to as Thompson scattering [9]. X-ray crystallography encompasses the knowledge that the resulting scattering will have significant intensity in certain directions. For single crystal X-ray diffraction, Bragg's law is used to express this. It provides the conditions for a plane wave to be diffracted from a family of lattice planes – denoted by Miller index (h,k,l) – with constant lattice

spacing, d . If the diffraction angle, 2θ , and wavelength of the X-ray beam, λ , are measured, d can be calculated, resulting in the relative positions of the atoms within the structure. To satisfy the equation, the wavelength of the X-ray radiation is comparable with interatomic separations.

$$2d\sin\theta = n\lambda \quad (\text{Eq. 2.1})$$

The angle of incidence, θ , is equivalent to the angle of diffraction, as shown in Fig 2.1. Whilst the path length of individual X-rays that scatter from different planes differ, the scattered waves will be constructive in phase conceding that the path difference in an integral number of wavelengths, $n\lambda$.

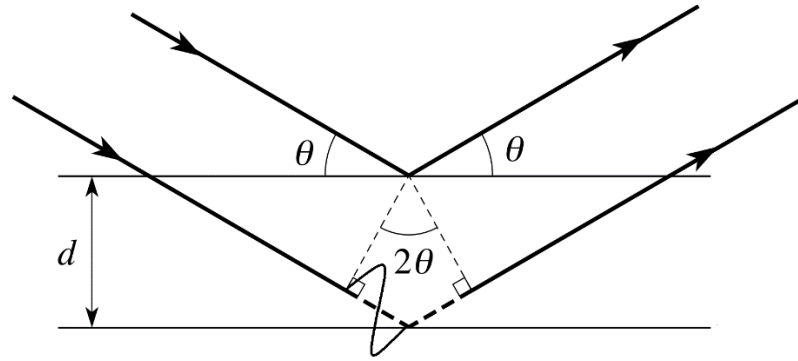


Fig 2.2 Bragg's law reflection. X-rays incident on the crystal lattice at an angle θ , producing diffracted X-rays.

A large selection of information can be directly extracted from an observed diffraction pattern, i.e. the unit cell indexing and space group. In addition, the observed intensities provide information regarding the amplitude of the scattering waves, $|F_0|$. However, information about the phase is (φ) lost, which is known as the "phase problem". Without both the amplitude and phase of the scattered X-rays, an accurate representation of the electron density within the unit cell cannot be achieved.

$$\rho_{(xyz)} = \frac{1}{V} \sum_{hkl} |F(hkl)| \exp[i\varphi(hkl)] \exp[-2\pi i(hx + ky + lz)] \quad (\text{Eq. 2.2})$$

There are two main methods for overcoming the phase problem, and therefore structure determination: (i) Patterson methods, and (ii) direct methods. Patterson methods often rely on the presence of heavy atoms and use $|F_0|^2$ rather than $|F_0|$ to overcome the phase problem. The resultant Patterson map which resembles the appearance of an electron density map, actually maps the interatomic vectors within the structure. Each peak corresponds to a vector between two atoms and its size is proportional to the squares of the atomic numbers of the atoms related by this vector.

$$P(uvw) = \frac{1}{V} \sum_{hkl} |F(hkl)|^2 \cos[2\pi(hu + kv + lw)] \quad (\text{Eq. 2.3})$$

In direct methods, the initial strategy is to mathematically derive the phases of the structure factors, and therefore the electron density, from a set of observed X-ray intensities. The method exploits constraints within statistical relationships (such as discrete peaks and non-negative values) between sets of structure factors, hence producing potential values for the phases. Direct methods are usually applied to lighter atom structures, so is ideal for organic molecules. This study is concerned with purely organic compounds and so direct methods have been used for structure determination.

In both Patterson and direct methods, residual electron density ($\Delta\rho$) is calculated to refine the structure. Residual density is defined as the difference between the calculated structure factors and the observed structure factors. Using such Fourier syntheses it is possible to determine whether a complete and accurate model has been achieved. Furthermore, hydrogen positions are able to be determined in high-quality data-sets.

In this work, crystal structures were solved and refined using direct methods using the program CRYSTALS [10]. The details for each structure solution are described in the relevant sections.

2.4 Powder X-ray diffraction

Instead of focusing on one crystal, powder X-ray diffraction exploits the fact that powder samples contain a set of crystals in random orientations. This results in

concentric cones of diffracted intensity from the sample. That are displayed as a series of rings on an area detector. The area detector is placed normal to the X-ray beam.

In single crystal X-ray diffraction, Patterson and direct methods are used to determine the crystal structure, which rely heavily on the accuracy of the determination of reflection intensities. This reliance becomes difficult in X-ray powder diffraction where peak overlap is common. Numerous programs such as DASH [11] and FOX [12] have been developed to overcome limitations of reciprocal-space methods. Such programs generate calculated patterns from indexed patterns, provided the chemical composition of the unit cell is known. A Monte Carlo approach is employed to optimise the agreement between observed and calculated patterns, known as "simulated annealing". The end result is a fitted structure (with the lowest goodness-of-fit, χ^2) that should correspond with the experimental structure.

A powder diffraction pattern is described in a plot as diffraction intensity (I_{obs}) against scattering angle (2θ). Least-squares refinement of the structural parameters is performed using the Rietveld method. This method minimises the difference between the calculated and observed intensities (I_{obs} vs I_{calc}). The quality of the fit is quantified by the weighted R-factor (wR_p) and χ^2 , which is the comparison of wR_p to the statistically expected value R_{exp} . In this work Rietveld refinements of various powder patterns were performed using GSAS [13] and TOPAS [14].

Irrespective of the collection procedure, X-ray powder diffraction presents a quick, yet often definitive representation of the scattering arising from the atomic planes within the sample of interest. It is an invaluable tool for assessing purity and for detection of polymorphism, which overcomes the difficulty of obtaining single crystals.

2.5 X-ray Sources: Laboratory versus Synchrotron

The ambient-temperature and ambient-pressure X-ray powder diffraction experiments detailed in this work were performed using a D2 PHASER. It provides a means of rapidly obtaining powder diffraction patterns, used for initial screening of samples. The powder patterns obtained from this device are of insufficient resolution to solve crystal structures, but they can be used in comparison of powder patterns to determine

the purity of new materials. All single crystal X-ray diffraction experiments were conducted using monochromatic laboratory X-ray sources in the School of Chemistry, University of Edinburgh. Both Mo-K α and Cu-K α_1 radiation sources were utilised ($\lambda = 0.71073$ and 1.54056 Å, respectively). Details of the data collection procedures are described in the relevant chapters.

In some cases, however, the restrictions applied to collecting and analysing powder diffraction data through laboratory sources, means that it is necessary to use X-ray radiation of shorter wavelengths (i.e. $\lambda \leq 0.5$ Å) at synchrotron sources. Using such radiation improves data completeness by compressing the characteristic diffraction pattern into a small volume of reciprocal space. In turn the smaller volume allows a larger portion to be accessed through an opening angle of 40° . In addition, synchrotron radiation has an increase of incident flux that counteracts the weak diffraction seen in organic samples and complex sample environments, such as diamond anvil cells.

In the current work synchrotron radiation has been essential in attaining high-resolution powder diffraction data for determining the complete crystal structure of polycrystalline samples and the observation of temperature dependent polymorphism. In addition, the acquisition of high-resolution powder diffraction data using the diamond-anvil cell is only possible through the use of synchrotron radiation.

2.6 Powder Neutron Diffraction

Neutron diffraction is a complementary technique to X-ray diffraction and uses the same principles. Neutrons can be diffracted by a three-dimensional grating, due the property of wave-particle duality. The momentum of a free particle, p , is related to its wavelength, λ , by the de Broglie equation,

$$\lambda = \frac{h}{p} = \frac{h}{mv} \quad (\text{Eq. 2.4})$$

where h is Planck's constant, m = mass and v = velocity of the particle. Whilst X-rays interact with the electron density of atoms, neutrons are diffracted by the nuclei. Both

neutrons and nuclei are small, so significant diffraction only occurs when the neutron passes close to the nucleus. On account of the much lower fluxes obtained from neutron sources compared to X-ray source, the intensity of diffraction of neutrons by a crystal is much lower than that of X-rays, hence larger sample volumes are required to give comparable statistics. Furthermore, neutron diffraction locates the atomic nuclei of the sample rather than the electron density, which can be distorted by bonding effects, giving a more accurate atomic position. The scattering power of an atom does not have a direct relationship in neutron diffraction, whilst X-ray radiation is directly proportional to its atomic number (Z). Therefore elements with similar atomic numbers and isotopes can be more easily distinguished. An additional benefit of the lack of correlation is the potential to determine the positions of hydrogen atoms more accurately. Hydrogen atoms diffract X-rays extremely weakly and therefore it is difficult to accurately determine their positions, due to having just one electron, but the scattering cross section of hydrogen makes it distinguishable in neutron diffraction. One drawback of scattering from hydrogen is the production of a very high, incoherent background. For this reason, neutron powder diffraction normally requires the use of deuterated samples.

2.7 High-pressure X-ray Diffraction – Diamond Anvil Cell

High-pressure X-ray powder diffraction studies were performed using a gasketed diamond-anvil cell (DAC). The concept of this device is relatively simple; the sample is placed between two diamond faces (culets) and is subjected to high-pressure when a force pushes the opposing anvils together. The DAC employed in this work is based on a Merrill-Bassett cell, first developed in 1974 [15]. The utility and small size (~5 cm diameter) make these cells extremely versatile and a perfect device for high-pressure X-ray diffraction studies. A photograph of the Merrill-Bassett diamond-anvil cell is shown in Fig 2.3, along with a representation of the principles of such a device.

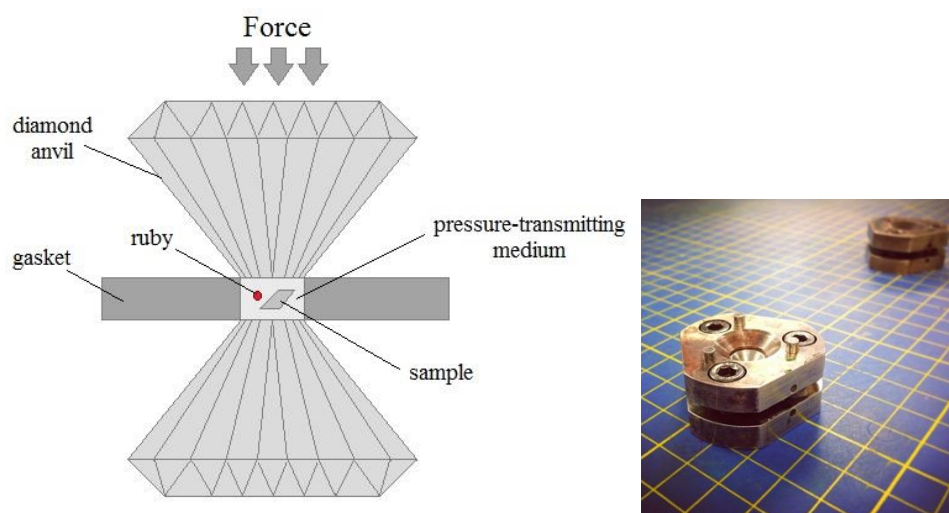


Fig 2.3 Expanded schematic of the anvil and gasket within a diamond anvil cell, and a photograph of a diamond anvil cell.

In a Merrill-Bassett DAC the diamond anvils are mounted onto two backing plates, which are encased in a steel body (Fig 2.4). Three screws in the steel body hold the anvil together. Once the screws are tightened a force is applied to the outer faces of the diamonds, which is then multiplied numerous times at the small cutlets. The cutlet size is the limiting factor in determining the maximum pressure that can be exerted. A cutlet size of 600 μm was used in the current study, thereby allowing maximum pressures of ca 10 GPa to be attained.

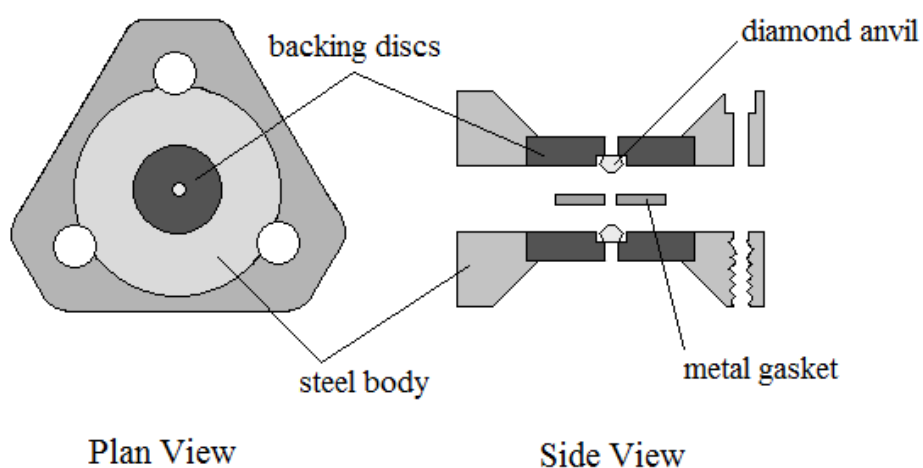


Fig 2.4 Expanded schematic of a diamond anvil cell

In the original design of a DAC, beryllium was used as the backing plates on which to mount the diamond anvils, due to its tensile strength and transparency to X-rays. However a major disadvantage of beryllium backing plates, is the tendency to contaminate the diffraction image with polycrystalline metal powder rings. This problem is accentuated when high flux and low divergence synchrotron X-ray beams are used. To remove these issues with Be-backing plates, tungsten carbide or steel backing seats have been introduced. However, due to the opacity of these materials to X-rays, large portions of the diffracted beam are absorbed reducing the reciprocal space accessible in a high-pressure experiment. The alteration of backing plate design to possess wider opening angles in which a conical Böhler-Almax diamond anvil can be embedded has been utilised to overcome this.

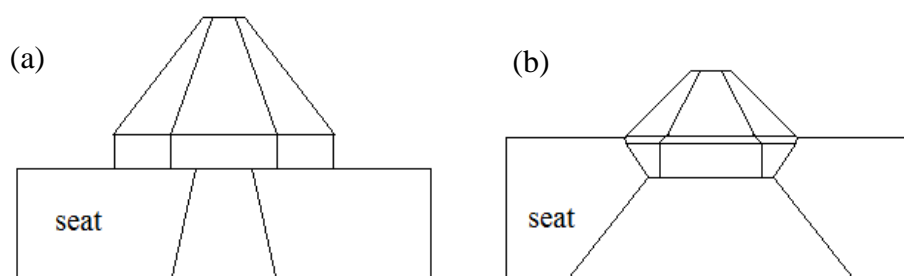


Fig 2.5 Initial diamond and backing plate (a) and a conical Böhler-Almax diamond anvil (b)

The metal gasket is sandwiched between the cutlets of the diamond. Upon compression the gaskets extrudes around the anvils, forming a seal around the sample chamber. In an ideal gasket the sample chamber will reduce in thickness, allowing the volume of the sample to decrease and hence the pressure to increase. If the gasket is too thick however, the gasket and hole will expand which can ultimately cause damage to the diamonds. Therefore gaskets are usually pre-indented to ensure a thin gasket which allows for higher pressures. In the work presented herein, a 250 μm thick tungsten gasket was used, with a pre-indented thickness of 100-150 μm . In order to achieve hydrostatic compression, the sample must be surrounded in a medium, such as a 4:1 mixture of methanol and ethanol, which displays hydrostatic behaviour. Finally a spherical synthetic ruby is placed in the sample chamber in order continuously measure the pressure of the cell. Measurements are obtained by

observing the laser-induced fluorescence of the ruby. The spectral lines of ruby undergo a red-shift with applied pressure; a linear dependence is observed for both parameters. Spectra were collected using the 632.8 nm line from a He-Ne laser and detected by a Jobin-Yvon LabRam 300 spectrometer (precision of ± 0.05 GPa)

Sample loading was conducted carefully to ensure that the polycrystalline sample and the ruby was not flushed out when flooding of the sample chamber with pressure transmitting medium.

2.8 High-pressure Neutron Diffraction – Paris-Edinburgh Cell

In contrast to X-ray diffraction, neutron diffraction requires a much larger sample volume size (ca. 10^6 times larger). Hence the Paris-Edinburgh Cell (PE-Cell) was developed in 1992 with a pressure range of 10-20 GPa [16]. Prior to this, commercial devices of the time which weighed close to 1 tonne, and so the (relatively) light-weight design (~ 50 kg) and portability made the PE-Cell a practical and popular option. In addition the load can be applied to the cell by a hydraulic ram while *in situ* on the beamline.

The anvils in which the sample is compressed are constructed from either of tungsten carbide (WC) or sintered diamond. Within the anvils, a TiZr gasket, utilised for its lack of scattering, is employed to confine the sample. A solid sphere of lead was used as a pressure sensor. Lead has a clearly defined equation of state, which allows the unit cell volume to be directly compared and related to the pressure within the gasket; making it an ideal pressure calibrant. In this work the pressure-transmitting medium was a 4:1 deuterated methanol:ethanol mixture.

The high-pressure neutron diffraction experiments conducted in this work were performed at the ISIS Spallation Neutron And Muon Source, STFC Rutherford Appleton Laboratory, UK. The high-flux, medium-resolution instrument PEARL-HiPr is specifically designed for data collection using a Paris-Edinburgh Cell. Time-of-flight diffraction data were collected in transverse geometry. The detectors are fixed at $83^\circ < 2\theta < 97^\circ$ and allow access to a d-spacing range of 0.5-4.1 Å, with a resolution

($\Delta d/d$) of $\sim 0.8\%$. The individual detector element spectra are electronically summed and normalised to the incident beam monitor and the scattering from a standard vanadium calibration sample. Finally, the diffraction pattern was corrected for the wavelength and scattering-angle dependence of the neutron attenuation by the anvil (WC) and gasket (TiZr) materials. Full-profile Rietveld refinements were carried out using GSAS [13].

2.9 Equation of State

It is possible to obtain a measurement of the variation of the material's volume with pressure. The outcome of this describes the materials behaviour under compression. The variation of volume with pressure at constant temperature is termed the isothermal "equation of state" (EoS). It is an equation regularly used in earth sciences and shock physics. Measured equations of state are usually parameterised in terms of the bulk modulus, $B_0 = -V \partial P / \partial V$, and its pressure derivative: $B' = \partial B / \partial P$, which are evaluated at zero pressure. V_0 , the zero-pressure volume, is generally accepted as the unit cell volume at ambient conditions.

The most commonly used formulations, and the only ones used in this study, are the Murnaghan [17] and Birch-Murnaghan [18] equations. The simplicity of the Murnaghan EoS makes it popular. It can be derived from the assumption that the bulk modulus varies linearly with pressure, such that:

$$P = \frac{B_0}{B'} \left[\left(\frac{V_0}{V} \right)^{B'} - 1 \right] \quad (\text{Eq. 2.5})$$

The Murnaghan EoS has been found to reproduce both PV data and B_0 for compressions up to about 10% (i.e. $V/V_0 = 0.9$).

The Birch-Murnaghan utilises an assumption that the strain energy applied during compression can be expressed as a Taylor series in the finite strain, f . The 3rd

order Birch-Murnaghan EoS is based on the Eulerian strain, $f_E = [V/V_0]^{2/3} - 1$], such that:

$$P = 3B_0 f_E (1 + 2f_E)^{\frac{5}{2}} \left[1 + \frac{3}{2}(B' - 4)f_E + \frac{3}{2} \left(B_0 B'' + (B' - 4)(B' - 3) + \frac{35}{9} \right) f_E^2 \right] \quad (\text{Eq. 2.6})$$

In this work, the parameters for the equations of state have been determined by a least-squares fit of the PV data using the program EoSFit v7 [19]. It is simpler to consider pressure as the dependent variable and the sum of the squares of the differences between the calculated and observed are minimised during the least-squares solution.

2.10 Environmental scanning electron microscopy (ESEM)

In order to obtain clear images of the surfaces of organic materials using conventional SEM, prior specimen preparation is required. Environmental scanning electron microscopy (ESEM) was developed for uncoated or hydrated specimens to remove this problem. A low pressure of gas, of up to 10 Torr surrounds the sample. For the ESEM images collected at the Cavendish Laboratory, Cambridge, samples were imaged in the presence of water vapour. The distance at which the electrons, from the injected electron beam, travel within ESEM is kept as short as possible. For a detailed account of environmental scanning electron microscopy for imaging wet materials, the reader is directed to the following review [20]. Samples are attached to an adhesive specimen and placed into the device. For samples described in this study, images were recorded at varying magnifications.

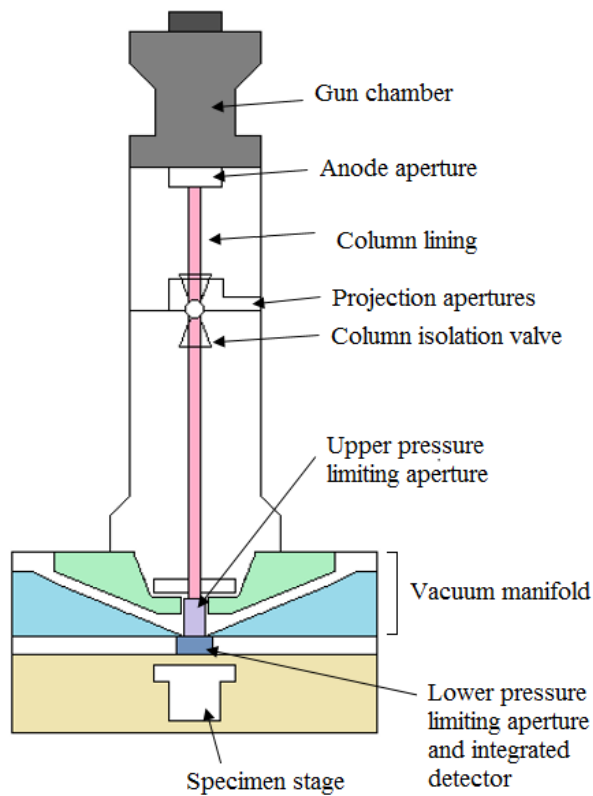


Fig 2.6 Schematic of an ESEM set up [20]

2.11 Sensitivity Testing

The sensitivity of an energetic material to stimuli represents a very important property, since it dictates its ability to be transported, stored and used safely. In addition, it is vital to understand the underlying causes of sensitivity to stimuli, in order to reduce the risks of accidental detonation.



Fig 2.7 Image of BAM Fall Hammer (BFH-12) impact tester

In this work, impact testing was performed using a BAM Fall Hammer (BFH-12) impact tester at the Cavendish Laboratory in Cambridge. To induce the impact a load of 0.5, 1, 2, 5 or 10 kg was dropped onto a sample, contained within an anvil, from a height of 20 - 100 cm. The anvil, denoted as impact device 1, consists of two coaxial steel cylinders. This is the typical device used for standard testing. For experimental testing a sample is placed between a file plate and steel cylinder, known as impact device 2. For standard testing, a sample of 40 mm³ is enclosed in an impact device 1, whilst 10 mm³ tested in impact device 2.



Fig 2.8 Devices used within a BAM hammer (BFH-12) **a** Impact device 1, consisting

of two coaxial steel cylinders within a guide-ring and, **b** impact device 2, involving a file plate and steel cylinder

Initially the “One-in-six” test procedure was performed to obtain limiting impact energy for each tested sample [21]. This is a recommended UN method. A series of tests are conducted to determine the lowest impact energy (stimulus level) that produces an initiation, whilst the next lower level produces no signs of initiation in a series of six trials. This procedure is ideal for small sample sizes and gathering a suitable drop height and load to begin full 30-trial Bruceton testing [22, 23].

The Bruceton method (known as the stair-step method) obtains the stimulus level resulting in a 50% probability of an initiation (impact height, H_{50}). After the first test trial, the sample receives a stimulus depending on the previous outcome. If the sample shows signs of initiation the stimulus is dropped down a level, if no initiation occurs then the next stimulus level moves up a step. Each step size is calculated using a logarithmic scale ($d = 0.05$).

2.12 Differential Scanning Calorimetry (DSC)

Differential scanning calorimetry (DSC) is a technique used to study the thermal behaviour of materials. It is possible to identify and measure thermal transitions, i.e. glass transitions, melting, and solid-solid phase transitions. The temperature of the sample pan, and reference pan, is increased at a rate of 10 K/min. As heat is taken out of the system, such as during an endothermic reaction, the heat flow is increased and as heat is put into the system i.e. an exothermic reaction, the heat flow is decreased. When heat flow is plotted against temperature of the system, it is possible to determine whether an exothermic or endothermic process has occurred. A notable process seen in energetic material is an exothermic decomposition peak. The integration of a peak, such as the decomposition peak, can be calculated to give the exothermic or endothermic heat of the process.

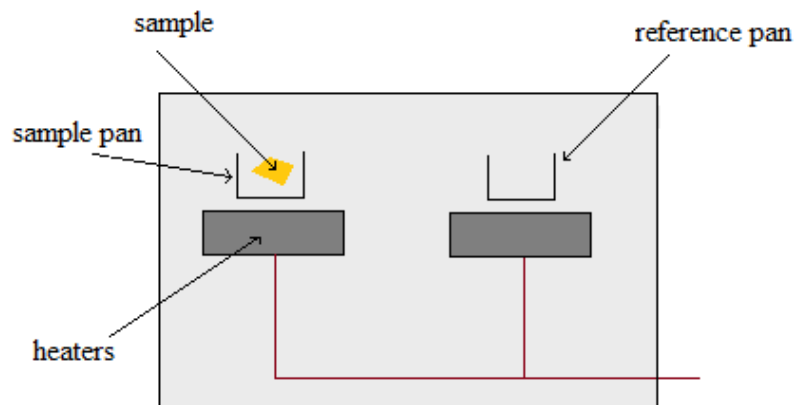


Fig 2.9 Diagram of a DSC set-up [24]

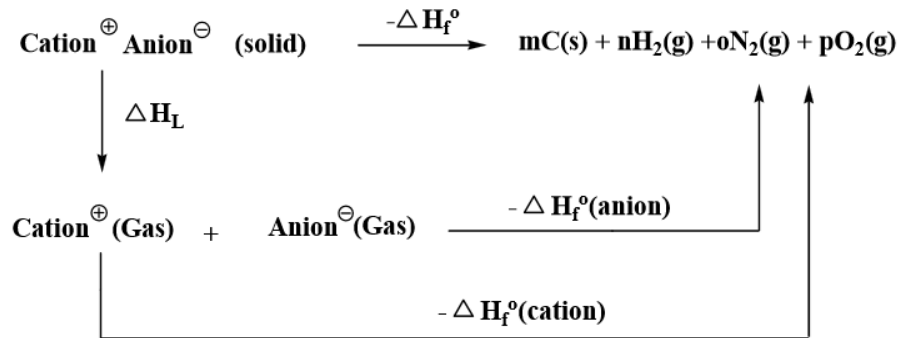
Within this work, DSC was carried out on TA Instruments Q2000 over a temperature range of room temperature (21°C) to 350°C, with an average sample size is 5 mg. Plots were imaged using TA Universal Analysis software [25].

2.13 Calculations of Detonation parameters

Detonation parameters are essential for gaining a basic understanding of a material's energetic performance. There are various methods for gaining such information, as detailed in Chapter 1. All detonation parameters, such as detonation velocity and pressure, presented in this work were gathered from calculations using the program EXPLO5 V6.03. The program is based on the chemical equilibrium, steady-state model of detonation. [26]

EXPLO5 uses the Becker-Kistiakowsky-Wilson's equation of state (BKW EOS) for gaseous detonation products and Cowan-Fickett's equation of state for solid carbon. The detonation parameters were calculated at the C-J point, which is found from the Hugoniot curve of the system by its first derivative. The main detonation products for the calculations of the energetic parameters were assumed to be N₂, H₂O, and CO₂. In addition, compounds with a positive oxygen balance provide O₂ as combustion product.

The detonation parameters in this work were calculated using the experimentally determined crystal density (X-ray), chemical composition, and enthalpy of formation of each material.



Scheme 2.1 Born-Haber energy cycle [20]

$$\Delta H_f^\circ(\text{ionic salt } 298\text{K}) = \Delta H_f^\circ(\text{cation } 298\text{K}) + \Delta H_f^\circ(\text{anion } 298\text{K}) - \Delta H_L \quad (\text{Eq. 2.7})$$

$$\Delta H_L = U_{\text{POT}} + [p(n_m/2-2) + q(n_x/2-2)] RT \quad (\text{Eq. 2.8})$$

$$U_{\text{POT}} = \gamma(p_m/M_m)^{1/3} + \delta \quad (\text{Eq. 2.9})$$

Based on a Born-Haber energy cycle (Scheme 5.1), the heat of formation of a salt can be obtained by the formula shown in equation 2.7, where ΔH_L is the lattice energy of the salt. This can be estimated by the formula suggested by Jenkins *et al.* [27] and used by Shreeve *et al.* [28] shown in equation 2.8, where n_m and n_x depend on the nature of the ions M_p^+ and X_q^- , respectively, and are equal to 3 for monoatomic ions, 5 for linear polyatomic ions and 6 for non-linear polyatomic ions. The equation for the lattice potential energy U_{POT} (eq 2.9) has the form: where density (p_m) g/cm^3 , M_m is the chemical formula mass of the ionic material, g, and the coefficients γ kJ/mol cm and δ kJ/mol are assigned literature values.

2.14 References

1. M. W. Smith, M. D. Cliff, *NTO-Based Explosive Formulations*, DSTO Aeronautical and Maritime Research Laboratory, Australia, 1999
2. T. Mukundan, G. N. Purandare, J. K. Nair, S. M. Pansare, R. K. Sinha, H. Singh, *Defence Science Journal*, 2002, **52** (2), 127-133
3. K. Y. Lee and M. D. Coburn, *LA-10302-MS*, Los Alamos National Laboratory, 1985
4. A. Becuwe and A. Delclos, *Propellants, Explosives, Pyrotechnics*, 2004, **18**, 1-10
5. G. I. Chipen, R. P. Bokalder, V. Y. Grinshtein, *Chemistry of Heterocyclic Compounds*, 1966, **2** (1), 110-116
6. S. L. Childs, N. RodríguezRodríguez-Hornedo, L. Sreenivas Reddy, A. Jayasankar, C. Maheshwari, L. McCausland, R. Shipplett and B. C. Stahly, *CrystEngComm*, 2008, **10**, 856-864
7. D. J. am Ende, S. R. Anderson, J. S. Salan, *Org. Process Res. Dev.*, 2014, **18** (2), 331–341
8. S. R. Anderson, D. J. am Ende, J. S. Salan, P. Samuels, *Propellants Explos. Pyrotech.*, 2014, **39**, 637–640
9. D. W. Bennett, *Understanding Single-Crystal X-Ray Crystallography*, Wiley-VCH, 2010
10. P. W. Betteridge, J. R. Carruthers, R. I. Cooper, K. Prout and D. J. Watkin, *J. Appl. Cryst.*, 2003, **36**, 1487
11. W. I. F. David, K. Shankland, J. van de Streek, E. Pidcock, W. D. S. Motherwell and J. C. Cole, *J. Appl. Cryst.*, 2006, **39**, 910-915
12. V. Favre-Nicolin, R. Cerny *J. Appl. Cryst.*, 2002, **35**, 734-743
13. A.C. Larson and R.B. Von Dreele, "General Structure Analysis System (GSAS)", Los Alamos National Laboratory Report LAUR 86-748 (1994)
14. A. Coelho, TOPAS-Academic V4, Coelho Software, Brisbane, Australia. 2007
15. L. Merrill, W. A. Bassett, *Rev. Sci. Instrum.*, 1974, **45**, 290

16. J. M. Besson, R. J. Nelmes, G. Hamel, J. S. Loveday, G. Weill, S. Hull, *Physica B: Physics of Condensed Matter*, 1992, 180, 907-910
17. F. D. Murnaghan, *Am J Math*, 1937, **59**, 235
18. F. Birch, *Phys Rev*, **71**, 809
19. R. J. Angel, J. Gonzalez-Platas, M. Alvaro, *Zeitschrift für Kristallographie*, 2014, 229, 405-419
20. A. Donald, *Nature Materials*, 2003, **2**, 511 - 516
21. K. L. Kosanke, B. J. Kosanke, B. T. Sturman, R. M. Winokur, *Encyclopedic Dictionary of Pyrotechnics*, Journal of Pyrotechnics, 2012
22. G. R. Walker, The Canadian Armament Research and Development Establishment, TTCP Panel O-2 (Explosives) Working Group on Sensitiveness, 1966
23. L. Shainheit, Technical Report 3413, Picatinny Arsenal, Dover, New Jersey, 1966
24. TA Universal Analysis software, TA Instruments—Waters LLC, New Castle, Delaware, USA, 2003
25. C. S. Smith, *Materials Measurement Methods*, Springer, 2006, 411–413
26. M. Sućeska, *EXPLO5*, v. 6.03, (2015), Brodarski Institute, Zagreb, Croatia
27. H. D. B. Jenkins, D. Tudeal, L. Glasser, *Inorg. Chem.*, 2002, **41**, 2364–2367
28. G-H. Tao, Y. Guo, Y-H. Joo, B. Twamley, J. M. Shreeve, *J. Mater. Chem.*, 2008, **18**, 5524-5530

Chapter 3

Structural Studies of Salts Formed Between Nitrotriazolone and Substituted Aniline and N-Heterocyclic Compounds

3.1 Introduction

Prior to the formation of NTO salts detailed within this thesis, a systematic and informed investigation into potential co-formers was begun. The Cambridge structural database and literature were used to establish pre-existing trends in synthon pairing, in similar molecular salts and co-crystals. Caffeine, picric acid, 3,5-dinitrosalicylic acid and 5-nitropyridin-2-one, have similar synthons to NTO (Highlighted in Figure 3.1) and have formed co-crystals with co-formers such as succinic acid, cytosine and trimesic acid [1-4]. The solubility and pK_a value of each co-former were also considered. Therefore, NTO was initially co-crystallised with such materials and a list of all co-formers which were attempted are detailed in the appendices.

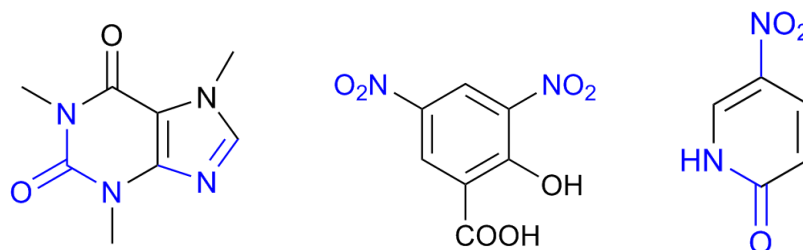


Fig 3.1 Caffeine, 3,5-dinitrosalicylic acid and 3, 5-nitropyridin-2-one

An investigation into 15 salts formed between NTO and substituted anilines has been reported by Singh, who characterised them using gravimetric estimation, TLC and conductivity measurements [5]. No crystal structures were reported, however suggestions were made as to whether solvent was present and to where the proton had been transferred. To test explosive properties, Singh performed dynamic and isothermal TG, DTA and explosion delay experiments [6]. Although the results are ambiguous, some details are of note, such as the proposed decomposition pathway of

arylamine NTO salts. It is suggested that the first step is proton transfer, followed by separation of the component, then decomposition of NTO as normal. These salts are of interest as all the co-formers are structurally similar; so through variation of the functional group, interaction-property relationships can be derived if crystal structures of the salts can be obtained. For this reason, and the desire to clear up discrepancies in the paper, a selection of these salts were prepared and characterised using single crystal X-ray diffraction. The results are described later within this chapter.

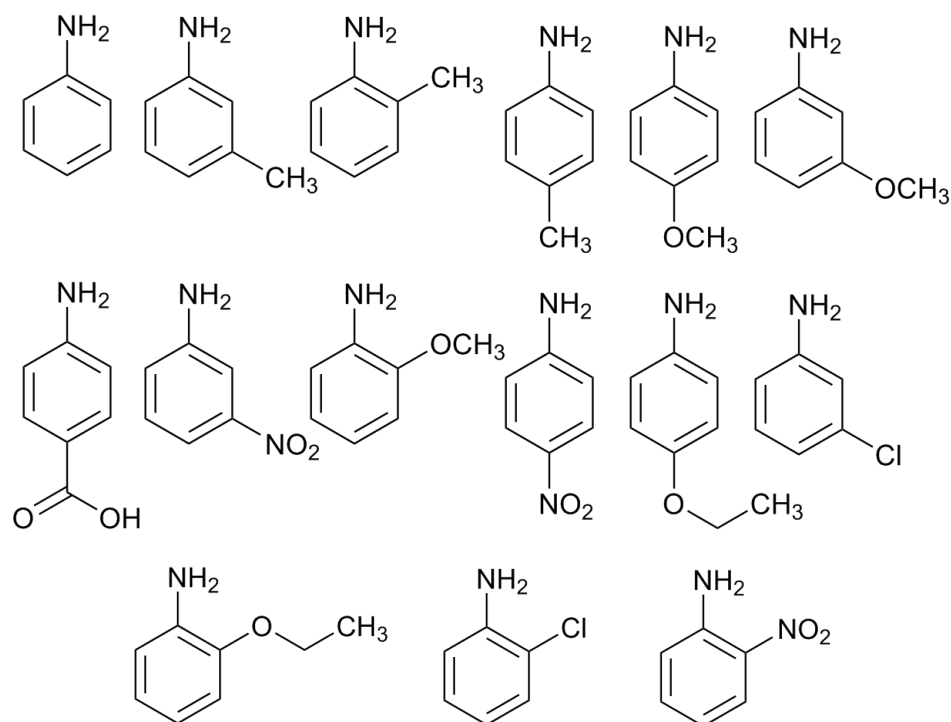


Fig 3.2 Fifteen arylamine co-formers used in study by Singh [5]

A salt containing melamine and NTO (MNTO) was recently reported [7]. Thermolysis data, ^1H NMR, ^{13}C NMR and IR spectroscopy were the methods used to characterise MNTO, but no crystal structure was reported. It was proposed that the structure of the salt contained a protonated amine group rather than a protonated tertiary amine (shown in Fig 3.3). Furthermore, there was no suggestion for the presence of any other molecules within the structure, such as solvent, yet thermal decomposition of the salt indicated a “dehydration” step. A potential advantage of MNTO is its high critical temperature of thermal explosion, which is higher than that of NTO. [7]

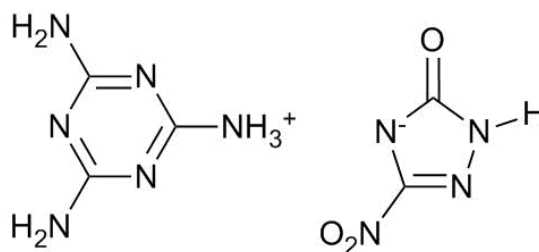


Fig 3.3 Proposed structural formula of MNTO. [7]

3.2 Aims

The motivation of this section was to explore structure-property relationships for a series of pyridine-derived salts. The initial approach was to identify suitable N-based heterocycles such as substituted pyridines.

Such molecules are of interest on account of their increased nitrogen content and the ability to tune interactions through changing substituents. This approach also allows pK_a differences to be modified in order to determine the ΔpK_a threshold for salt/co-crystal formation, with the goal of creating a catalogue for comparisons and form trends between crystal structure properties and physical properties.

In summary the aims of this work were:

- To synthesise aniline based NTO salts
- Compare and contrast the crystal structures to work by Singh
- Identify any relationships or trends

Upon completing these aims, further investigation into 6-membered heterocyclic NTO salts, such as melamine.NTO, was conducted. Resulting in the final set of aims:

- To form novel 6-membered heterocyclic salts – predicted by pK_a difference
- To compare each crystal structure and locate any trends
- To perform basic property testing on a selection of salts

3.3 Experimental

3.3.1 Materials

Aniline, *p*-toluidine, *p*-anisidine, 2-amino-3-picoline, pyridine, melamine, 3-bromopyridine, 3-chloropyridine and piperazine were all obtained from Sigma Aldrich.

Single crystals of all NTO salts were synthesised by slow spontaneous crystallisation from solution at room temperature (1:1 molar ratios, ~10 mg of NTO and co-former in few mls of solvent). Single crystals and powder of aniline.NTO, *p*-toluidine.NTO, *p*-anisidine.NTO, piperazine.NTO, 2-amino-3-picoline.NTO and melamine.NTO were obtained from water. Crystals of pyridine.NTO salt were obtained from NTO dissolved in excess pyridine, whilst 3-bromopyridine.NTO and 3-chloropyridine.NTO were crystallised from methanol.

3.3.2 Powder X-ray Diffraction

X-ray powder diffraction, performed using the D2 PHASER instrument, was utilised in initial screening of samples. Powder patterns were not of sufficient resolution to acquire full crystal structure data but they were used to compare powder patterns of sample with the starting materials. A polycrystalline sample of potential salts (~ 5 mg) was applied thinly to a disc and diffraction patterns recorded over the range of $2\theta = 5 - 50^\circ$.

2-Amino-3-picoline.NTO complex powder X-ray diffraction data was collected, using synchrotron x-ray radiation, on beamline I11 at the Diamond Light Source ($\lambda = 0.827145$), and the structure was solved using TOPAS [8].

3.3.3 Single Crystal X-Ray Diffraction

All single crystal X-ray data for the NTO complexes were collected at 120 K (unless otherwise stated), in the School of Chemistry, using an Agilent Technologies SuperNova diffractometer equipped with an Oxford Cryosystems N₂ low temperature Cryostream. Data for aniline.NTO (An.NTO), anisidine.NTO (Ani.NTO) and 3-chloropyridine.NTO (ClPy.NTO) was collected using monochromated Cu-K α radiation ($\lambda = 1.5418 \text{ \AA}$) whilst data *p*-toluidine.NTO (Tol.NTO), melamine.NTO (Mel.NTO), pyridine.NTO (Py.NTO), 3-bromopyridine.NTO (BrPy.NTO) and piperazine.NTO (Pip.NTO) were collected using monochromated Mo-K α radiation ($\lambda = 0.71073 \text{ \AA}$). Reflections were processed using CrysAlisPro [9] and an absorption correction applied based on the multi-scan method [10]. Within the CRYSTALS [11] program suite, the structures were solved by direct methods using SHELXS [12] and

refined with anisotropic displacement parameters for all non-H atoms using SHELXS. Hydrogen atoms were located using Fourier difference methods and refined isotropically.

3.3.4 Environmental Scanning Electron Microscopy

In order to obtain clear images of the surfaces of organic materials using conventional scanning electron microscopy (SEM), prior specimen preparation, such as gold coating, is required. Environmental scanning electron microscopy (ESEM) was developed for uncoated or hydrated specimens to remove this problem. ESEM images were obtained by Dr. Jon J. Rickard from the University of Cambridge using the ESEM service at the Cavendish Laboratory. Small amounts of material were placed on a flat plate (shown in Fig. 5.2), which was installed in a water vapour environment. Images were obtained at varying magnifications.

3.3.5 Differential Scanning Calorimetry

DSC measurements were performed on a TA Instruments Q2000 over the temperature range 21 - 350°C at a scan rate of 10 K min⁻¹. The sample masses on average were approximately 1-2 mg.

3.3.6 BAM Fall Hammer

BAM Fall Hammer impact testing (BFH-12) was conducted, at the Cavendish Laboratory, Cambridge, on AP.NTO, MeI.NTO, Py.NTO, Pip.NTO, ClPy.NTO and BrPy.NTO and NTO. A sample of 40 mm³ was enclosed in an anvil device consisting of two coaxial steel cylinders. Anvil devices were disposed of along with sample after each test. A variety of loads were dropped from varying heights on all samples. The method conducted throughout is the 30-trial Bruceton method [13]. Anvil device one was initially used on all samples. Later the file plate, or device two, set up was employed for NTO and 2-amino-3-picoline. A positive result is commonly acknowledged by the presence of a flash of light or loud sound (bang), but in these studies it is also distinguished by a discolouration or scorch marks on the device following the test.

3.3.7 Detonation Parameter Calculations

All calculations on the detonation parameters of the materials were performed using the program package EXPLO5 V6.03 [14]. The detonation parameters were calculated at the C-J point with the aid of the steady-state detonation model using a modified Becker-Kistiakowski-Wilson equation of the state for modelling the system. The C-J point is found from the Hugoniot curve of the system by its first derivative. The main detonation products for the calculations of the energetic parameters were assumed with N_2 , H_2O , and CO_2 . The parameters inputted into the software for each salt and co-crystal are; the enthalpy of formation, chemical compositions, and experimentally determined crystal densities.

3.3 Results and Discussion

3.3.1 Salts formed between NTO and Arylamine

Three salts were previously produced and characterised by "conductivity measurements" and DSC [6]. Aniline, *p*-toluidine and *p*-anisidine were crystallised with NTO separately, according to route described by Singh [5] and characterised using single crystal X-ray diffraction.

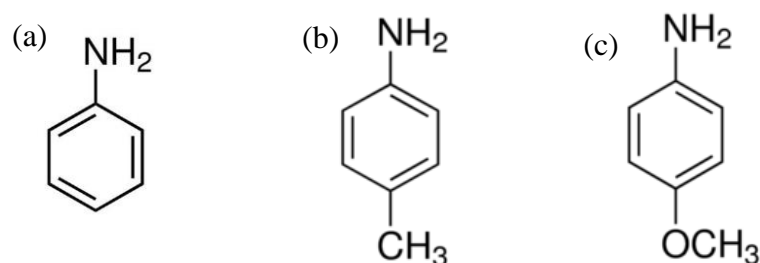


Fig 3.4 Molecular structures of (a) aniline, (b) *p*-toluidine and *p*-anisidine (c)

Although the co-formers have similar molecular structures the resulting salts with NTO are very different in terms of crystal structure parameters, space group and crystal system. To further compare and contrast the three systems the asymmetric unit, intermolecular interactions and crystal structure packing are described together with physical property testing.

Table 3.1 Crystallographic information for An.NTO, Tol.NTO and Ani.NTO

	An.NTO	Tol.NTO	Ani.NTO
Formula	C ₈ H ₁₁ N ₅ O ₄	C ₉ H ₁₁ N ₅ O ₃	C ₉ H ₁₁ N ₅ O ₄
Mr [g.mol⁻¹]	241.20	237.21	253.21
Crystal System	Monoclinic	Orthorhombic	Orthorhombic
Space Group	<i>P2</i> ₁	<i>Pca</i> 2 ₁	<i>Pbca</i>
<i>a</i> (Å)	5.07368(7)	10.1104(5)	10.4966 (5)
<i>b</i> (Å)	8.22943(14)	14.9380(7)	6.6750 (3)
<i>c</i> (Å)	12.49280(19)	7.1785(3)	31.6050 (17)
<i>α</i> (°)	90	90	90
<i>β</i> (°)	90.3054	90	90
<i>γ</i> (°)	90	90	90
<i>V</i> (Å³)	521.61	1084.16	2214.41
<i>ρ</i> (g.cm⁻³)	1.536	1.453	1.519
R-Factor (%)	2.34	4.1	5.08
Radiation	Cu	Mo	Mo
Z	2	4	8

3.3.1.1 Asymmetric Units

The crystal structures, of all 3 salts all show that a proton has been transferred from the NTO molecule to protonate the primary amine upon the co-former. An interesting feature within the asymmetric unit of An.NTO is the water molecule present. This addition of the solvent is not seen in toluidine.NTO and *p*-anisidine.NTO and could alter the decomposition pathway due to the additional step of “dehydration”. The previous report from Singh did not observe its presence, yet it plays an important role in the crystal structure. However, it could be a new hydrate form of An.NTO, and not the same salt reported by Singh [5]. In addition, an attempt to produce an anhydrous form of An.NTO was conducted using methanol and ethanol as solvents. However, no salt or co-crystal product was formed.

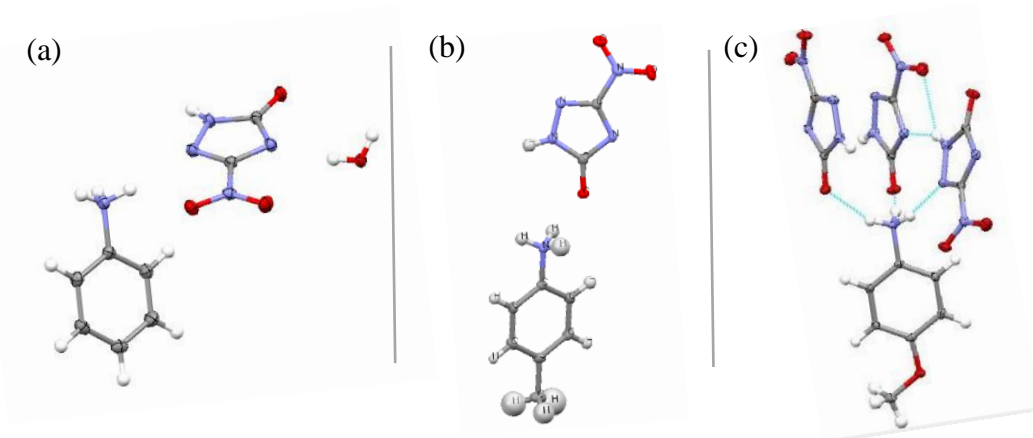


Fig 3.5 Asymmetric units of (a) aniline.NTO, (b) toluidine.NTO, (c) *p*-anisidine.NTO

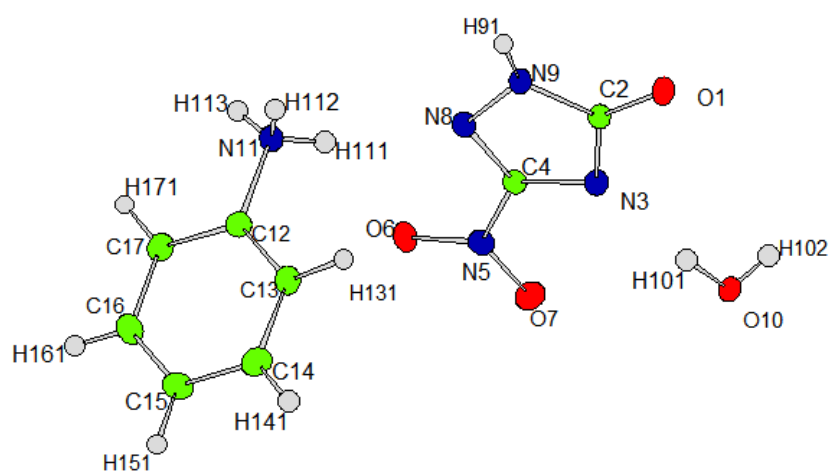


Fig 3.6 Labeled asymmetric unit of aniline.NTO

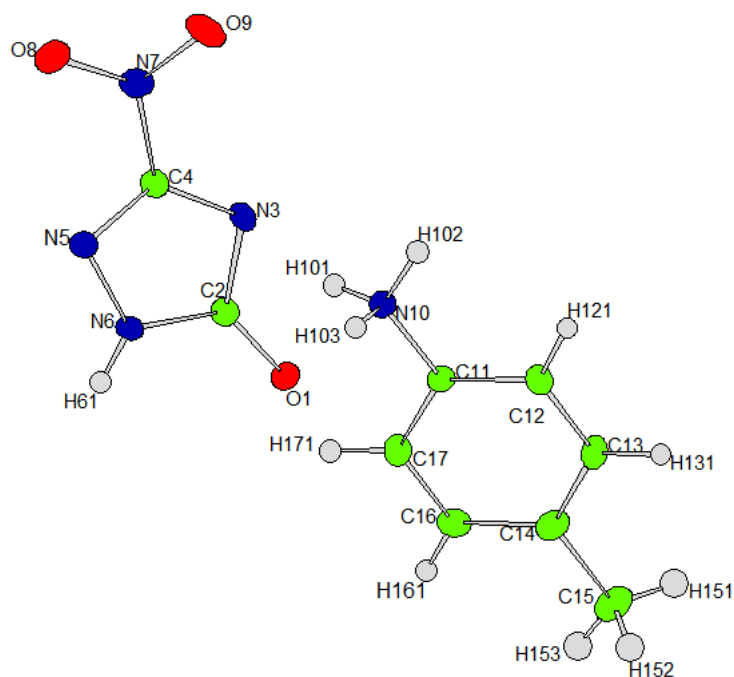


Fig 3.7 Labelled asymmetric unit of toluidine.NTO

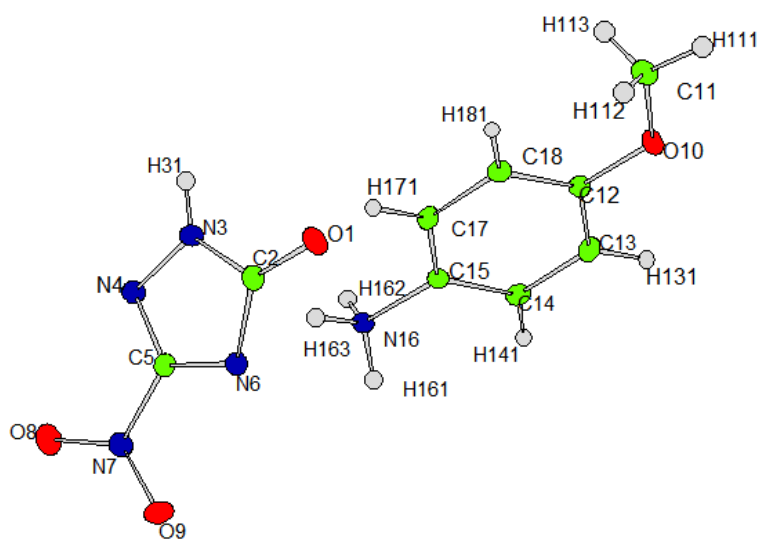


Fig 3.8 Labelled asymmetric unit of *p*-anisidine.NTO

3.3.1.2 Intermolecular Bonding and Structural Arrangements

The common feature shared by all of the salts is the amine-group and benzene ring. The benzene ring does not appear to contribute to the intermolecular interactions – there is no π - π stacking. Primary amine groups are good hydrogen-bond donors and are the sole contributing area for strong interactions between co-former and NTO in

all three crystal structures. The water molecule present in An.NTO is heavily involved in the hydrogen bonding and interacts with both the NTO^- and An^+ ions through moderately strong hydrogen bonding. This behaviour suggests that this contributes strongly to the stability of the structure.

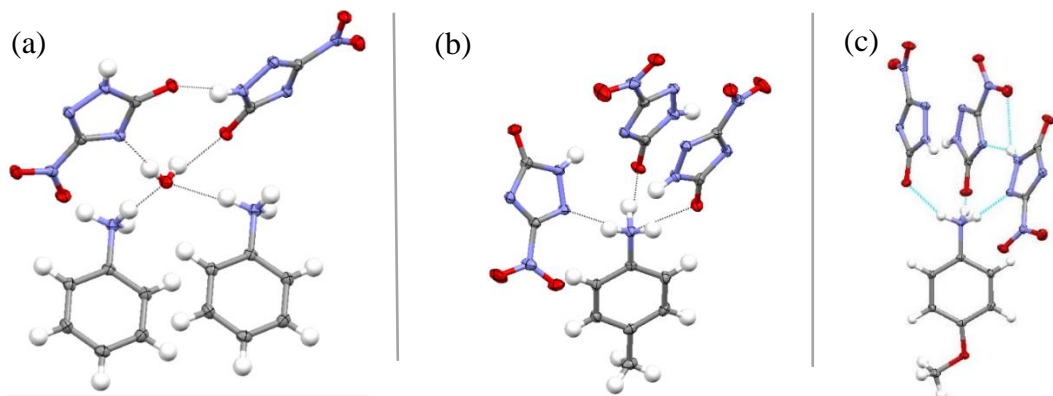


Fig 3.9 Hydrogen bonding present in An.NTO (a), Tol.NTO (b), and Ani.NTO (c)

Table 3.2 Hydrogen bonds lengths and angles between NTO^- and co-former

Salt	$D-H\cdots A$	$D-H$ [\AA]	$H\cdots A$ [\AA]	$D\cdots A$ [\AA]	$D-H\cdots A$ [$^\circ$]
An.NTO	N11-H111\cdotsO6	0.90 (2)	2.348 (2)	3.056 (2)	136.39(1)
	N1-H111\cdotsN8	0.90 (2)	2.258 (2)	3.046 (2)	147.17(1)
Tol.NTO	N10-H102\cdotsN5	0.91 (2)	2.019 (2)	2.877 (3)	157.8 (1)
	N10-H103\cdotsO1	0.92 (2)	1.749 (2)	2.659 (3)	168.5 (1)
	N10-H101\cdotsO1	0.90 (2)	1.903 (3)	2.737 (3)	152.1 (1)
Ani.NTO	N16-H161\cdotsN4	0.91 (1)	1.985 (2)	2.872 (2)	164.15 (1)
	N16-H162\cdotsO1	0.93 (2)	1.728 (2)	2.650 (2)	170.55 (1)
	N16-H163\cdotsO1	0.90 (1)	1.971 (2)	2.759 (2)	144.72 (1)
	N16-H163\cdotsO9	0.90 (1)	2.574 (2)	3.149 (2)	122.18 (1)

In the salt, aniline.NTO, there are two weak H-bonds between one donor atom on aniline ($-\text{NH}_2$) and two acceptor atoms ($-\text{C}=\text{O}$ and $\text{N}-\text{R}_2$) on NTO. Stronger H-bonds exist between aniline and water. Whilst Tol.NTO has three hydrogen bonds between the amine group and three NTO molecules and Ani.NTO has four hydrogen bonds between the amine-group and four NTO molecules. The interactions between the amine group hydrogen atoms and the oxygen atoms on NTO are short, moderate hydrogen bonds, with distances of 2.658 and 2.740 Å, respectively.

NTO^- ions forms 1D chains for all three salts. An.NTO and Tol.NTO possess a single H-bond connecting the chain, notably aniline.NTO has shorter and more directional H-bond. Ani.NTO shows a bifurcated H-bond between the NTO^- ions (Fig 3.10).

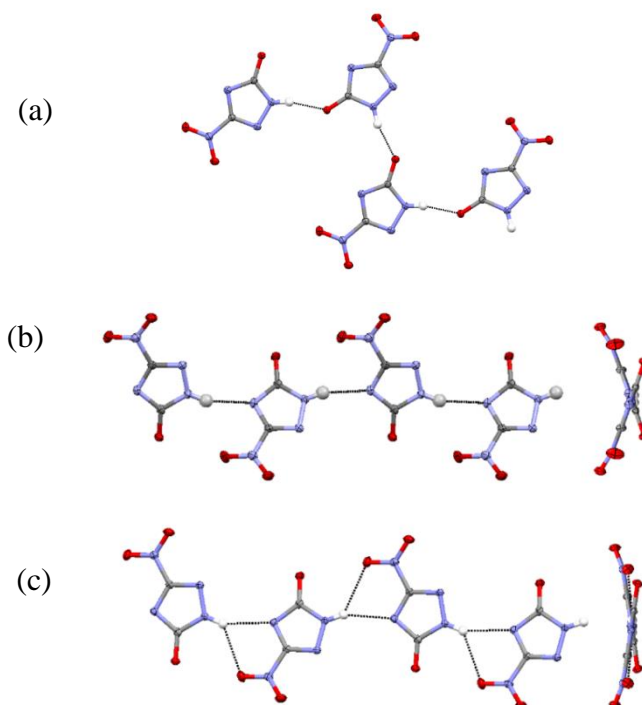


Fig 3.10 Hydrogen-bonded 1D chains of NTO^- anions in An.NTO (a), Tol.NTO (b), and Ani.NTO (c)

Table 3.3 Lengths and angles of interactions between NTO⁻ molecules through 1D chains

	<i>D-H</i> ⋯ <i>A</i>	<i>D-H</i> [Å]	<i>H</i> ⋯ <i>A</i> [Å]	<i>D</i> ⋯ <i>A</i> [Å]	<i>D-H</i> ⋯ <i>A</i> [°]
An.NTO	N-H ⋯ O	0.86 (2)	1.910 (2)	2.755 (2)	165.89 (1)
Tol.NTO	N-H ⋯ N	0.85 (2)	2.084 (3)	2.881 (3)	155.58 (1)
Ani.NTO	N-H ⋯ N	0.86 (2)	2.242 (2)	3.046 (2)	156.52 (1)
	N-H ⋯ O	0.86 (2)	2.509 (2)	3.151 (2)	132.57 (1)

The variety of interactions leads to unique crystal packing arrangements for each salt there are channels of NTO and co-former throughout structure. Key differences appear in how the NTO ions interact with each other, shown in the previous section.

Two-dimensional channels of NTO⁻ (red) and An⁺ (green) can be observed along the *a*- and *b*-axes, with water molecules connecting the NTO⁻ ions (Fig 3.12). Over the course of a month, the yellow crystals of An.NTO were allowed to stand open to the atmosphere at room temperature and deposits of white starting material appeared as the salt dehydrated. This is a strong indication that water is key to holding the structure together. NTO⁻ ions are layered, with a distance of 2.895 Å between each layer.

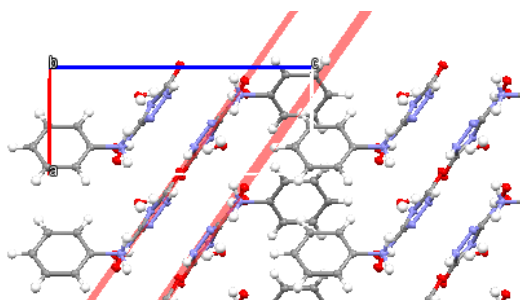


Fig 3.11 Crystal structure of An.NTO, with planar layers of NTO⁻ and water molecules indicated in red.

In Tol.NTO the NTO⁻ ions align in 1D chains (Figure 3.10) that are connected by hydrogen bonding in alternating directions (180°). The chains stack in staggered formations throughout the structure along the *c*-axis, forming a crisscrossing layer.

Ani.NTO has a very similar packing arrangement as Tol.NTO, with the same crisscrossing of hydrogen-bonded chains, however, they are not isostructural. In addition, channels of anions and cations form throughout the structure of all three salts, An.NTO, Tol.NTO and Ani.NTO.

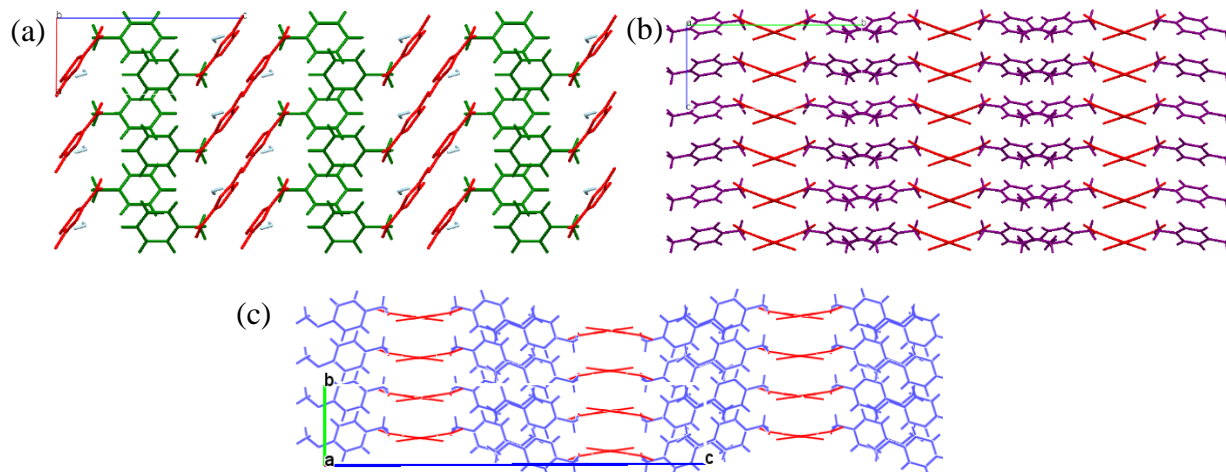


Fig 3.12 Crystal structure packing in An.NTO (a), Tol.NTO (b), and Ani.NTO (c)

3.3.2 Salts formed between NTO and N-heterocycles.

To date, six NTO salts containing substituted pyridines; have been obtained by evaporative crystallisation. The co-formers of the salts are melamine, 2-amino-3-picoline, pyridine, 3-bromopyridine, 3-chloropyridine and piperazine - all 6-membered rings with nitrogen-based functionality.

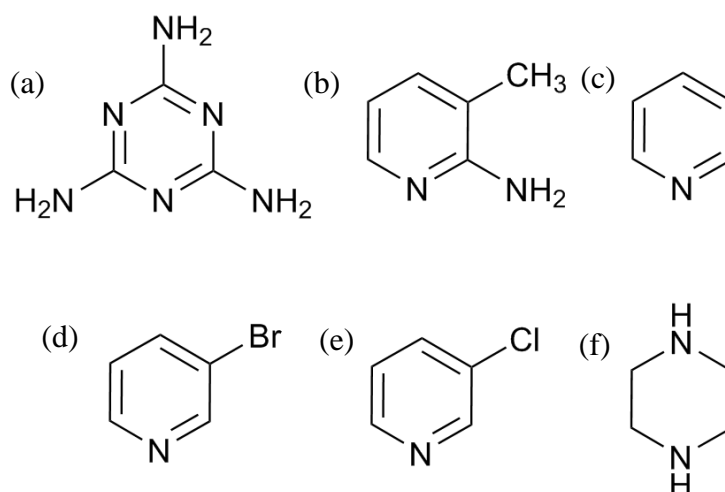


Fig 3.13 Molecular structures of melamine (a), 2-amino-3-picoline (b), pyridine (c), 3-bromopyridine (d), 3-chloropyridine (e) and piperazine (f)

Table 3.4 Crystallographic information for Mel.NTO, AP.NTO, Py.NTO, BrPy.NTO, ClPy.NTO and Pip.NTO

	Mel.NTO	AP.NTO	Py.NTO	BrPy.NTO	ClPy.NTO	Pip.NTO
Formula	C ₅ H ₁₀ N ₁₀ O ₄	C ₈ H ₁₀ N ₆ O ₃	C ₇ H ₇ N ₅ O ₃	C ₇ H ₆ N ₅ O ₃ Br	C ₇ H ₆ N ₅ O ₃ Cl	C ₈ H ₁₄ N ₁₀ O ₆
Mr [g.mol⁻¹]	274.20	238.20	209.16	288.06	243.61	346.26
Crystal System	Monoclinic	Monoclinic	Monoclinic	Triclinic	Triclinic	Monoclinic
Space Group	<i>P2₁/m</i>	<i>P2₁/n</i>	<i>C2/c</i>	<i>P1-</i>	<i>P1-</i>	<i>P2₁/n</i>
<i>a</i> (Å)	9.194 (10)	15.767	18.618 (16)	6.563 (4)	3.665 (2)	6.666 (3)
<i>b</i> (Å)	6.137 (7)	9.237	3.720 (3)	7.016 (4)	9.657 (4)	12.522 (6)
<i>c</i> (Å)	9.385 (10)	7.074	25.845 (2)	10.829 (7)	13.863 (7)	8.556 (4)
<i>α</i> (°)	90	90	90	94.871 (5)	102.007 (4)	90
<i>β</i> (°)	95.860 (10)	77.801	103.050 (9)	104.672 (5)	95.525 (5)	108.461 (2)
<i>γ</i> (°)	90	90	90	93.319 (5)	100.007 (4)	90
<i>V</i> (Å³)	526.80	1006.93	1743.69	478.95	468.61	677.42
<i>ρ</i> (g.cm⁻³)	1.729	1.57	1.586	1.997	1.728	1.70
<i>Z</i>	4	4	8	2	2	4
R-Factor (%)	7.61	9.00	5.78	2.39	4.51	3.03
Diffraction Method	Single-crystal XRD	Powder XRD	Single-crystal XRD	Single-crystal XRD	Single-crystal XRD	Single-crystal XRD

3.3.2.1 Asymmetric Units

Single crystal data were collected for all of the salts apart from AP.NTO for which PXRD data were collected and the structure solved using TOPAS. In contrast to the salts with substituted anilines (Section 3.3.1), all NTO salts containing pyridine derivatives have a protonated nitrogen atom within the unsaturated heterocyclic ring

rather than the primary amine. Pip.NTO is an anomaly since the piperazine molecule is a non-planar saturated ring with two heteroatoms - both of which are protonated.

Mel.NTO has previously been reported, yet not characterised using single-crystal X-ray diffraction. The hypothesised structure is partly inaccurate, as the primary amine is not protonated, however the assumption made in a previous work [7] that water is present within the structure is true.

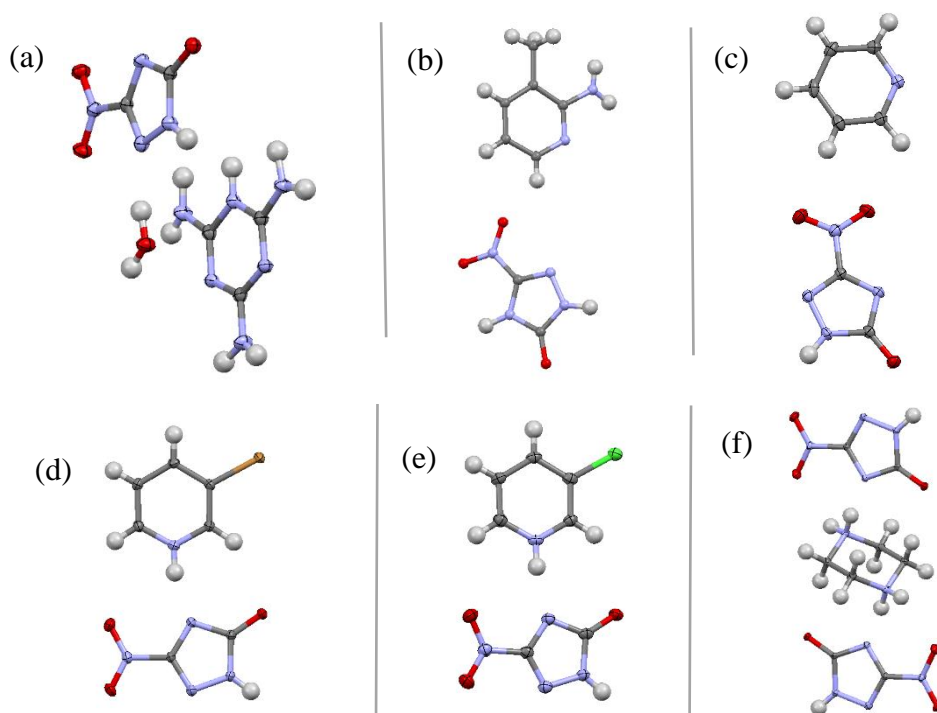


Fig 3.14 Asymmetric units of (a) melamine.NTO, (b) pyridine.NTO, (c) 2-amino-3-picoline.NTO, (d) 3-bromopyridine.NTO, (e) 3-chloropyridine.NTO, and expanded asymmetric unit of (f) piperazine.NTO

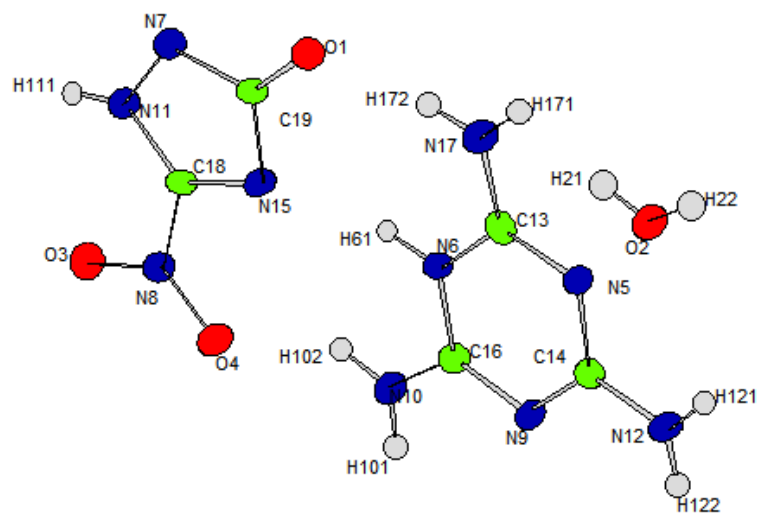


Fig 3.15 Labeled asymmetric unit of Mel.NTO

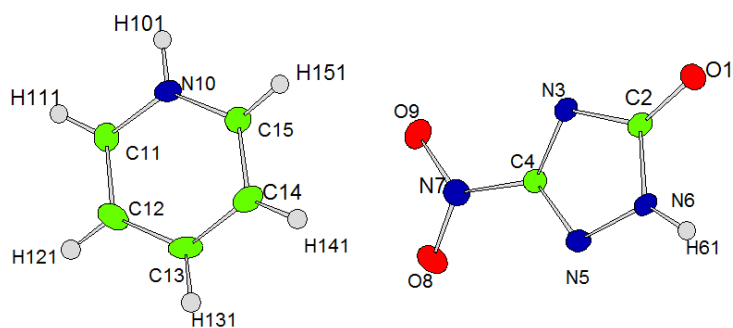


Fig 3.16 Labeled asymmetric unit of Py.NTO

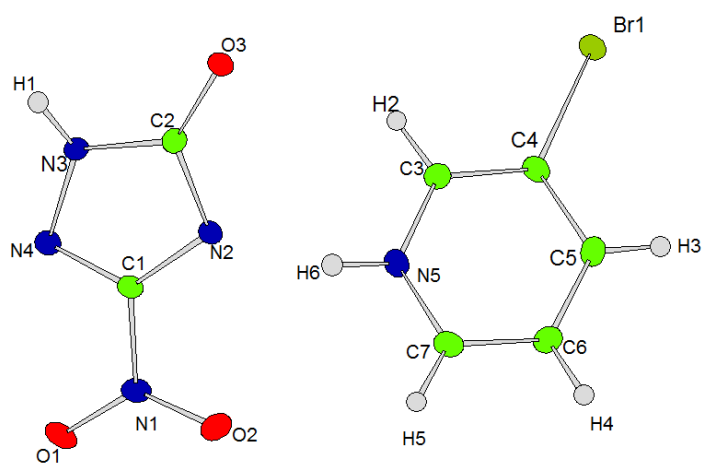


Fig 3.17 Labeled asymmetric unit of BrPy.NTO

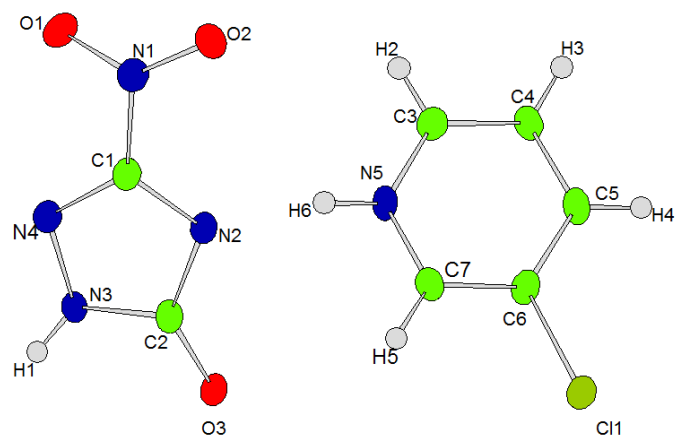
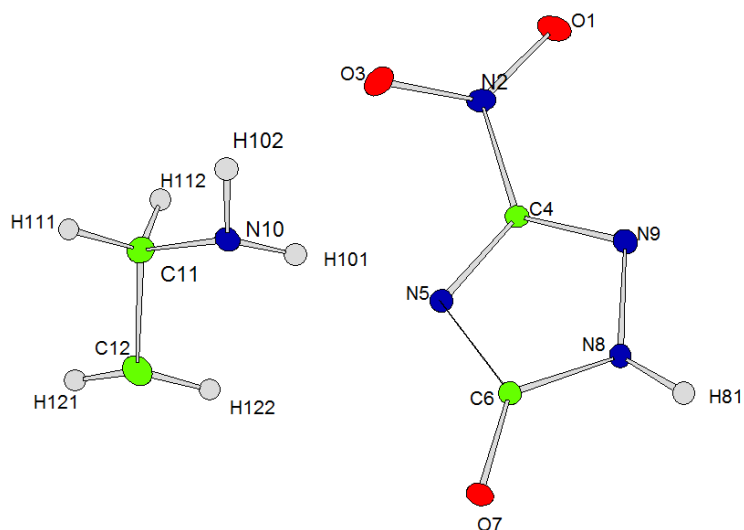


Fig 3.18 Labelled asymmetric unit of CIPy.NTO



Furthermore the addition of halogen functionality opens up prospect of halogen bonding, which can be observed in BrPy.NTO and ClPy.NTO.

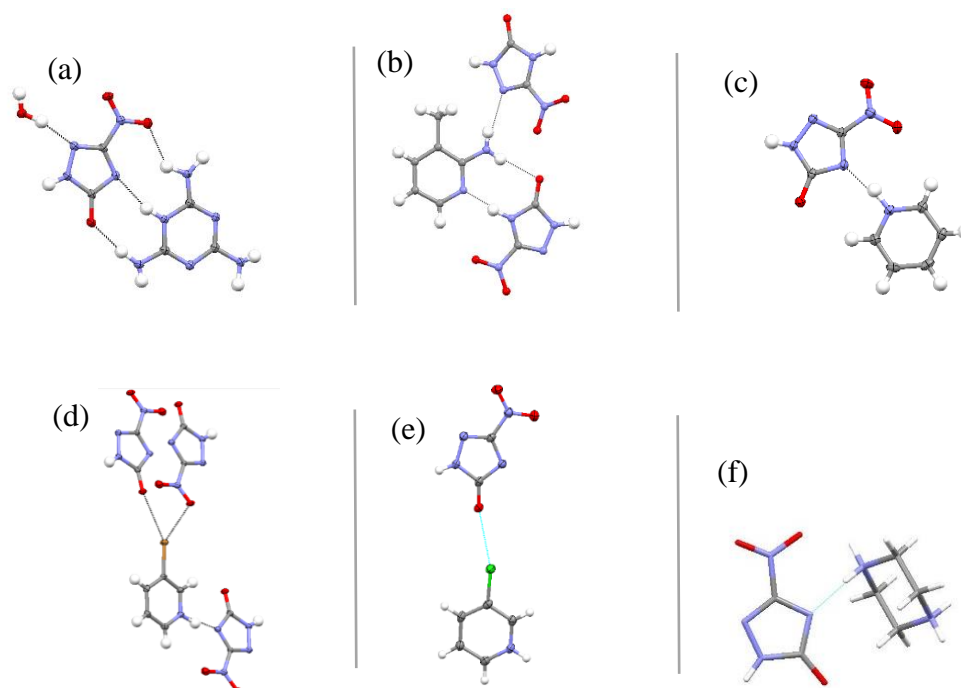


Fig 3.20 Important hydrogen-bonding between NTO and co-formers. (a) melamine.NTO, (b) pyridine.NTO, (c) 2-amino-3-picoline.NTO, (d) 3-bromopyridine.NTO, (e) 3-chloropyridine.NTO, (f) piperazine.NTO

There are multiple hydrogen bonds between NTO^- and Mel^+ resulting in the formation of planar sheets. However, these hydrogen bonds are relatively weak.

For AP.NTO, owing to the limitations of powder X-ray diffraction, it is difficult to identify the position of the proton and therefore whether the structure is a salt or a co-crystal; but based on ΔpK_a of 3.57 (Py.NTO salt has a lower value of 1.51) and colour (yellow), it is clear that a salt has been formed. It is easy to see that there is a hydrogen bond present (2.782 Å) between the deprotonated nitrotriazolone (NTO^-) and the tertiary nitrogen on 2-amino-3-picoline (Figure 3.20). This is very similar to the behaviour of the salts based on that of melamine and pyridine. For this material, ΔpK_a is approximately 3, which lies in the indefinite region of the ΔpK_a rule ($\Delta pK_a > 4$ results in a salt, $\Delta pK_a < -1$ in a co-crystal). However, Py.NTO, ClPy.NTO and BrPy.NTO are salts and have ΔpK_a values lower than 3. Spectroscopic methods can be conducted to further confirm the hydrogen position.

Py.NTO contains a pair of hydrogen bonds between two NTO⁻ ions, and a single relatively strong hydrogen bond between Py⁺ and NTO⁻. The lack of functionality on pyridine creates a bulky hindrance which blocks further interactions.

The asymmetric unit of Pip.NTO includes one NTO molecule and half a piperazinium molecule, resulting in a 2:1 molecular ratio (NTO:Pip).

Table 3.5 Hydrogen bonds lengths and angles between NTO⁻ and co-former

	<i>D-H...A</i>	<i>D-H</i> [Å]	<i>H...A</i> [Å]	<i>D...A</i> [Å]	<i>D-H...A</i> [°]
Mel.NTO	N6-H10...N2	0.99 (2)	2.021 (1)	2.939 (1)	164.37 (3)
	N9-H3...O1	0.94 (2)	2.099 (1)	2.877 (1)	133.51 (3)
	N10-H7...O3	0.97 (2)	1.876 (1)	2.841 (1)	172.17 (3)
	O4-H9...N4	0.96 (2)	1.851 (1)	2.794 (1)	165.78 (3)
AP.NTO	N1-H6...N5	1.01 (3)	1.781 (1)	2.782 (1)	170.56 (3)
	N10-H11...O3	0.86 (3)	2.186 (1)	3.035 (1)	168.99 (3)
	N10-H12...N4	0.86 (3)	2.265 (1)	3.100 (1)	163.64 (3)
Py.NTO	N5-H2...N2	1.04 (1)	1.651 (1)	2.670 (2)	165.30 (3)
Pip.NTO	N10-H101...N5	0.90 (4)	1.978 (4)	2.877 (5)	175.39 (3)
BrPy.NTO	N5-H6...N2	0.90 (1)	1.751 (1)	2.623 (2)	163.53 (3)
ClPy.NTO	N5-H6...N2	0.88 (1)	1.775 (1)	2.641 (1)	167.55 (3)

Halogen bonding exists in BrPyNTO and ClPyNTO. This is where a halogen acts as an electrophilic species and interacts with a Lewis base. For ClPy.NTO and BrPy.NTO salts, the electron pair donor involved in halogen-bonding is the oxygen atoms on two separate NTO⁻ ions. ClPy.NTO has a shorter and more directional halogen bond than the two halogen bonds shown in BrPy.NTO. However, both are very weak halogen bonds, which is likely due to the nature of the pyridine ring, which diffuses interactions.

It is difficult to discern whether ClPy.NTO is a co-crystal or salt. Electron density maps have been created and show an elongated spread of density where a

hydrogen atom is expected. In comparison, BrPy.NTO has a clearly defined proton position, closer to the bromopyridine than NTO. These observations are logical considering the ΔpK_a for each complex. BrPy.NTO has a pK_a difference of -0.75, whereas ClPy.NTO has a lower difference of -0.85. Neutron diffraction studies are required to accurately determine the proton position in ClPy.NTO and confirm whether it is a salt or co-crystal.

Table 3.6 Halogen bonds lengths and angles between NTO⁻ and co-former

	<i>D-Hal</i> ... <i>A</i>	<i>D-Hal</i> [Å]	<i>Hal</i> ... <i>A</i> [Å]	<i>D</i> ... <i>A</i> [Å]	<i>D-Hal</i> ... <i>A</i> [°]
BrPy.NTO	C-Br ... O	1.88 (3)	3.040 (1)	4.817 (2)	155.63 (3)
ClPy.NTO	C-Cl ... O	1.72 (3)	2.953 (1)	4.634 (1)	164.02 (3)

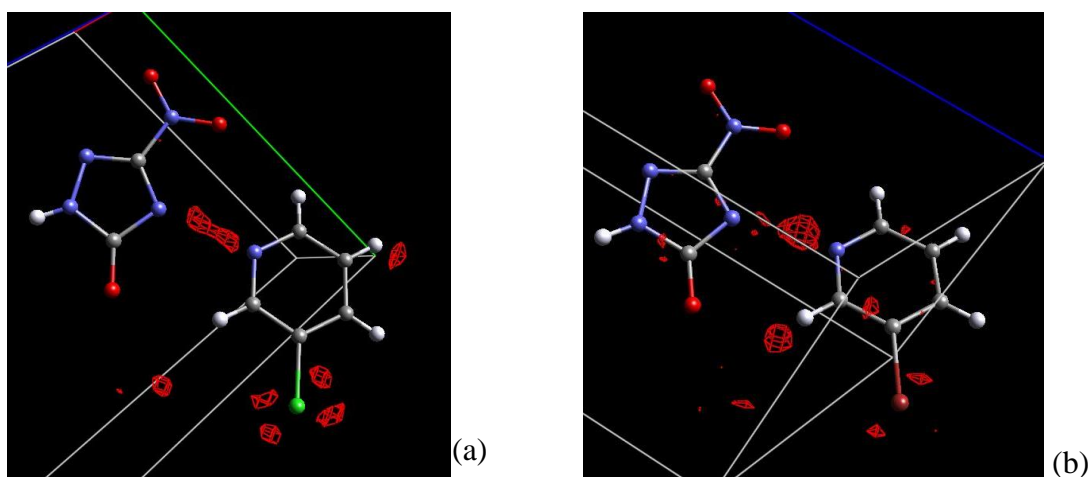


Fig 3.21 Electron density map for (a) 3-chloropyridine.NTO and (b) 3-bromopyridine.NTO. Calculated in CRYSTALS.

A range of packing features are shown in the NTO salts containing pyridine derivatives. The packing of AP.NTO comprises pairs of NTO⁻ ions in planes, surrounded by AP⁺ molecules at various angles. This unit is repeated at 45 ° relative to itself throughout. The extended packing structure resembles a zig-zag or chevron arrangement when focusing on the NTO⁻ molecules (Figure 3.22).

Melamine.NTO has a layered structure, similar to that of TATB. The distance between each layer is 3.069(2) Å.

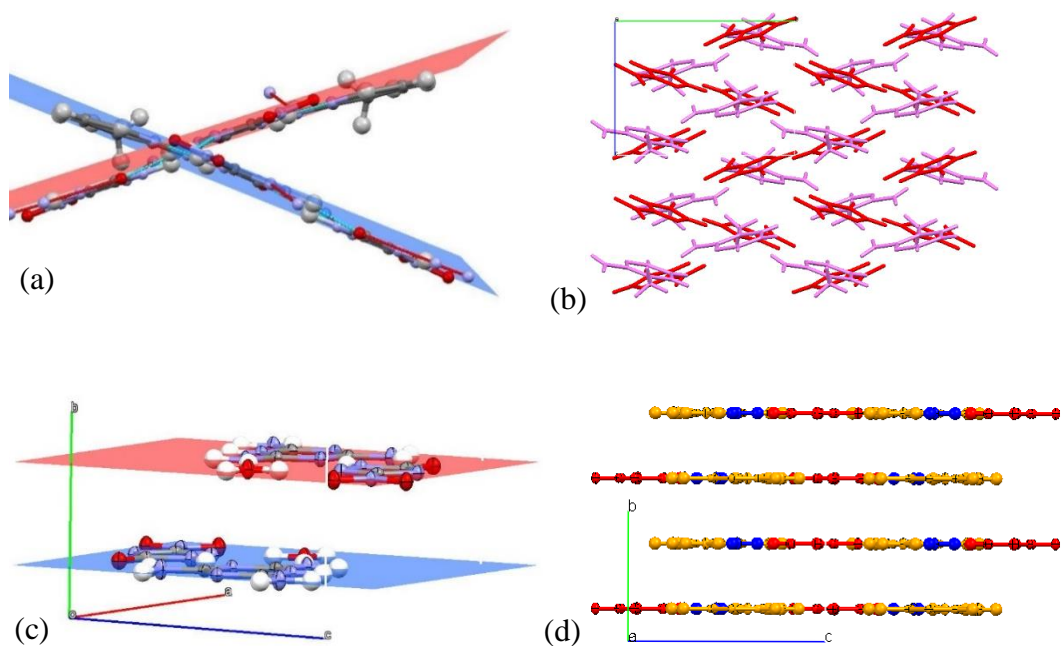


Fig 3.22 (a) Calculated planes indicating planar NTO^- pairs in AP.NTO, (b) crystal structure packing of AP.NTO, (c) calculated planes indicating planar sheets of NTO^- , Mel^+ and H_2O , (d) crystal structure packing of Mel.NTO

Piperazine is the only co-former that is not planar, and this is reflected in the packing structure of Pip.NTO. The structure contains π -stacked pairs of NTO^- ions, shown in Figure 3.23, with an inter-ion distance of 3.042 Å. A piperazinium ion links these pairs, creating a column of NTO anions.

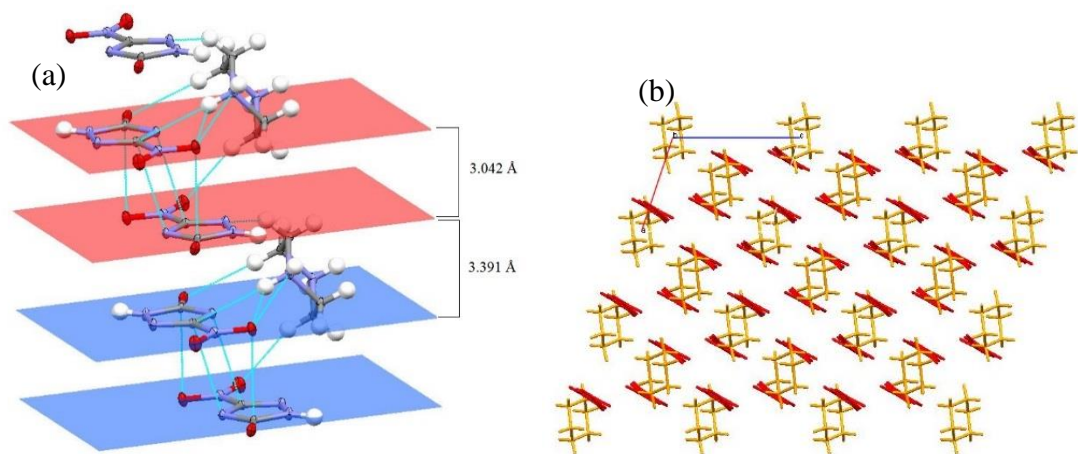


Fig 3.23 (a) Calculated planes indicating NTO^- stacking in Pip.NTO (b) crystal structure packing of Pip.NTO

The structure of Py.NTO has fewer interactions throughout in comparison to other salts. This is due to the lack of functional groups that would aid H-bonding. Py.NTO is built of bisecting NTO^- chains with pyridinium molecules acting as interaction blockers. These chains form a “wine-rack” structure. Such structures are as the namesake states, similar to a collapsible wine-rack, which are crossed over structures with gaps in the centre. Wine-rack structures are known for being compressible in one direction (decreasing the angle to $< 60^\circ$), causing an extension in the perpendicular direction, and vice versa. External conditions, such as pressure or temperature are required to observe this expansion and contraction of the unit cell. To ascertain whether this situation occurs in Py.NTO, single crystal X-ray diffraction data was also collected at a range of temperatures (200, 250 and 300 K).

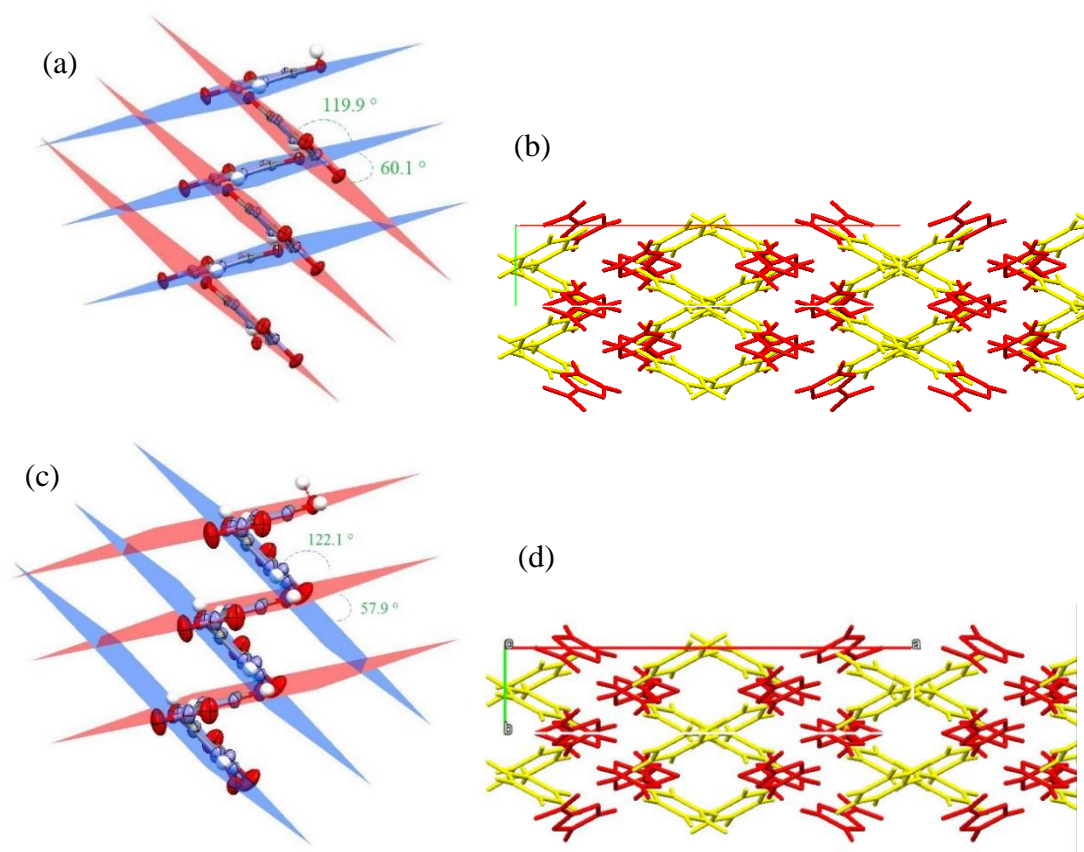


Fig 3.24 (a) Calculated planes indicating zig-zag relationship of NTO^- packing in Py.NTO at 120 K, (b) crystal structure packing of Py.NTO at 120 K (c) Calculated planes indicating zig-zag relationship of NTO^- packing in Py.NTO at 250 K (d) crystal structure packing of Py.NTO at 250 K

As temperature increases, thermal expansion is observed with the b - and c -axes (2.4 % and 1.7 %, respectively), while thermal contraction occurs along the a -axis (-0.5 %). This was expected behaviour for this structure. The angles within the cross-overs of the structure alter with increasing temperature, as shown in Fig 3.24. It would be interesting to investigate this system under pressure, to obtain an equation of state with respect to pressure, and to better understand the compressibility of the system.

Table 3.7 Unit cell parameters of Py.NTO with increasing temperature

	120 K	200 K	250 K	300 K
a (Å)	18.618 (2)	18.577 (3)	18.547 (2)	18.518 (2)
b (Å)	3.720 (3)	3.750 (1)	3.774 (1)	3.800 (1)
c (Å)	25.845 (2)	26.024 (4)	26.152 (2)	26.287 (2)
β (°)	103.05 (1)	103.25 (2)	103.44 (1)	103.66 (1)
V (Å ³)	1743.7	1764.7	1778.5	1797.4
ρ (g.cm ⁻³)	1.593	1.574	1.561	1.546
R (%)	5.36	3.2	3.43	3.59

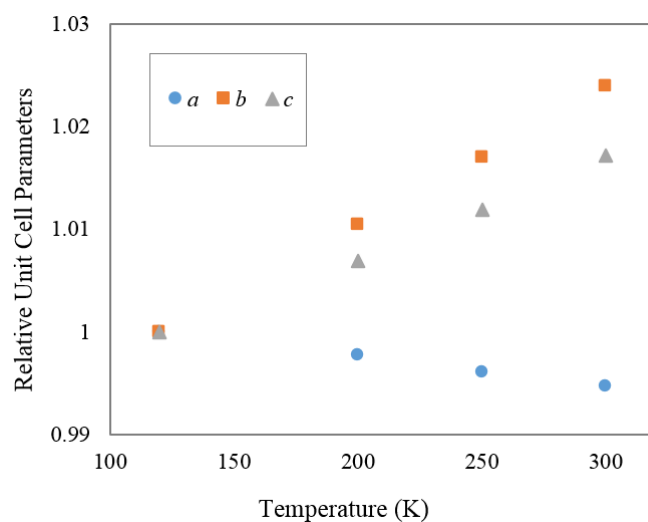


Fig 3.25 Relative unit cell parameters in Py.NTO with varying temperature

The crystal structures of BrPy.NTO and ClPy.NTO are similar in a certain direction, and are not isostructural. Both possess variations of planar NTO⁻ layers, which expand throughout the structure. Within the BrPy.NTO salt, the bromopyridinium ion sits out of the plane further than the chloropyridinium ion does in ClPy.NTO. The distances between each layer are 3.151 and 3.183 Å for BrPy.NTO and ClPy.NTO respectively.

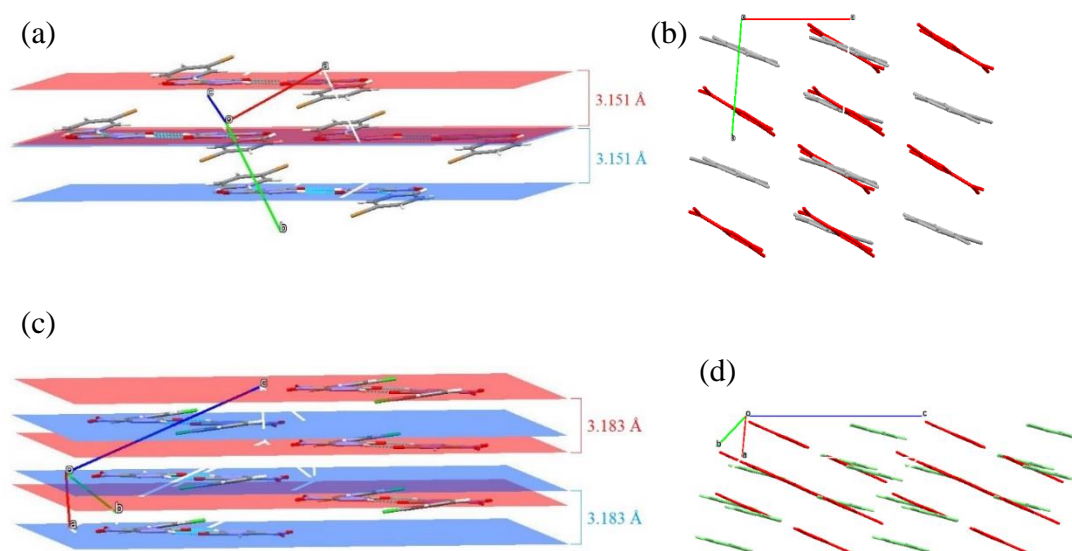


Fig 3.26 (a) Calculated planes indicating layered packing in BrPy.NTO (b) crystal structure packing of BrPy.NTO (c) Calculated planes indicating layered packing in ClPy.NTO (d) crystal structure packing of ClPy.NTO

3.3.3 Property Testing

The ESEM observations show that co-crystallisation of NTO with other materials significantly changes the crystal morphology. NTO forms large plate-like crystals, whilst APNTO produces very small crystals which agglomerate together.

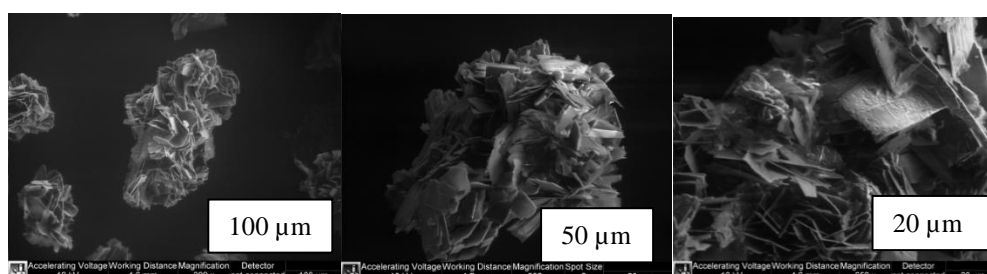


Fig 3.27 ESEM images of NTO at 100 μm, 50 μm and 20 μm

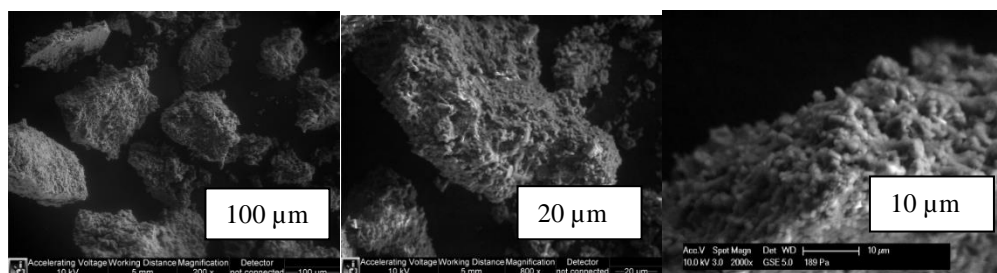


Fig 3.28 ESEM images of APNTO at 100 μm , 20 μm and 10 μm

Table 3.8 Physical properties of NTO salts

	Impact (J)	T_p^a (K)	Density^b (g/cm³)	ΔH_f^c (kJ/mol)	D^d (m/s)	P^e (GPa)
AP.NTO	>100	253.3	1.570	-518.02	5285.86	9.009
MeI.NTO	>100	316.5 ^f	1.730	-66.10	5705.14	8.820
Py.NTO	20.3	190.8	1.590	-457.98	5034.69	9.953
Pip.NTO	10.9	274.4	1.697	-686.29	6449.17	13.13
BrPy.NTO	>100	-	1.997	-419.45	5055.40	15.45
ClPy.NTO	>100	199.3	1.728	-481.86	5447.89	9.512

a – peak temperature of exothermic peak obtained by DSC. b – calculated from single crystal data. c – enthalpy of formation calculated. d, e – detonation velocity and pressure calculated in EXPLO5 using crystal density and enthalpy of formation, f – literature value [3]

Impact sensitivity has been performed on all NTO salts with pyridine-based co-formers. Many are insensitive, with no signs of initiation up to the testing limit of 100 J, which is similar to NTO. These insensitive NTO salts are displayed in Table 3.8. Each salt's insensitivity to impact can potentially be linked to features within the packing structure. MeI.NTO, BrPy.NTO and ClPy.NTO all exhibit forms of layered structures, similar to TATB – one of the most insensitive conventional energetic materials.

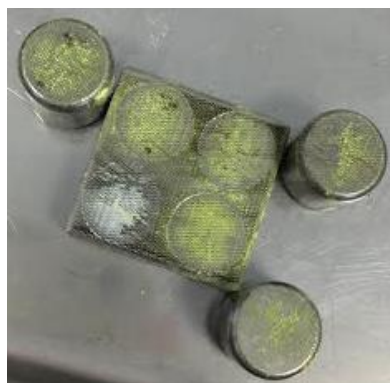


Fig 3.29 BFH-12 impact testing using impact device 2; white NTO (100 J) and pale yellow 2-Amino-3-picoline.NTO (100 J)

In contrast, AP.NTO does not have a layered structure, yet is just as insensitive. It is worth noting that the crystal grain size of AP.NTO ($< 100 \mu\text{m}$) is very fine in comparison to the standard grain size for testing ($200 \mu\text{m}$) [15]. Therefore this could potentially contribute to a decrease in sensitivity, though there are conflicting reports as to how grain size effects sensitivity [16]. Further testing was conducted on 2-amino-3-picoline.NTO, using device 2, a file plate to increase energy inputted by inducing friction. Results showed AP.NTO demonstrates a similar sensitivity to NTO (Figure 3.29), with evidence of scorch marks.

PyNTO and Pip.NTO have unusual impact sensitivities. Both PyNTO and PipNTO were tested using the 30-trial Bruceton method [9], with a load of 5 kg. These are shown in Tables 3.9 and 3.10. Statistical analysis of the trial results show Pip.NTO has an impact sensitivity of $H_{50} = 21.7 \text{ cm}$ (s.d. 1.235), while Py.NTO has $H_{50} = 40.6 \text{ cm}$ (s.d. 1.081). The outcomes of the experiments imply it is possible to reduce sensitivity by crystallising NTO with a co-former. This is not regularly seen in organic salts, so is of great interest.

Table 3.9 Bruceton method testing on Pip.NTO with a 5 kg load

H (cm)	Individual Trial Results										$\sum n_x$	$\sum n_o$	I
16						O	O				0	2	0
18			O	O	O	X	O				1	4	1
20	O		O	X	O	X	O		O	O	2	6	2
22	O	O	X		X		X	O	X	O	4	4	3
25	X	O	X				X	X		X	5	1	4
28		X									1	0	5
Totals N_x and N_o											13	17	

Table 3.10 Bruceton method testing on Py.NTO with a 5 kg load

H (cm)	Individual Trial Results										$\sum n_x$	$\sum n_o$	I
32	O					O				O	0	3	0
36	O	O		O	O	O	O	O	O	O	0	9	1
40	X	O	O	X	O	X	X	X	O	O	5	5	2
45	X	X	O		X	X			X	X	6	1	3
50			X								1	0	4
Totals N_x and N_o											12	18	

DSC measurements were performed on NTO salts to obtain data on their thermal stability. For AP.NTO and Pip.NTO a sharp single exothermic peak is observed. These are interpreted to be decomposition peaks of the salt as an entity. The onset temperature and peak maximum for AP.NTO are 248.9 °C and 253.3 °C, respectively, with a calculated heat of decomposition of 485.1 J/g. The peak temperature of decomposition is lower than that of pure NTO (253 to 279 °C depending on experimental conditions) [17]. In contrast Pip.NTO has a higher decomposition peak which onsets at 271.9 °C, with a peak max at 274.4 °C. Calculated heat of decomposition is 460.6 J/g. Hence it appears from the data that Pip.NTO has improved thermal stability to NTO.

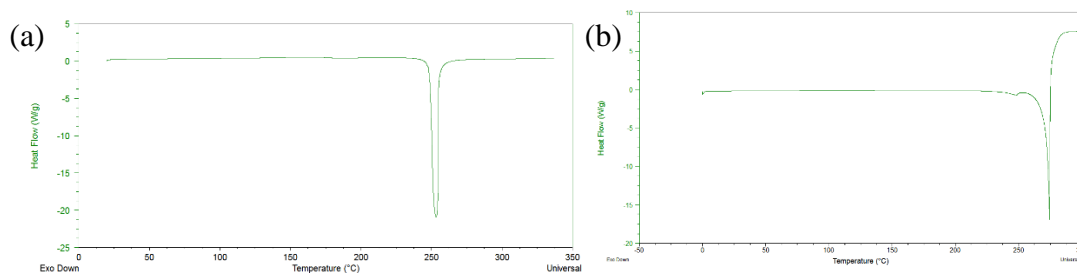


Fig 3.30 DSC plots of AP.NTO (a) and Pip.NTO (b)

Py.NTO possesses a complex curve which is difficult to interpret accurately without TGA weight data alongside. However, assumptions can be made and intelligent deductions explained. At 162.4 °C a relatively sharp endothermic peak of 149.5 J/g occurs with a peak temperature of 164.3 °C – this is perhaps indicative of loss of pyridine vapour (the boiling point of pyridine is 115.2 °C [18]). A broad exothermic peak subsequently follows the endothermic peak with an onset temperature of 177.9 °C and a peak temperature at 191.4 °C. This suggests that either NTO or the salt has decomposed. Within the broad exothermic peak is a small endothermic peak, which is possibly an artefact produced during testing, or potentially a solid-solid phase change occurring during decomposition. The overall exothermic decomposition enthalpy is 1499 J/g. Finally, a very sharp endothermic peak occurs with extrapolated onset temperature (T_e) peak temperature (T_p) and endotherm of 250.0 °C, 250.1 °C and 93.2 J/g, respectively. It is unclear what this peak represents, although it could correspond to a melt of materials produced through decomposition.

This endothermic peak is also observed at $T_e = 249.3$, $T_p = 249.5$ in 3-ClPy.NTO. 3-Chloropyridine.NTO also has a complex DSC curve. An endothermic peak is observed at approximately 148.3 °C, with a peak temperature of 150.5 °C which is representative of the boiling point of 3-chloropyridine, ~148 °C [19]. The decomposition of 3-ClPy.NTO appears to be unusual, with a secondary chemical reaction occurring within the exothermic peak. The overall extrapolated measurements gathered from the peak are shown in Table 3.8.

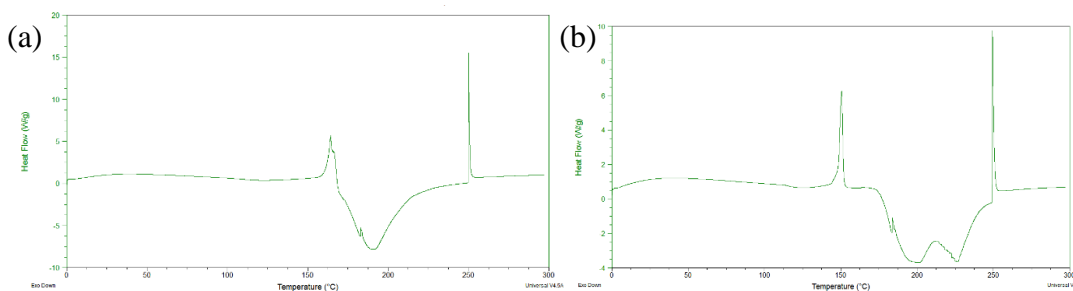


Fig 3.31 DSC plots of Py.NTO (a) and ClPy.NTO (b)

The salt Mel.NTO was reported to undergo two main stages of thermal decomposition [7], using DSC at 20 K/min. Firstly an endothermic process occurs between 116-200 °C, corresponding to the loss of water. Following this process, a sharp exothermic peak is observed at 316.5 °C. This decomposition peak is at a much higher temperature than that seen for NTO (253 to 279 °C). It is possible that that the strong hydrogen-bonded layers are responsible for this increase in stability.

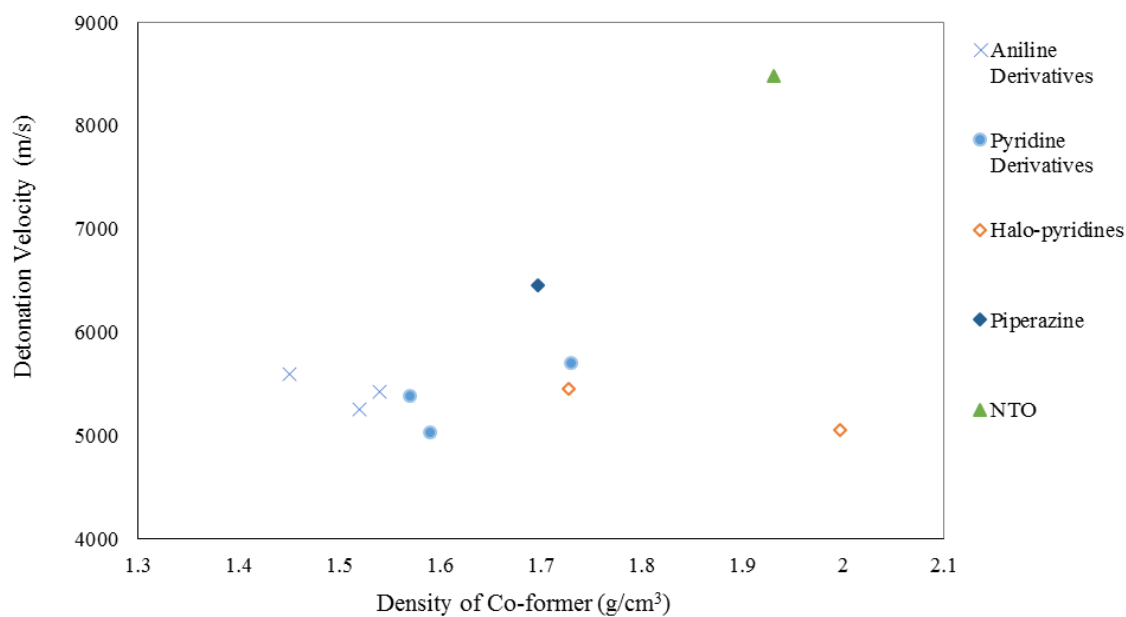


Fig 3.32 Plot of crystal density against detonation velocity for NTO salts. Co-former types are set into categories.

The general trend that detonation velocity increases with crystal density, does not appear to apply for the majority of the NTO salts that have been studied here (Fig.

3.32). The only salts that fits the trend is piperazine, which has an elevated detonation velocity that matches crystal density.

Halogen pyridines have a higher crystal density, however this is due to the high atomic density of the halogen atoms. The crystal packing is relatively low – halogen bonding does exist, however interaction distances are large. VoD calculations confirm the higher crystal density is not related to a high VoD parameters. Therefore, halogen atoms do not improve detonations parameters. It is possible that the packing coefficient would be more relevant for comparison and analysing of trends instead of crystal structure density.

The lack of data points makes it difficult to form any trends or conclusions as to how functionality effects the crystal density-detonation velocity relationship. Therefore more X-ray diffraction data on NTO salts containing aniline derivatives is required, along with a wider range of pyridine based salts of NTO.

3.3.4 Trends and Relationships

For Fig. 3.33 it is evident that for nearly all the investigated salts of NTO, their crystal densities lie approximately midway between those of NTO and the individual co-former. There are two anomalies to this trend: BrPy.NTO and ClPy.NTO. The crystal density of these salts is larger than expected, and in the case of BrPy.NTO the density is greater than that of pure NTO. The high density of BrPyNTO can be explained due to halogen bonding – which is not observed in pure bromopyridine. Pip.NTO has a greater than median density relative to NTO and Pip, though still lower than that of NTO alone, yet is a 2:1 complex with twice as much NTO.

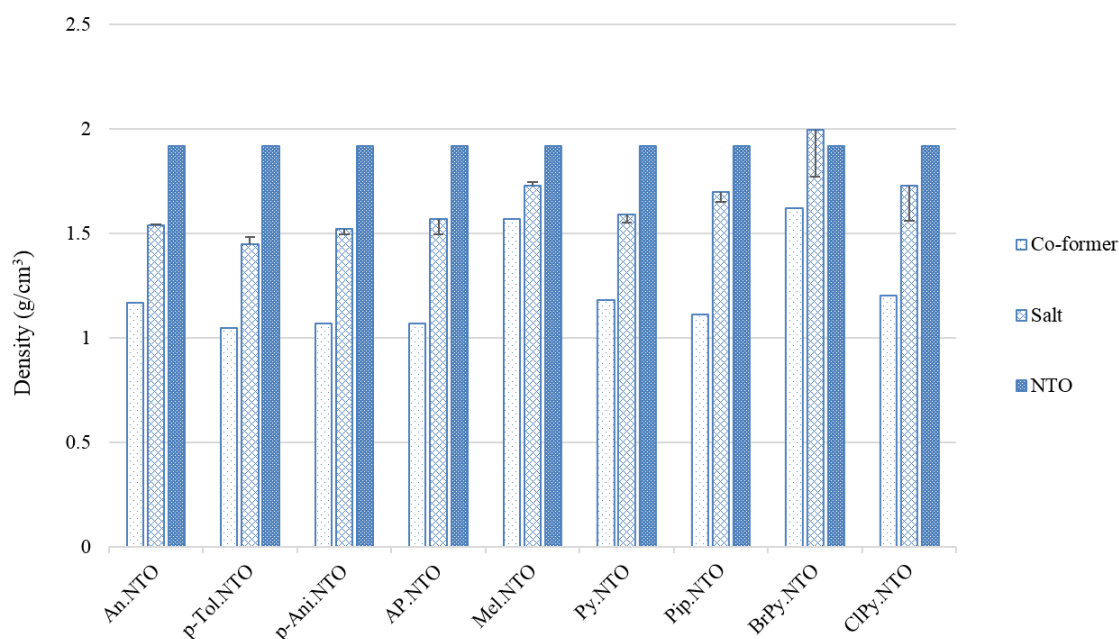


Fig 3.33 Crystal density of co-former (aniline, *p*-toluidine, *p*-anisidine, 2-amino-3-picoline, pyridine, melamine, 3-bromopyridine, 3-chloropyridine, piperazine), the resultant salts and the crystal density of NTO.

Another trend noted is one regarding the difference in pK_a and interaction distance between the protonated and deprotonated nitrogen atoms, on the co-former and NTO respectively. It appears the interaction distance decreases with reducing pK_a difference. Therefore it is possible to tentatively estimate this interaction distance between NTO and a potential co-former, based on the ΔpK_a of the components. This is a further step towards the specific design and engineering of salts and co-crystals.

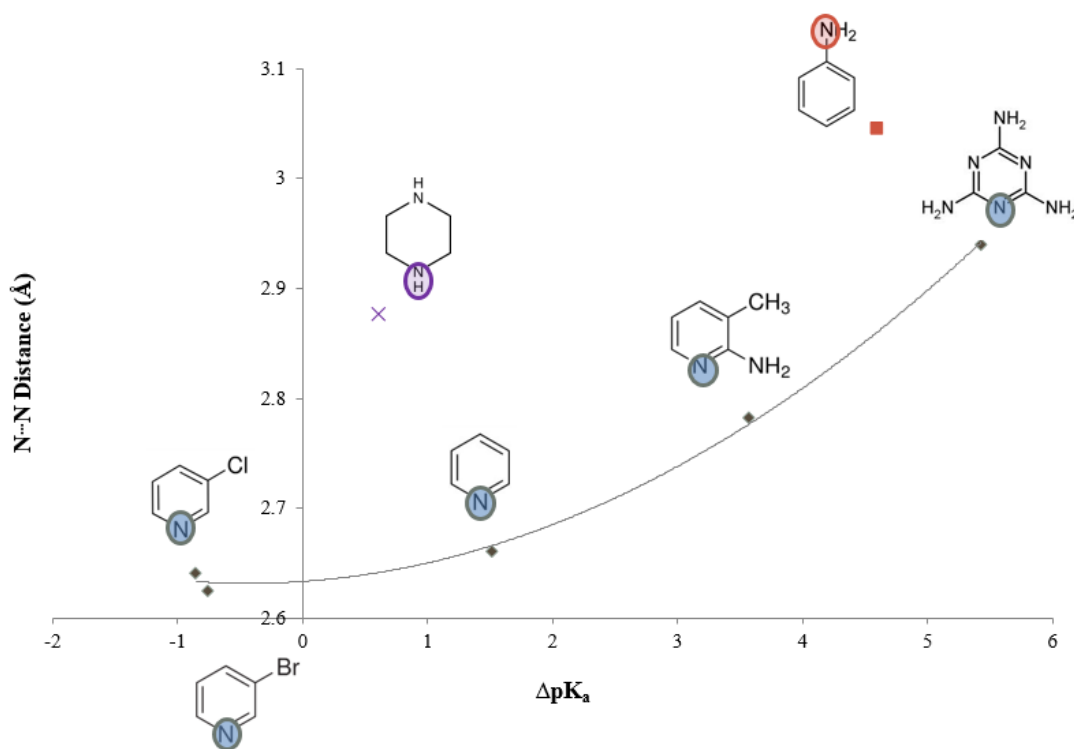


Fig 3.34 Plot of pK_a difference against $N\cdots N$ interaction distance. $N\cdots N$ interaction between deprotonated nitrogen atom on NTO and protonated nitrogen atom on co-former.

3.4 Conclusions

A series of arylammonium.NTO salts were successfully obtained. These materials were confirmed as salts, in line with the expectations of Singh [5,6]. However, Aniline.NTO was found to contain water within the crystal structure. The average crystal density appears to be approximately 1.5 g/cm^3 , which is relatively low.

A selection of substituted pyridines were crystallised with NTO to form a selection of salts. All salts produced were 1:1 (NTO:Co-former), with the exception of Pip.NTO which was 2:1. A large range of interesting properties, both structural and physical, were observed in these salts. Firstly, moderate hydrogen bonding has been noted between NTO ions and co-formers, in addition to the presence of halogen bonding. These interactions along with π -stacking assemble the molecules into a variety of packing structures. Py.NTO has a wine-rack structure, which simultaneously

with expands in two directions while contracting in another with increasing temperature. Many NTO salts are layered, due to the planar nature of both molecules. It appears this arrangement and hydrogen-bonded network are linked to increased insensitivity to impact, relative to NTO. In some cases, insensitivity to impact has been greatly decreased, which is unusual. This indicates that incorporating non-energetic co-formers does not dilute the sensitivity properties of NTO.

Thermal stability is another physical property that can be significantly changed by the addition of certain co-formers. For Py.NTO and ClPy.NTO, it appears that the cationic component has evaporated prior to decomposition of NTO. In comparison, Pip.NTO and AP.NTO seem to decompose as an entity with NTO, with no prior endothermic processes. Furthermore, Pip.NTO exhibited an increase in thermal stability in comparison to NTO. This has been previously observed and reported in Mel.NTO [3].

The resulting densities of the NTO salts reside approximately halfway between the densities of each individual co-former. This is observed for all the NTO salts except for BrPy.NTO and ClPy.NTO, which present artificially increased densities, owing to the presence of the dense halogen atoms and halogen bonding. Moreover, no apparent trend has been observed between crystal density and detonation velocity of NTO salts.

Finally, an NTO salt was found with a pK_a difference as low as -0.85. Therefore NTO salts and co-crystals do appear to comply with the ΔpK_a range rule, established for pharmaceutical complexes. This is understandable, given the large difference in functionality and solubility of NTO (and co-formers) compared to common pharmaceutical compounds. In addition, it was possible to determine trends between pK_a difference and specific interaction distances. This is an active step toward understanding structure-property relationships for the design and control of energetic materials.

3.5 Suggestions for Further Work

The work carried out in this thesis has revealed promising areas of further research in structure-property design. A few of these areas worthy of further investigation are briefly summarised, as follows:

- Further property testing such as friction and spark on all salts, including substituted aniline co-former series. Can assign classification by regulations and standards. Therefore, identify if suitable for transportation.
- Complete trends – synthesise and characterise 3-fluoropyridine and 3-iodopyridine. Potentially amino-pyridines to increase nitrogen content - mainly a 2-aminopyridine to directly compare with 2-amino-3-picoline. Substitutes Piperazines, such as piperazine-2,6-dione. This would also increase oxygen balance. Also increase data points for comparison and establishing trends.
- Further investigation into variable temperature and pressure on salts. Full TGA/DSC. Potential to find polymorphs. Suggest looking further into Pip.NTO and halogen salts.

3.6 Reference

1. G. Smith, U. D. Wermuth, P. C. Healy, *Acta Cryst.*, 2005, **E61**, o746-o748
2. F. H. Herbststein, M. Kapon, G. M. Reisner, *Acta Cryst.*, 1985, **B41**, 348-354
3. T. V. Sreevidya, G. Golden, N. Saper, *Struct. Chem.*, 2011, **22**, 1105
4. T. Friscic, A. V. Trask, W. Jones, W. D. S. Motherwell, *Angew. Chem. Int. Ed.* 2006, **45**, 7546 –7550
5. G. Singh, I. P.S. Kapoor, S. M. Mannan, and S. K. Tiwari, *Journal of Energetic Materials*, 1998, **16**:1, 31-43
6. G. Singh, I. P.S. Kapoor, S. M. Mannan, and S. K. Tiwari, *Journal of Energetic Materials*, 1998, **16**:2-3, 101-118
7. M. Najafi and A. K. Samangani, *Propellants, Explosives, Pyrotechnics*, 2011, **36**: 487–492.

8. A. Coelho, TOPAS-Academic V4, Coelho Software, Brisbane, Australia. 2007
9. Oxford Diffraction, CrystAlisPro, (2006), Oxford Diffraction Ltd, Abingdon, Oxfordshire, England.
10. R.H. Blessing, *Acta Cryst.*, 1995. **A51**, 1-6
11. P. W. Betteridge, J. R. Carruthers, R. I. Cooper, K. Prout and D. J. Watkin, *J. Appl. Cryst.*, 2003, **36**, 1487.
12. G. M. Sheldrick, *Acta Cryst.*, 2015, **C71**, 3-8
13. C. D. Fuh, J. S. Lee and C. M. Liaw, *Journal of Data Science*, 2003, **1**, 83-101
14. M. Sućeska, *EXPLO5*, v. 6.03, (2015), Brodarski Institute, Zagreb, Croatia.
15. *BAM Fall Hammer (BFH-12) User Manual*
16. H. Czerski, *Churchill College, Cambridge, 2006*
17. M. W. Smith, M. D. Cliff, *NTO-Based Explosive Formulations*, DSTO Aeronautical and Maritime Research Laboratory, Australia, 1999
18. E. Klingsberg, *The Chemistry of Heterocyclic Compounds, Pyridine and Its Derivatives*, Interscience publishers, Inc., New York, 1960
19. W. L. F. Armarego, C. L. L. Chai, *Purification of Laboratory Chemicals*, Butterworth-Heinemann, Elsevier, Amsterdam, 2003

Chapter 4

Structural Studies of Co-crystals Formed by NTO with 4,4'-Bipyridine and 2-Pyridone

4.1 Introduction

To date there have been no reported co-crystals of NTO and the previous chapter illustrated that the ΔpK_a rule is correct. At values of ΔpK_a of -0.85, salt formation occurs, therefore when searching for a co-crystal the pK_a must be more negative and closer to -1. This reflects the known deficiencies of the ΔpK_a rule. In the previous chapter, there was some evidence that in the 3-ClPy.NTO salt, the proton was not entirely localised on the chloropyridine molecule. This suggested that a ΔpK_a of -0.85 for this system represented a potential threshold value below which a co-crystal might be formed. More data points around this ΔpK_a of -0.85 is required to confirm or deny this. Hence two candidate co-formers were selected on the basis that they would result in lower ΔpK_a values, thereby enabling the formation of co-crystals.

4.2 Aims

Previous work on NTO organic salts, such as pyridine.NTO motivated this chapter towards reproducing NTO co-crystals. The aims of this work were:

- To form co-crystal of 4,4'-bipyridine.NTO and 2-pyridone.NTO
- To provide evidence of co-crystal formation
- To compare crystal structure and physical properties to locate possible trends

4.3 Experimental

4.3.1 Materials

4,4'-Bipyridine and 2-hydroxypyridine were obtained from Sigma Aldrich. Single crystals of BiPy.NTO and PyO.NTO co-crystals were prepared by slow spontaneous crystallisation from solution at room temperature (1:1 molar ratios, ~10 mg of NTO

and co-former in a few mls of ethanol). Polycrystalline material of β -4,4'-bipyridine.NTO (β -BiPy.NTO) salt were formed from aqueous solutions of NTO.

4.3.2 Powder X-ray Diffraction

X-ray powder diffraction, performed using the D2 PHASER instrument, was utilised in initial screening of samples. Powder patterns were not of sufficient resolution to acquire full crystal structure data but they were used to compare powder patterns of sample with the starting materials. A polycrystalline sample of potential salts (~ 5 mg) was applied thinly to a disc and diffraction patterns recorded over the range of $2\theta = 5$ - 50° . Variable temperature powder X-ray diffraction studies on BiPy.NTO were conducted using synchrotron X-ray radiation, on beamline I11 at the Diamond Light Source, Rutherford Laboratory. The patterns were indexed using DASH [1] and TOPAS [2].

4.3.3 Single Crystal X-Ray Diffraction

Single crystal X-ray data for the NTO co-crystals were collected at 120 K, in the School of Chemistry, using an Agilent Technologies SuperNova diffractometer equipped with an Oxford cryosystems N₂ low temperature Cryostream. Data for BiPy.NTO and PyO.NTO were collected using monochromated Cu-K α radiation ($\lambda = 1.5418 \text{ \AA}$). Reflections were processed using CrysAlisPro [3] and an absorption correction applied based on the multi-scan method [4]. Within the CRYSTALS program suite [5], the structures were solved by direct methods with SHELXS and refined with anisotropic displacement parameters for all non-H atoms using SHELXS [6]. Hydrogen atoms were located using Fourier difference methods and refined isotropically.

4.3.4 DSC

DSC measurements were performed on a TA Instruments Q2000 over the temperature range 21 - 350°C at a scan rate of 10 K min⁻¹. The sample masses of α -BiPy.NTO and β -BiPy.NTO used were 1.4820 mg and 1.5550 mg respectively.

4.3.5 BAM Hammer

BAM hammer impact testing (BFH-12) was conducted at the Cavendish Laboratory, Cambridge on α -BiPy.NTO, β -BiPy.NTO, PyO.NTO and NTO. A sample of 40 mm³ was enclosed in an anvil device consisting of two coaxial steel cylinders. Anvil devices were disposed of along with sample after each test. A variety of loads were dropped from varying heights on all samples. The method conducted throughout is the 30-trial Bruceton method [7]. Anvil device one was initially used on all samples, later the file plate, device 2, set up was employed for NTO, α -BiPy.NTO and PyO.NTO. A positive result is commonly acknowledged by a flash of light or loud sound (bang), however here it was also distinguished by a discolouration or scorch marks.

4.3.6 VoD Calculations

All calculations on the detonation parameters of the materials were performed using the program package EXPLO5 V6.03 [8]. The detonation parameters were calculated at the C-J point with the aid of the steady-state detonation model using a modified Becker-Kistiakowski-Wilson equation of the state for modelling the system. The C-J point is found from the Hugoniot curve of the system by its first derivative. The main detonation products for the calculations of the energetic parameters were assumed with N₂, H₂O, and CO₂. The parameters inputted into the software for each salt and co-crystal are; the enthalpy of formation, chemical compositions, and experimentally determined crystal densities.

4.4 Results and Discussion

Two NTO co-crystals were discovered and characterised; 4,4'-bipyridine.NTO (BiPy.NTO) and 2-pyridone.NTO (PyO.NTO). The synthesis of the latter involves the crystallisation of 2-hydroxypyridine and NTO in a 1:1 ratio. The resulting NTO co-crystal contains 2-pyridone molecules rather than the tautomeric 2-hydroxypyridine (Figure 4.1). Single crystals of both co-crystals appeared to be cream in colour. This is an unusual observation for NTO complexes produced to date, for which the intense yellow colour NTO salts is attributed to the formation of the NTO⁻ anion.

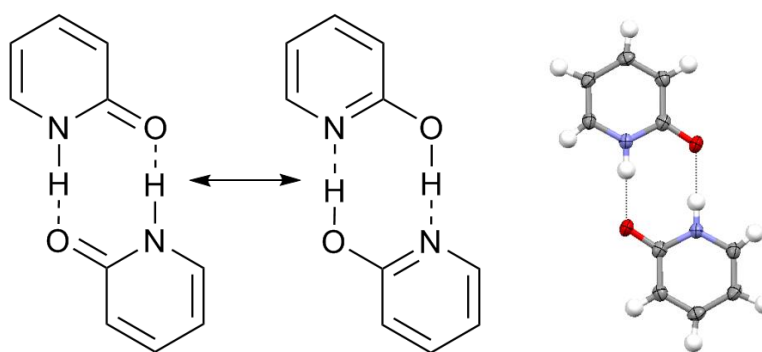


Fig 4.1 Tautomerisation of 2-pyridone to 2-hydroxypyridine

Crystal structures were obtained using single crystal X-ray diffraction and important parameters are shown in Table 4.1. It is worth noting that the densities of both co-crystal are lower than that of NTO (1.92 g/cm^3) [9, 10], and lie half-way between those of the co-formers. Error bars symbolise the exact half way value between co-formers (figure 4.2).

Table 4.1 Crystallographic information for BiPy.NTO and PyO.NTO

	BiPy.NTO	PyO.NTO
Formula	$\text{C}_{12}\text{H}_{10}\text{N}_6\text{O}_3$	$\text{C}_7\text{H}_7\text{N}_5\text{O}_4$
Mr [g.mol⁻¹]	286.25	225.16
Crystal System	Monoclinic	Monoclinic
Space Group	$P2_1/n$	$P2_1/c$
<i>a</i> (Å)	7.821 (2)	11.810 (9)
<i>b</i> (Å)	5.786 (1)	5.568 (5)
<i>c</i> (Å)	27.336 (5)	14.753 (2)
β (°)	92.192 (2)	104.086 (9)
<i>V</i> (Å³)	1236.07	940.99
ρ (g/cm³)	1.538	1.589
R-Factor (%)	3.38	6.95
Radiation	Cu	Mo
Z	4	4

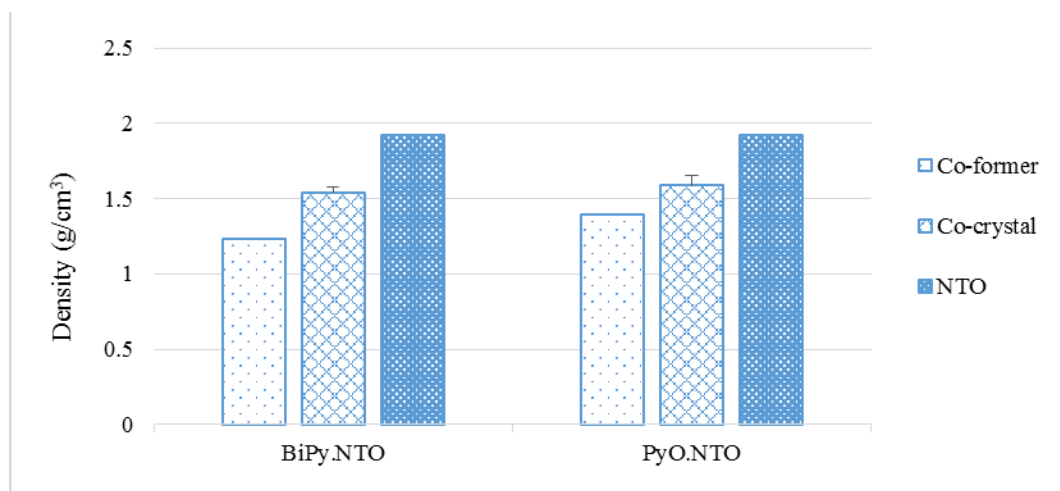


Fig 4.2 Crystal density of co-former (BiPy and PyO), the resultant salts (BiPy.NTO and PyO.NTO) and the crystal density of NTO.

4.4.1 Asymmetric Unit

Asymmetric units of both co-crystals are shown in Figure 4.3, and show that the hydrogen atoms remain on the NTO molecule rather than being transferred onto the co-former. Firstly the ΔpK_a of BiPy.NTO and PyO.NTO are -0.98 and -0.97, respectively, the lowest ΔpK_a achieved for an NTO complex, after the chloropyridine.NTO salt (ΔpK_a , -0.88). The observation that the material is not bright yellow is also consistent with the retention of the proton on the NTO molecule.

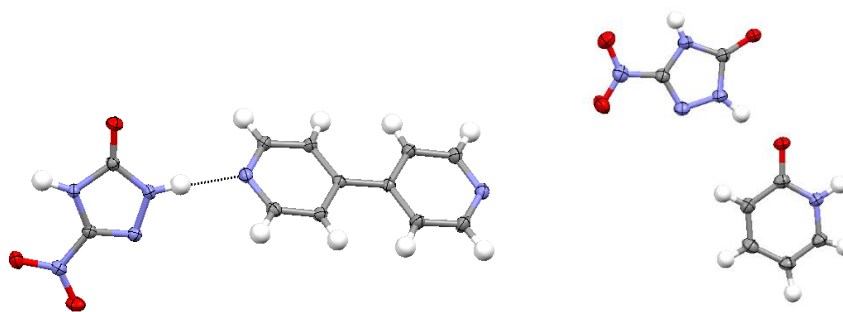


Fig 4.3 Asymmetric units of BiPy.NTO and PyO.NTO

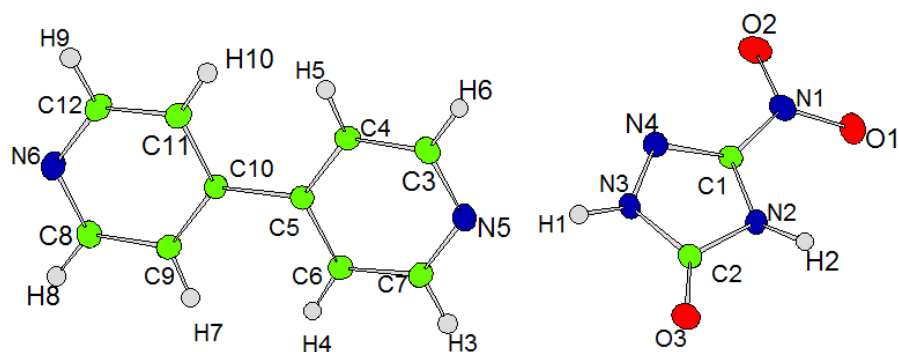


Fig 4.4 Labelled asymmetric unit of BiPy.NTO

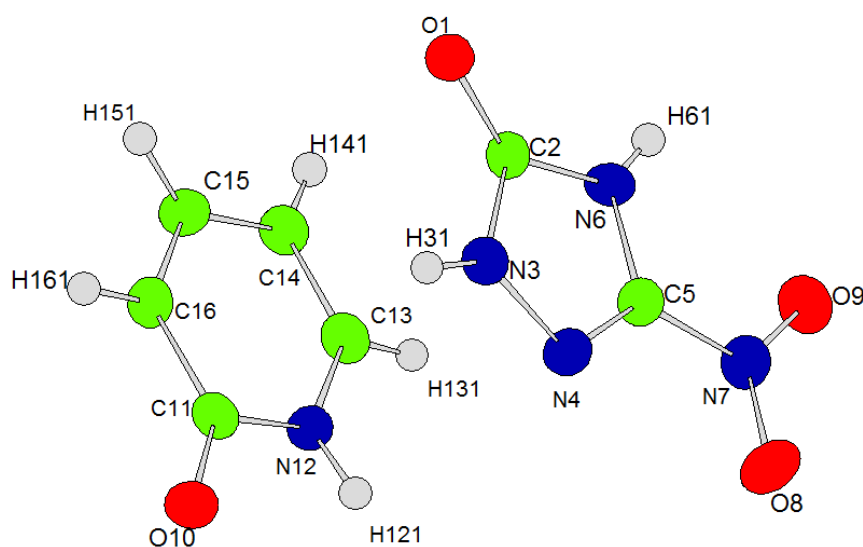


Fig 4.5 Labelled asymmetric unit of PyO.NTO

Crystallography can support this claim by focusing on the proton position. Hydrogen has only one electron, and so it is difficult to assign the atom through Fourier difference due to the lack of resulting electron density. Fortunately, BiPy.NTO and PyO.NTO do not contain any heavy atoms that could mask the electron density from a hydrogen atom. A Fourier difference map, with the hydrogen of interest removed, can be calculated using WinGx to visualise the electron density hole it leaves behind. Such images are shown in Figure 4.6 and 4.7 and confirm this conclusion.

Ultimately it would be helpful to conduct spectroscopic methods such as FT-IR and ATR-IR or methods such as solid-state NMR and neutron diffraction studies in

order to provide additional evidence and to explore the possible effects of temperature and pressure on the proton position.

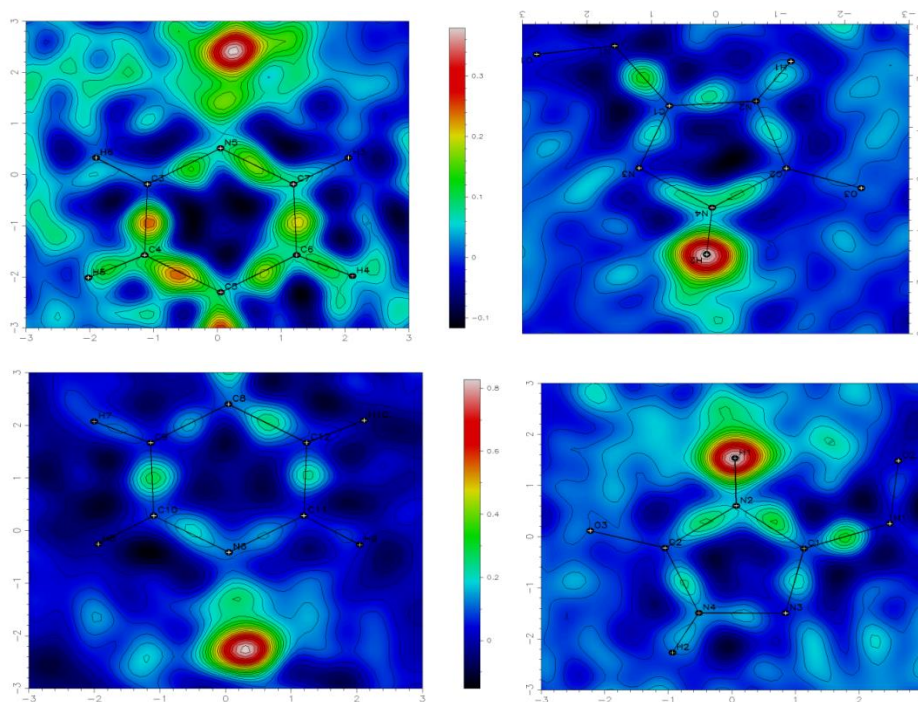


Fig 4.6 Fourier difference map of BiPy.NTO

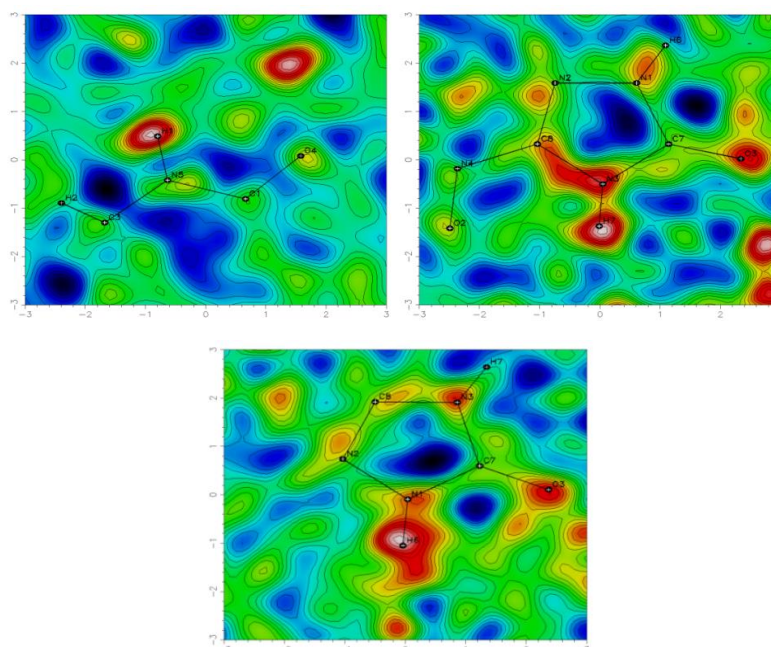


Fig 4.7 Fourier difference map of PyO.NTO

The structure of BiPy.NTO possesses several noteworthy features. Within the crystal structure of the BiPy.NTO co-crystal, molecules of 4,4'-bipyridine are more planar in comparison to 4,4'-bipyridine itself (Figure 4.8). This aids the formation of the layers observed in the patterns. It is a possibility that the planar character arises from a difference in H-bonding. Potentially the hydrogen bonding in the co-crystal is providing a slight charge on the BiPy molecule thereby affecting the torsion angle.

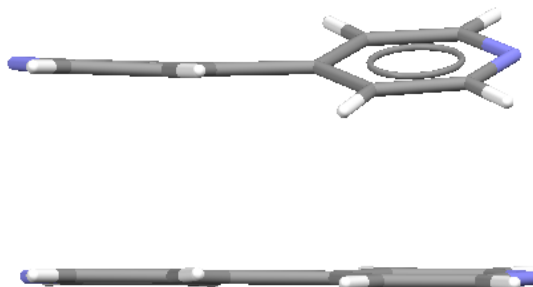


Fig 4.8 4,4'-Bipyridine molecule at 193 K and in co-crystal at 120 K, respectively.



Fig 4.9 NTO molecule at 100 K and NTO in co-crystal at 120 K.

4.4.2 Intermolecular Bonding and Structural Arrangements

BiPy.NTO possesses two H-bonds, $N-H \cdots N$, between BiPy and NTO molecules, shown in Figure 4.10, which form a 1D chain containing each molecule in an ABAB pattern. The hydrogen-bond which exists between the protonated and deprotonated nitrogen atoms in previously described NTO salts (Chapter 3), is also observed in BiPy.NTO, but not in PyO.NTO.

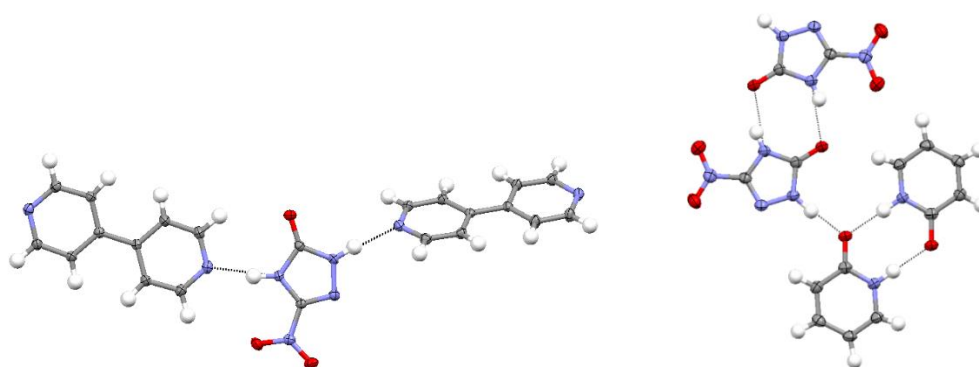


Fig 4.10 Hydrogen bonding between in BiPy.NTO and PyO.NTO, between co-former and NTO molecules

Stronger H-bonds exist within PyO.NTO (N-H \cdots O). However, the strongest hydrogen bonding is present between two PyO molecules which form a dimer, and two NTO molecules. A weak hydrogen bond of N12-H12 \cdots O10 exists between NTO and PyO. By way of these interactions a 1D ribbon of hydrogen bonded molecules extends through the crystal structure.

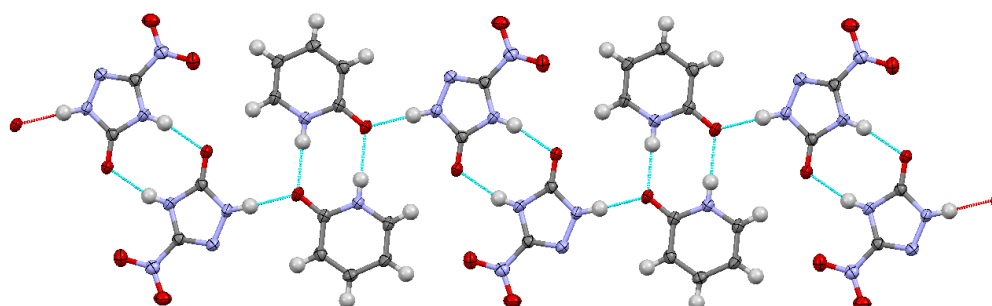


Fig 4.11 Hydrogen bonded ribbons of PyO and NTO molecules

Table 4.2 Hydrogen bonds lengths and angles between NTO and co-former

	<i>D-H\cdotsA</i>	<i>D-H</i> [\AA]	<i>H\cdotsA</i> [\AA]	<i>D\cdotsA</i> [\AA]	<i>D-H\cdotsA</i> [$^\circ$]
BiPy.NTO	N3-H1\cdotsN5	0.90 (2)	1.923 (3)	2.825 (2)	171.0 (2)
	N2-H2\cdotsN6	0.90 (2)	1.846 (2)	2.731 (1)	167.4 (2)
PyO.NTO	N6-H6\cdotsO1	0.84 (3)	1.901 (3)	2.721 (4)	165.8 (2)
	N3-H3\cdotsO10	0.87 (3)	1.826 (2)	2.697 (4)	176.4 (2)
	N12-H12\cdotsO10	0.86 (3)	1.952 (3)	2.814 (4)	177.8 (2)

The 2D and 1D chains of planar molecules within PyO.NTO and BiPy.NTO, give rise to a partially layered structures. Within BiPy.NTO the layers are spaced 2.787 Å apart. Viewing the structure along the *a*-axis, it is possible to see channels of NTO and BiPy.

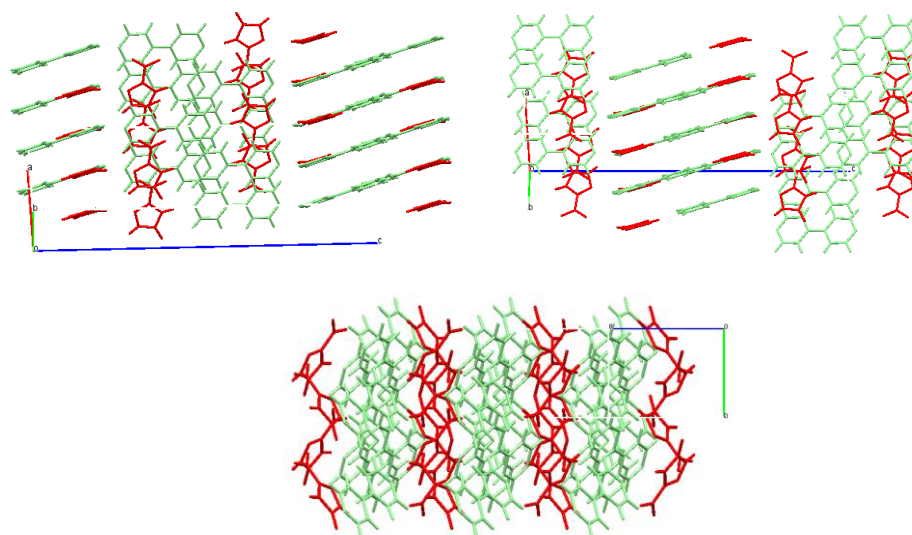


Fig 4.12 Structural packing arrangement in BiPy.NTO.

Similar to BiPy.NTO, networks of NTO and PyO are also seen in PyO.NTO along the *b*- and *c*-axis. The semi-layered structure is shown in Figure 4.12. The distances between the layers is 3.067 Å.

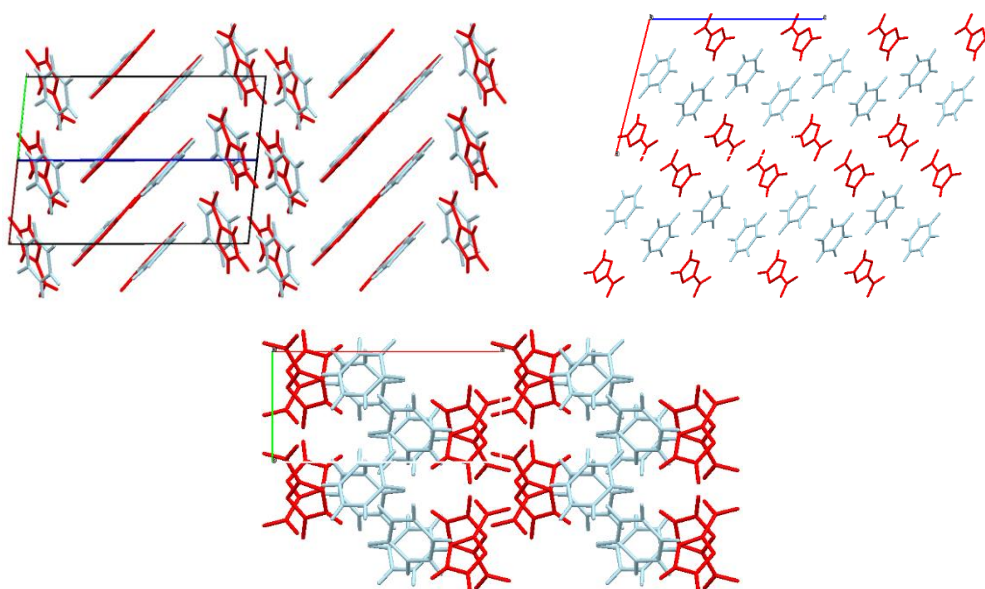


Fig 4.13 Structural packing arrangement in PyO.NTO.

4.4.5 Polymorph Investigation of BiPy.NTO

When crystallising samples of BiPy.NTO it was noticed that two different forms were obtained depending on crystallisation conditions. Typically NTO forms a yellow product when a salt is formed, but forms a paler, off-white product when a co-crystal is formed. The product obtained from ethanol was off-white and from water was yellow, thereby giving an initial indication that a co-crystal and salt had been formed respectively. This is further supported by the $\Delta pK_a \approx -0.98$ for BiPy.NTO in ethanol and $\Delta pK_a \approx 0.50$ for BiPy.NTO in water [11, 12]. When reflecting on previous chapter 3, salts exist as low as $\Delta pK_a = -0.8$. The β -form (salt) was indexed using data from high-resolution powder X-ray diffraction studies on beamline at the Diamond light source, I11 (shown in Table 4.3). To date it has been difficult to produce single crystals of the β -form that would be suitable for single crystal X-ray diffraction studies. A simple heating test was conducted on the BiPy.NTO salt and it was observed that the salt changes colour from yellow to white within 15 seconds of heating, as shown in Figure 4.14. Initially it was thought that the salt contained water or was a hydrate, yet FT-IR measurements showed that this was not the case. Therefore, it was assumed that these were indeed polymorphs with one being a salt and the other a co-crystal.

Table 4.3 Crystal structure information for BiPy.NTO polymorphs

Polymorph	Space group	Volume (\AA^3)	A (\AA)	B (\AA)	C (\AA)	α ($^\circ$)	β ($^\circ$)	γ ($^\circ$)
α -form	$P2_1/n$	1236	7.82	5.79	27.33	90	92.19	90
β -form	$P2_1$	1618	11.52	31.79	4.62	90	94.61	90

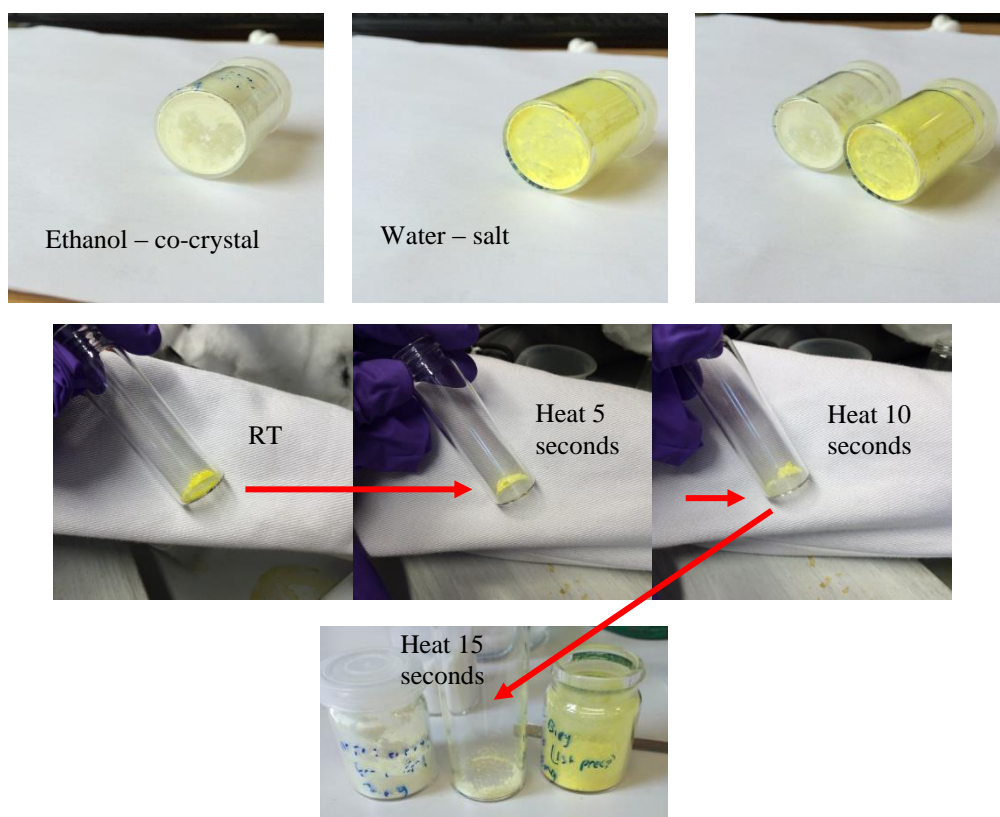


Fig 4.14 Polymorphs of BiPy.NTO, produced from ethanol and water. Heat is applied to β -BiPy.NTO salt, after 15 seconds colour change has occurred.

4.4.5.1 Variable Temperature Diffraction Studies - I11, Diamond

On gentle warming, β -BiPyNTO can be converted to α -BiPyNTO, as shown in Figure 4.15. Full conversion to the α -form (co-crystal) occurred at 60 °C (333 K). On cooling to room temperature α -BiPyNTO persisted. An increase in symmetry was observed based on systematic absences.

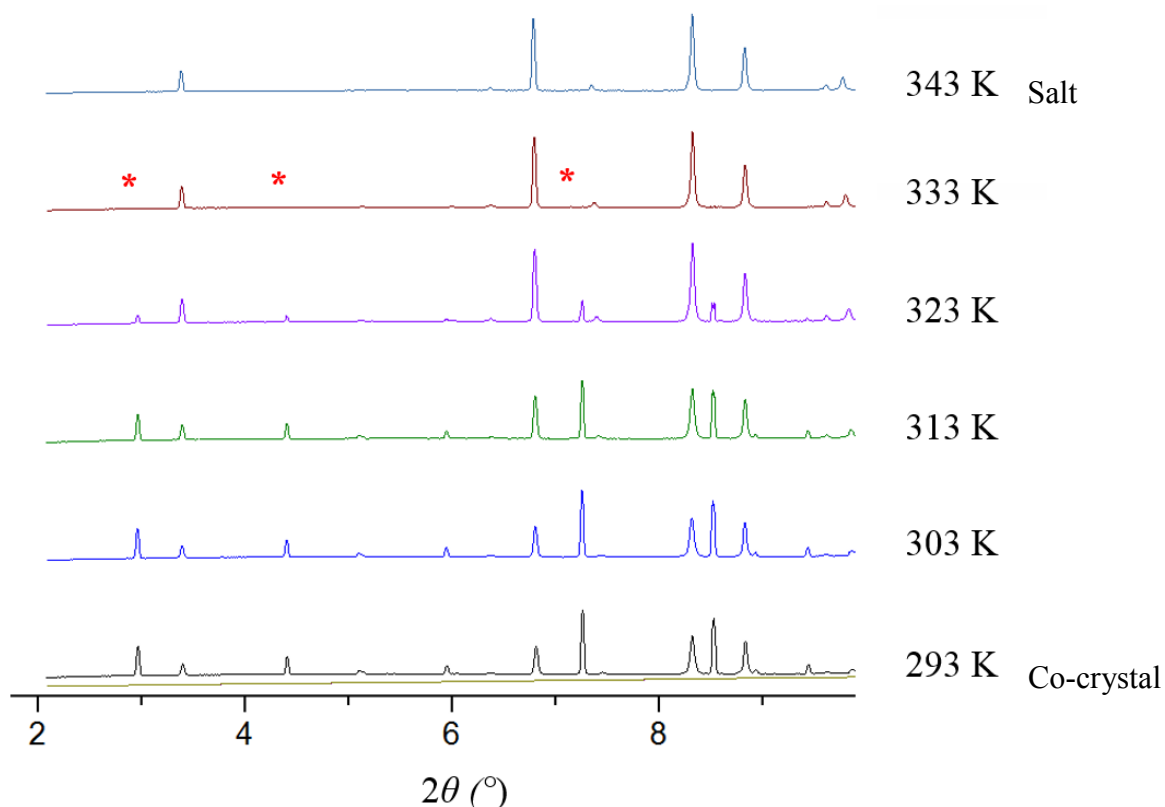


Fig 4.15 Variable temperature X-ray diffraction studies of BiPy.NTO

4.4.6 Properties

DSC measurements were conducted on both polymorphs of BiPy.NTO and the data compared to that of NTO. α -BiPy.NTO display a sharp exothermic peak, which starts at 216.4 °C, with a peak maximum at 217.5 °C (366.2 J/g). A sharp endothermic peak was also observed at 287.4 °C (41.7 J/g). This secondary peak is likely to be the melting of the decomposition products. β -BiPy.NTO has two slightly broad endothermic peaks, at 74.9 °C and 133.2 °C prior to a large sharp exothermic peak at 221.0 °C. The endothermic peaks indicate there is either a melt or polymorph change. It is likely that a phase change to α -BiPy.NTO is occurring, as this change was observed in variable temperature powder X-ray diffraction patterns at around 60 °C. The apparent difference in temperature may reflect the different heating rates in the two experiments. In addition the exothermic peak at 221.0 °C is very similar to the exothermic peak seen in α -BiPy.NTO at 217.5 °C.

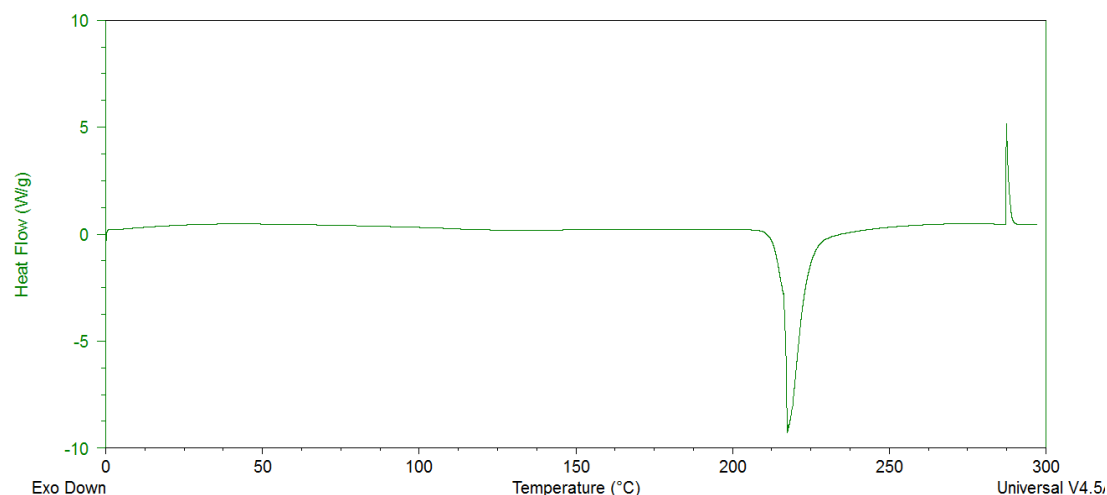


Fig 4.16 DSC plots of α -BiPy.NTO at a rate of 10 K.min⁻¹

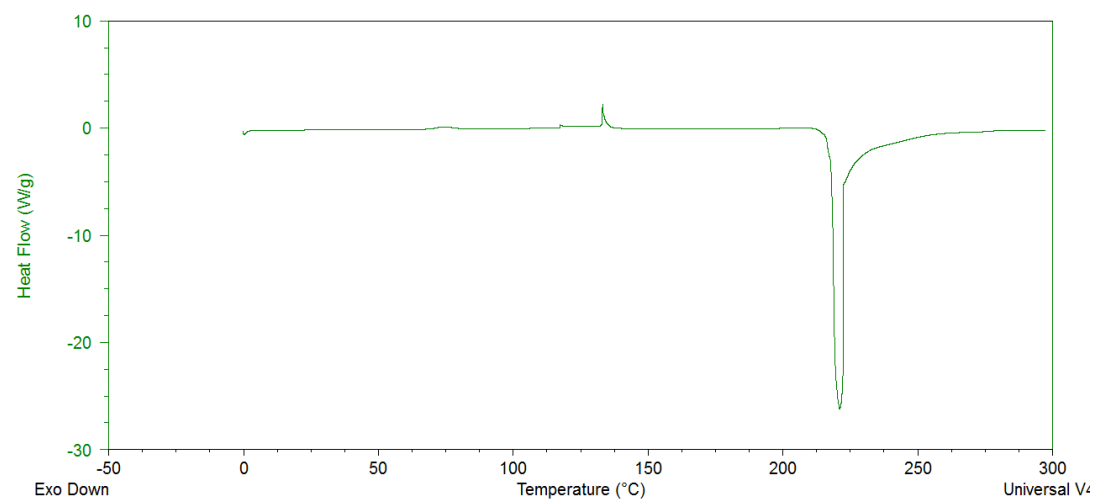


Fig 4.17 DSC plots of β -BiPy.NTO at a rate of 10 K.min⁻¹

Table 4.4 Physical properties of α -BiPy.NTO, β -BiPy.NTO and PyO.NTO

Co-crystal	Impact (J)	Density (g/cm ³)	VoD (m/s)	P (GPa)	DSC (°C)
α -BiPy.NTO	23.7 *	1.538	5970.0	10.39	217.5
β -BiPy.NTO	>100	-	-	-	221.0
PyO.NTO	>100	1.589	5598.5	9.38	-

* exhibits interesting two impact sensitive “zones”

Full impact sensitivity testing was conducted on PyO.NTO. Results indicate the co-crystal is as insensitive to impact as NTO – no initiation even at 100 J.

Both polymorphs of BiPy.NTO were scaled up and tested on a BFH-12 BAM hammer using a 30-trial Bruceton method. Similar to NTO, β -BiPy.NTO is insensitive to impact > 100 J. In vast contrast interesting impact property behaviour is exhibited in α -BiPy.NTO.

Upon initial testing of α -BiPy.NTO to find the limiting energy value, required for Bruceton method, unusual properties were observed. Testing was started at 40 J, resulting in no initiation, but a colour change to bright yellow was observed. The drop-height was gradually increased to produce 100 J of impact energy, with an assumption that the α -BiPy.NTO co-crystal was as insensitive to impact as β -BiPy.NTO. The colour change continued to appear until 70 J and resembled the salt β -BiPy.NTO. At 70 J the colour change was no longer observed, yet signs of initiation began to appear in the form of scorch marks on the sample. Between 70 and 100 J, scorch and soot marks indicated that initiation had occurred, yet no traces of yellow colour were observed. Out of curiosity a selection of tests were repeated between 40 J and 70 J, finishing with tests taken at values lower than 40 J. At around 30 J signs of initiation, scorch marks were witnessed, and continued to be seen down to 25 J. At values lower than 25 J no initiations were seen. This complex behaviour led to two tests (30-trial Bruceton method) at around 25 J and 70 J.

Table 4.5 Bruceton method testing on β BiPy.NTO with a 10 kg load. 50% point = 23.7 cm, s.d. = 1.212 cm

H (cm)	Individual Trial Results											$\sum n_x$	$\sum n_o$	i
18					O							0	1	0
20				O	O	O						0	3	1
22	O		O	X	X	O	O	O		O		2	6	2
25	X	O	X	X		X	X	O	O	X	X	7	1	3
28	X	X						O	X	X		4	0	4
32	X							X				2	0	5
36	X											1	0	6
Totals N_x and N_o											15	15		

Table 4.6 Bruceton method testing on β BiPy.NTO with a 10 kg load. 50% Point = 72 cm, s.d = 1.137 cm

H (cm)	Individual Trial Results											$\sum n_x$	$\sum n_o$	i
56		O										0	1	0
63		X	O	O	O	O				O		1	5	1
71	O	X	O	X	X	O	O	O		O	X	4	6	2
79	X	X	X			X	O	X	O	X	X	7	2	3
89	X						X		X			3	0	4
100	X											1	0	5
Totals N_x and N_o											14	16		

A possible interpretation of these results is that the pressure generated on impact, drives the sensitive co-crystal to convert to the less-sensitive salt. Higher impact energy also results in heat and so drives back to the co-crystal – as previously mentioned can convert from salt to co-crystal *via* heat. Therefore there could be a balance between pressure and temperature.

To further explore this concept, the co-crystal α -BiPy.NTO was placed in a manual hydraulic press, which can exert up to 15 tonnes load onto a sample. Intervals of 1 tonne of pressure was placed on the various samples of co-crystal to compare visually and powder X-ray diffraction. Colour change from cream to yellow occurred at low loads of 3-5 tonnes. This represents a pressure of ~200-300 bar. However, powder patterns are not conclusive as to what polymorph is present.

To analyse the energetic performance of NTO co-crystals, detonation parameters were calculated using EXPLO5 on α -BiPy.NTO and PyO. In comparison the NTO, detonation velocity (V_{oD}) is much lower for both co-crystals at 5970.0 and 5598.5 m/s (Table 4.4). These values are similar to those of other NTO complexes involving pyridine based co-formers (Chapter 3). BiPy.NTO appears to have a higher detonation velocity value in comparison to PyO.NTO, even though PyO.NTO has a higher density (Table 4.4). This information is plotted in a graph for comparison and to assess any trends. Data collected for NTO salts, described in chapter 3 are also

included. There are not enough data points for NTO co-crystals to draw any conclusions. However, it appears that values for the co-crystals are in accordance with results collected for NTO salts.

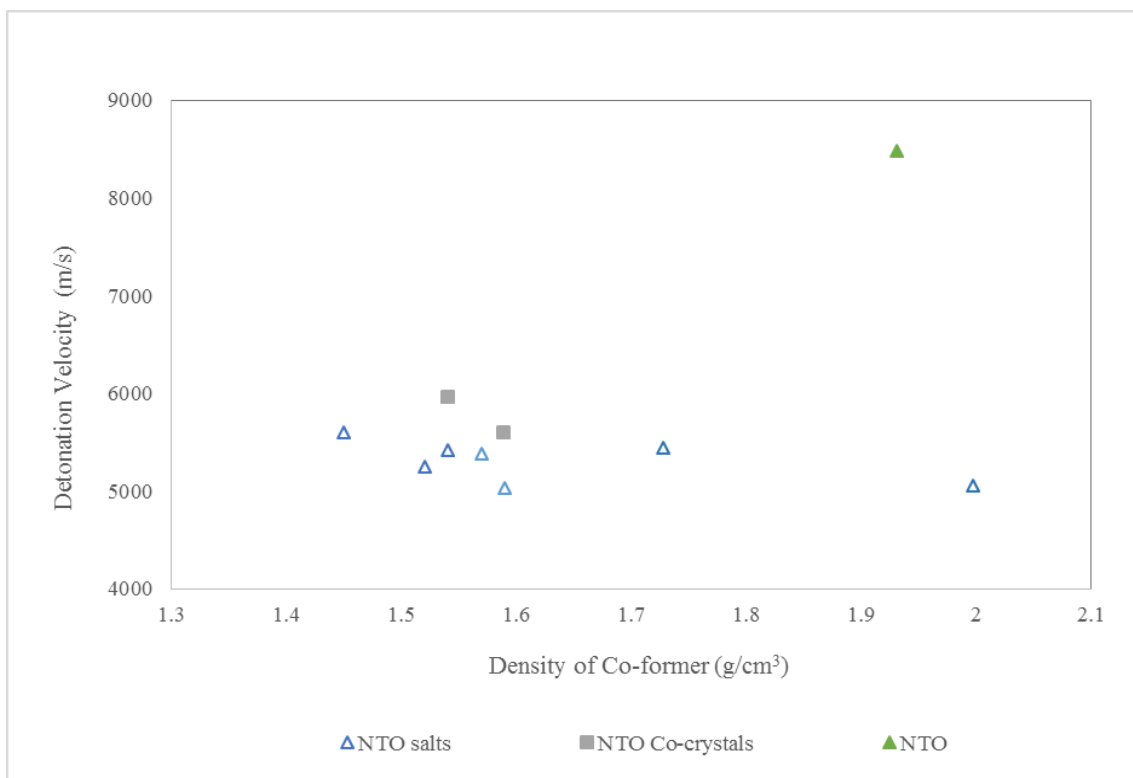


Fig 4.18 Plot of crystal density against detonation velocity for NTO salts. Co-former types are set into categories.

4.5 Conclusions

The first NTO co-crystals have been prepared and characterised using single-crystal X-ray diffraction. The crystal structure density and detonation velocities of both co-crystals are lower than those of NTO. An interesting feature observed is the semi-layered structure present in both co-crystals, which may be responsible for their low impact sensitivities.

BiPy.NTO has two polymorphs that can be produced in different solvents, which appear to be a salt and co-crystal. It is possible to convert from the β -form (salt) to the α -form (co-crystal) by heating. In addition it appears the conversion from α -form the β -form can potentially occur through minimal pressure. This conversion prevents initiation between 40 and 70 J of impact energy. It is possible that impact

testing is producing enough heat output to convert material back to the more impact sensitive form. DSC measurements of both polymorphs suggest that the salt (β -form) converts to co-crystal at around 79 °C, a similar value to variable temperature X-ray powder diffraction studies (60 °C).

4.6 Suggestions for Further Work

Future work will include designing experiments to specifically target co-crystal formation over salt formation. High-pressure studies should be conducted on both α - and β -form of BiPy.NTO, to investigate additional polymorphism and equation of state. Further structural characterisation will also need to be completed for β -BiPy.NTO, to analyse key structural features such as proton position and crystal density. Once the density of the β -form has been established, detonation parameters can be calculated using the EXPLO5 program. DSC measurements of PyO.NTO with the addition of TGA is required to compare with other NTO co-crystals and salts. Additionally full sensitivity testing, such as friction and spark testing, will need to be carried out on all co-crystals comparing them directly with standard NTO.

4.7 References

1. W. I. F. David, K. Shankland, J. van de Streek, E. Pidcock, W. D. S. Motherwell and J. C. Cole, *J. Appl. Cryst.*, 2006, **39**, 910-915
2. A. Coelho, TOPAS-Academic V4, Coelho Software, Brisbane, Australia. 2007
3. Oxford Diffraction, CrystAlisPro, (2006), Oxford Diffraction Ltd, Abingdon, Oxfordshire, England.
4. R.H. Blessing, *Acta Cryst.*, 1995. **A51**, 1-6
5. P. W. Betteridge, J. R. Carruthers, R. I. Cooper, K. Prout and D. J. Watkin, *J. Appl. Cryst.*, 2003, **36**, 1487.
6. G. M. Sheldrick, *Acta Cryst.*, 2015, **C71**, 3-8

7. C. D. Fuh, J. S. Lee and C. M. Liaw, *Journal of Data Science*, 2003, **1**, 83-101
8. M. Sućeska, *EXPLO5*, v. 6.03, (2015), Brodarski Institute, Zagreb, Croatia.
9. N. B. Bolotina, K. Kirschbaum, A. A. Pinkerton, *Acta Crystallogr.*, 2005, **B61**, 577
10. M. W. Smith, M. D. Cliff, *NTO-Based Explosive Formulations*, DSTO Aeronautical and Maritime Research Laboratory, Australia, 1999
11. J. Ulstrup, *Acta Chem. Scand.*, 1971, **25**, 3397
12. J. A. Dean, *Lange's Handbook of Chemistry*, McGraw-Hill, Inc, New York, 1999

Chapter 5

Structural Studies of Salts Formed Between NTO and 3,5-Diamino-1,2,4-triazole and 3,4-Diamino-1,2,4-triazole

5.1. Introduction

The majority of organic NTO salts described so far contain 6 membered heterocycles as co-formers, with only a few containing 1,2,4-triazole derivatives. Triazoles are potentially desirable co-formers on account of their high nitrogen content, thereby producing more energy and gas upon decomposition. Examples of NTO salts with 1,2,4-triazoles are 3-amino-1,2,4-triazole.NTO (3-ATz.NTO) [1,2], a layered structure with 2D hydrogen-bonding sheets, and 4-amino-1,2,4-triazole.NTO (4-ATz.NTO) [3]. Physicochemical properties have been reported for both 3-ATz.NTO and 4-ATz.NTO and are shown in Table 5.1, but there is no crystal structure data reported for 4-ATz.NTO. The most recent report involving a triazole.NTO salt is the salt 3,4-diamino-1,2,4-triazole.NTO (3,4-DAT.NTO), which was described in 2013 by Zhang *et al.*, has full structural and physicochemical properties. For example, 3,4-DAT.NTO is described to be relatively sensitive to impact (3.18 J) [4].

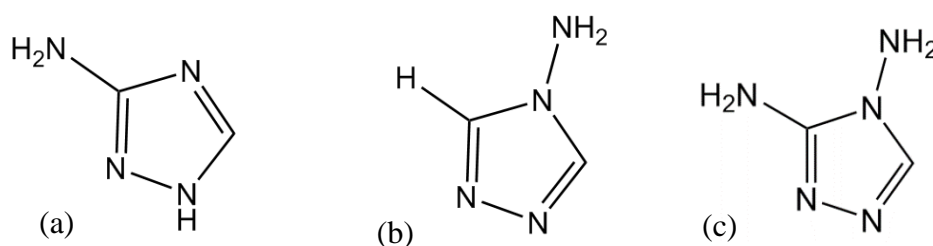


Fig 5.1 *a* The molecular structure of 3-aminotriazole (3-ATz) presented alongside *b* 4-aminotriazole (4-Atz) and *c* 3,4-diaminotriazole (3,4-DAT)

Unlike the salts described in chapter 3, the -NH_2 groups external to the ring in 3-ATz.NTO, 4-ATz.NTO and 3,4-DAT.NTO (Fig. 5.1) are not protonated, but instead one of the nitrogen atoms within the heterocyclic ring becomes protonated.

Table 5.1 Physicochemical Properties of 3-ATz.NTO, 4-ATz.NTO and 3,4-DAT.NTO.

	<i>wt N (%)</i>	<i>OB (%)</i>	<i>T_d (°C)</i>	<i>ρ (g/cm³)</i>	<i>VoD (m/s)</i>
3-ATz.NTO [1, 2]	52.33	- 60	255	1.72	8842
4-ATz.NTO [3]	52.33	- 60	175	1.68*	8016
3,4-DAT.NTO [4]	55.01	- 59	237	1.69	6320

* obtained via gas pycnometer.

The interesting properties of 3-ATz.NTO, 4-ATz.NTO and 3,4-DAT.NTO provided the motivation to explore salts of NTO with 5-membered heterocycles. In particular, the intention was to prepare a salt or co-crystal of NTO with 3,5-diamino-1,2,4-triazole (3,5-DAT) and investigate its crystal structure and physicochemical properties in order to make comparisons with those of NTO. A further aim was to reproduce 3,4-DAT.NTO for comparison (physical and chemical properties) with 3,5-DAT.NTO with a particular focus on whether the crystal structure played a part in affecting properties.

5.2. Experimental

5.2.1. Materials

Crystalline samples of 3,4-DAT were synthesised from diamino guanidium chloride. [4] Diamino guanidium chloride was treated with formic acid in concentrated hydrochloric acid (as a catalytic agent) under reflux. Aqueous potassium hydroxide was used to neutralise 3,4-diamino-1,2,4-triazolium chloride to form 3,4-diamino-1,2,4-triazole. 3,5-Diamino-1,2,4-triazole was obtained from Sigma Aldrich.

Single crystals of 3,5-DAT.NTO and 3,4-DAT.NTO were prepared by slow, spontaneous crystallisation from aqueous solution at room temperature (1:1 molar ratios, 13 mg of NTO and 10 mg of 3,5-DAT.NTO in a few mls of solvent). Both polymorphs (α - and β -form) of 3,4-DAT.NTO were obtained from aqueous solution. Polycrystalline samples of both 3,5-DAT.NTO and 3,4-DAT.NTO were obtained from supersaturated solutions which were cooled rapidly. Samples were recrystallised from small volumes of hot water and methanol, respectively, in order to purify samples.

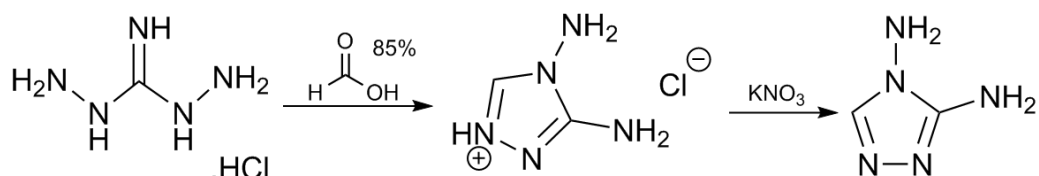


Figure 5.2 Reaction scheme of the synthesis of 3,4-diamino-1,2,4-triazole

5.2.2. Single Crystal X-Ray Diffraction

Single crystal X-ray data for 3,4-DAT.NTO and 3,5-DAT.NTO complexes were collected at 120 K, by Dr G. Nichol at the School of Chemistry, using an Agilent Technologies SuperNova diffractometer equipped with an Oxford cryosystems N₂ low-temperature Cryostream. Data for 3,5-DAT.NTO were collected using monochromated Cu-K α radiation ($\lambda = 1.5418 \text{ \AA}$). Reflections were processed using CrysAlisPro [5] and an absorption correction applied based on the multi-scan method [6]. Within the CRYSTALS [7] program suite, the structures were solved by direct methods with SHELXS and refined with anisotropic displacement parameters for all non-H atoms using SHELXS. Hydrogen atoms were located using Fourier difference methods and refined isotropically. In the cases of calculating Fourier difference maps WinGX [8] program suite was used.

5.2.3. Environmental Scanning Electron Microscopy (ESEM)

To determine the particle size and morphology of a crystalline material, electron scanning microscopy (ESEM) can be used. In order to obtain clear images of organic materials using conventional SEM, prior preparation of specimens is required, this process is time consuming and can be expensive. Environmental scanning electron microscopy (ESEM) was developed for uncoated or hydrated specimens to remove this problem. ESEM images were obtained by Dr. Jon J. Rickard from the University of Cambridge using the ESEM service at the Cavendish Laboratory. Small amounts of material were placed on a flat plate (shown in Fig. 5.3). Images were recorded at varying magnifications.

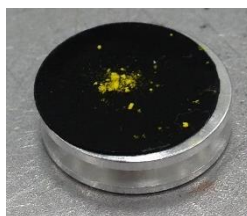


Fig 5.3 Polycrystalline 3,5-DAT.NTO on flat plate prior to ESEM testing.

5.2.4. DSC

DSC measurements were performed on a TA Instruments Q2000 over the temperature range 21 - 350°C at a scan rate of 10 K min⁻¹. The sample masses of α -3,4-DAT.NTO, 3,5-DAT.NTO and NTO used were 0.2250, 3.3430 and 3.1800 mg respectively.

5.2.5. BAM Hammer

BAM hammer impact testing (BFH-12) was conducted, at the Cavendish Laboratory, Cambridge, on 3,5-DAT.NTO, α -3,4-DAT.NTO and NTO. A consistent sample volume of 40 mm³ was applied per test and anvil devices were disposed of along with sample after each test. Throughout all testing on 3,5-DAT.NTO and NTO a weight of 10 kg was used at varying heights. For 3,4-DAT.NTO a weight of 5 kg was employed. The method conducted on 3,5-DAT.NTO and NTO is the 30-trial Bruceton method [9], whilst the 1-in-6 method was utilised for α -3,4-DAT.NTO. Device 1 was initially used for all samples, but later the file-plate device 2, was employed for NTO and 3,5-DAT.NTO. A positive result is commonly acknowledged by a flash of light or loud sound (bang). However, here it was also distinguished by a discolouration or scorch marks.

5.2.6. Calculation of Detonation Velocity

All calculations on the detonation parameters of the materials were performed using the program EXPLO5 V6.03 [10]. The detonation parameters were calculated at the C-J point with the aid of the steady-state detonation model using a modified Becker-Kistiakowski-Wilson equation of the state for modelling the system. The C-J point is found from the Hugoniot curve of the system by its first derivative. The main detonation products for the calculations of the energetic parameters were assumed with N₂, H₂O, and CO₂. The parameters inputted into the software for each salt and co-

crystal are; the enthalpy of formation, chemical compositions, and experimentally determined crystal densities. These values for each sample are detailed within the relevant sections.

5.3 Results and Discussion

5.3.1 Salt of NTO and 3,5-Diamino-1,2,4-triazole

3,5-Diamino-1,2,4-triazole, (or guanazole), is an alkaline material (pK_a of conjugate acid = 4.43 [11]) which is readily available. Recently, inorganic salts of 3,5-diamino-1,2,4-triazole with inorganic acids have been prepared and investigated for crystal engineering purposes. [12]

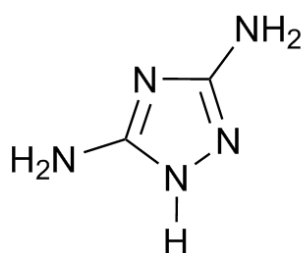


Fig 5.4 The molecular structure of 3,5-diaminotriazole (3,5-DAT)

3,5-DAT was chosen as a co-former for crystallisation with NTO on the basis of its composition and its functionality for crystal engineering. The pK_a difference between NTO and 3,5-DAT is 0.76. Using knowledge gained from previous work (Chapter 3) it was predicted that a salt would form rather than a co-crystal, with the proton being transferred onto one of the tertiary amine rather than the primary amines. 3,5-DAT has ideal hydrogen bond acceptors and donors for interacting with NTO. One additional significant feature of 3,5-DAT is the similarity in molecular shape to NTO.

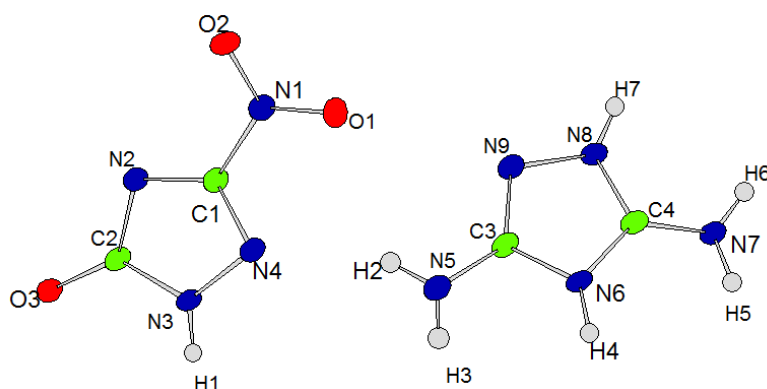


Fig 5.6 Labelled asymmetric unit of 3,5-DAT.NTO

5.3.1.1 Structural Properties of 3,5-Diamino-1,2,4-triazole.NTO

Large crystals were formed on slow evaporation of a 1:1 aqueous mixture of NTO and 3,5-DAT. The crystals appeared canary yellow and were prism-shaped, in marked contrast to the colourless, plate-shaped crystals of both NTO and 3,5-DAT. The powder X-ray diffraction pattern of the finely ground yellow polycrystalline material displayed new peaks when compared to the X-ray diffraction patterns of NTO and 3,5-DAT.

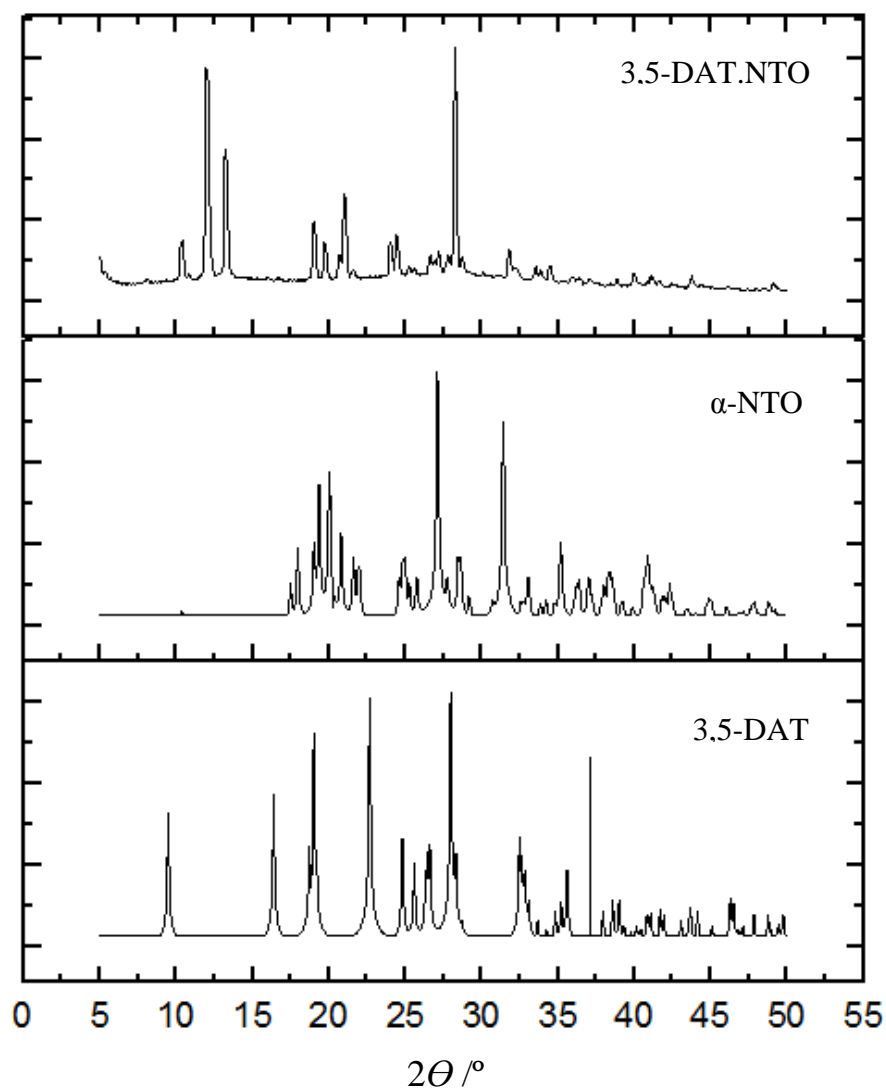


Fig 5.5 Powder X-ray diffraction patterns of polycrystalline sample of 3,5-DAT.NTO, α -NTO and 3,5-DAT.

The PXRD patterns shown in Fig 5.5 from the lightly ground sample showed that the polycrystalline material was not starting material (NTO or 3,5-DAT). In addition it appears that the sample was pure with no starting material present.

The 1:1 salt of NTO and 3,5-diamino-1,2,4-triazole (DAT) crystallises in the $P2_1/c$ space group with one deprotonated nitrotriazolone (NTO⁻) and one protonated 3,5-diamino-1,2,4-triazole (DAT⁺) molecule in the asymmetric unit. It was predicted that 3,5-DAT.NTO would be a salt of NTO rather than a co-crystal, based on ΔpK_a values and trends formed in Chapter 3; the charged species and proton transfer confirms the presence of a salt.

Table 5.2 Crystallographic information for 3,5-DAT.NTO

	3,5-DAT.NTO
Empirical formula	C ₄ H ₇ N ₉ O ₃
Formula mass /g.mol⁻¹	229.17
Temperature /K	120
Crystal Size /mm	0.12 x 0.03 x 0.02
Crystal System	Monoclinic
Space Group	$P2_1/c$
Z	4
a /Å	3.5501 (2)
b /Å	17.2271 (8)
c /Å	14.6537 (5)
β /°	93.903 (4)
Cell Volume /Å³	894.13 (3)
Density calculated / g.cm⁻³	1.702
Absorption coefficient /mm⁻¹	1.267
F(000) / Å	472
Final R₁ and wR₂ [I > 2σ(I)]	0.0437 0.0378
Largest diff. peak and hole /e.Å⁻³	0.33, -0.32

Using the crystal data obtained from single crystal X-ray diffraction studies, a simulated powder pattern was generated using Mercury [13]. A comparison of the simulated pattern and experimentally obtained pattern is shown in Figure 5.6. It is apparent that the bulk polycrystalline material is indeed a pure sample of 3,5-DAT.NTO. A significant difference between the patterns arises from some of the peak intensities, indicating some degree of preferred orientation, but this is not unexpected given the morphology of the crystallites and packing arrangement (see later) in the crystal structure.

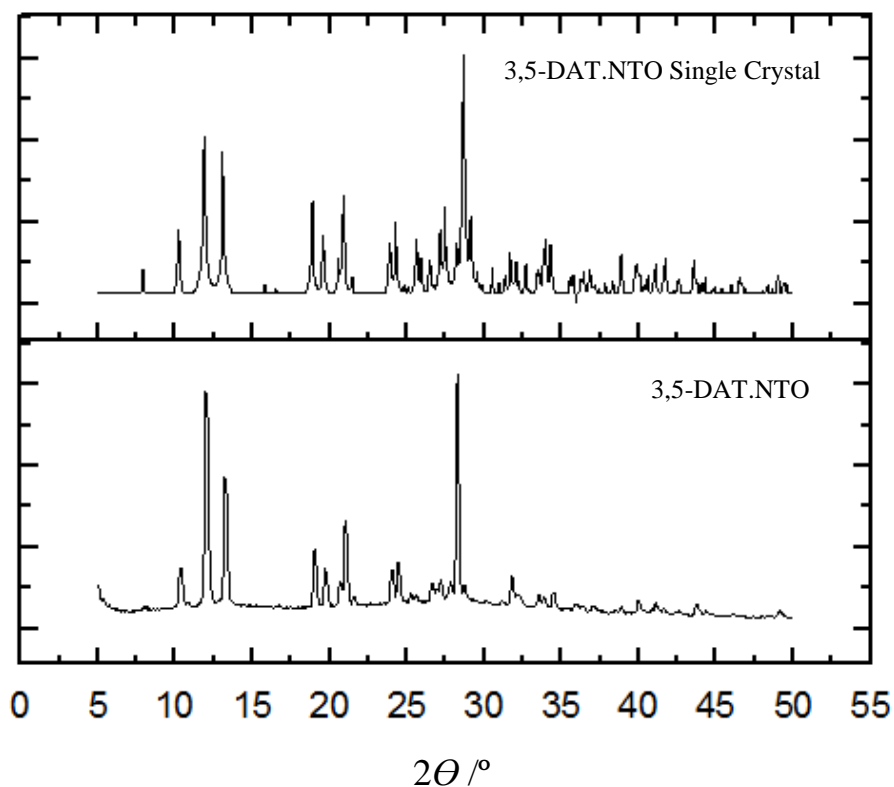


Fig 5.7 Simulated powder patter of 3,5-DAT.NTO collected via single crystal X-ray diffraction, powder X-ray diffraction pattern of polycrystalline sample

Two strong hydrogen bonds are present between the anion and cation forming a hetero-dimer (Fig 5.8). An N-H \cdots N bond is formed between the deprotonated nitrogen atom (N2) on the NTO $^-$ anion and the protonated nitrogen atom (N6) on the 3,5-DAT $^+$ cation.

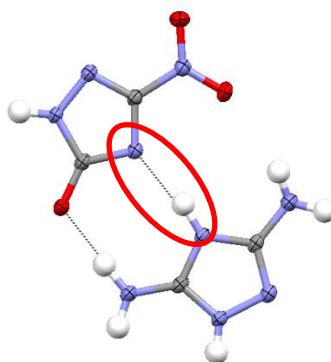


Fig 5.8 Hydrogen bond N2-H4...N6 (circled in red) involving NTO⁻ and 3,5-DAT⁺

Based on the N...N distance of 2.756 (2) Å and an N-H...N bond angle of 168° this can be regarded as a relatively strong hydrogen bond. This H-bond also represents the pathway for the proton transfer. From the Fourier-difference maps (Fig 5.9), the electron density resides closer to N6 on the 3,5-DAT⁺ ion rather than on N2 of the NTO⁻ anion. This is confirmation that the proton H4 was assigned to the correct position during refinement. A second hydrogen bond, N-H...O, is slightly longer at 2.787 Å, but with an N-H...O angle of 176°.

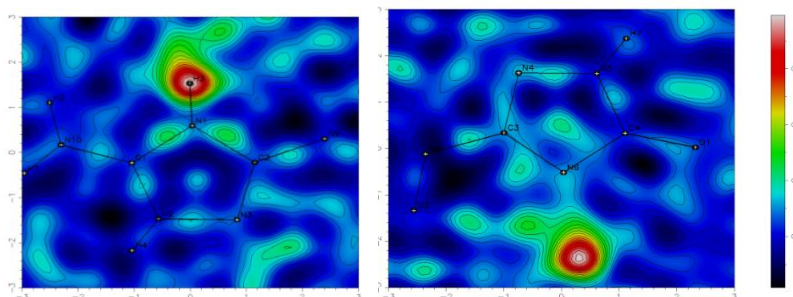


Fig 5.9 Electron density Fourier difference maps NTO⁻ and DAT⁺

Table 5.3 Hydrogen bonding lengths and angles within dimer and chain of NTO⁻ with 3,5-DAT⁺

<i>D-H...A</i>	<i>D-H</i> [Å]	<i>H...A</i> [Å]	<i>D...A</i> [Å]	<i>D-H...A</i> [°]
<i>Dimer</i>				
N6-H4...N2	0.942(2)	1.8261(1)	2.7559(1)	168.5(1)
N7-H5...O3	0.969(2)	1.8171(1)	2.7851(1)	176.1(1)
N5-H3...O2	0.870(2)	2.4431(1)	3.2572(2)	156.1(1)
<i>Chain</i>				
N8-H7...N9	0.848(2)	2.2133(1)	2.8673(1)	133.8(1)
N3-H1...O3	0.925(2)	1.8270(1)	2.7394(1)	168.2(1)

The packing of the heterodimers (AB) can be described in two directions; planar repeating chains that form 2D sheets along the *b*-axis and layered π -stacking in the perpendicular direction to the *b*-axis. The planar chains are formed of BA-AB-BA repeating units - this is illustrated in Figure 5.9.

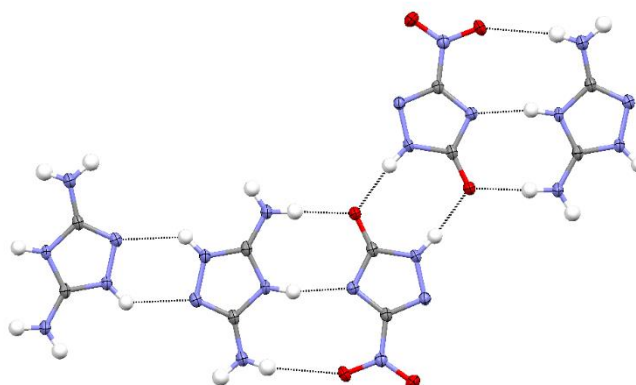


Fig 5.10 1-Dimensional chains of NTO⁻ and 3,5-DAT⁺ connected via hydrogen bonding

Based on the distance and angle of the hydrogen bonds linking 3,5-DAT cations, these H-bonds are much weaker and much less directional [2.8673(1) Å, 133.8(1)°] than in the hetero-dimer and NTO⁻-NTO⁻ homo-dimer [2.7394(1) Å, 168.2(1)°]. The chains are connected together through van der Waals interactions to form 2D sheets. The electrostatic interactions responsible are N-O...N and N-H...O, shown in the

asymmetric unit and connecting chains in Figure 5.11. A slight zig-zag within the hydrogen bonded chains is shown in different colours.

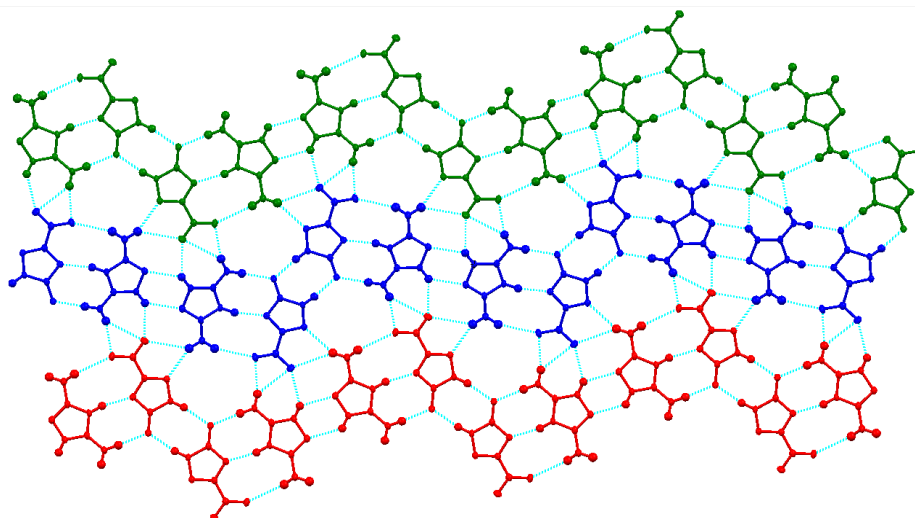


Fig 5.11 Chains connected by N-O...N and N-H...O interactions to form sheets

The 2D sheets containing the hetero-dimers stack through π - π interactions to form a layered structure. The distance between layers is 3.133(2) Å. The view directly perpendicular to *b*-axis, shows that a nitrogen atom of NTO⁻ sits directly above the heterocyclic ring of an adjacent NTO⁻ ion (Figure 5.12).

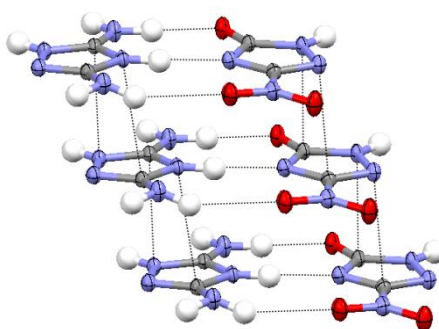


Fig 5.12 π -Stacking between the hetero-dimer, NTO⁻ and 3,5-DAT⁺

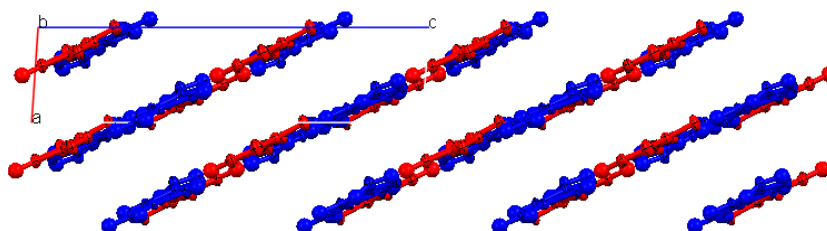


Fig 5.13 Packing arrangement of 3,5-DAT.NTO along the *b*-axis

The crystal structure density is 1.702 g/cm^3 at 120 K. It is worth noting that the resulting density of the NTO salt lies halfway between the densities of each of the co-formers as shown in Figure 5.14.

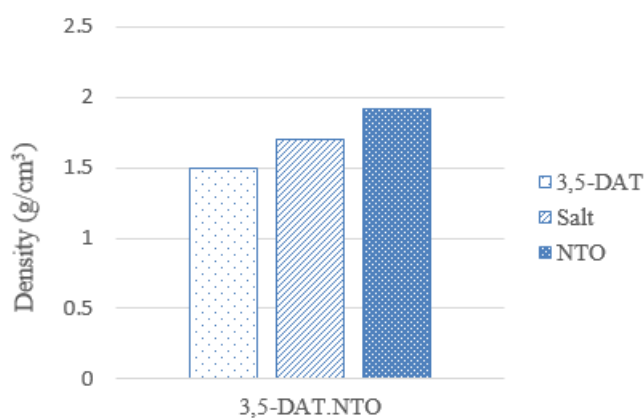


Fig 5.14 Crystal density of starting materials, 3,5-DAT and α -NTO taken at room temperature, and salt 3,5-DAT.NTO taken at 120 K. [14, 15]

5.3.1.2 Physical Properties of 3,5-Diamino-1,2,4-triazole.NTO

To assess the energetic and physical properties of 3,5-DAT.NTO the morphology (ESEM), thermal stability (DSC) and sensitivity to impact were experimentally determined. In addition, the heat of formation was calculated, (from the lattice enthalpy and heat of formation of cation and anion) in order to determine the detonation parameters using the EXPLO5 program.

Environmental scanning electron microscopy

The ESEM images highlight the plate-like morphology of NTO. In contrast, 3,5-DAT.NTO adopts a prismatic morphology, and under high magnification the layered nature of the structure can be discerned.

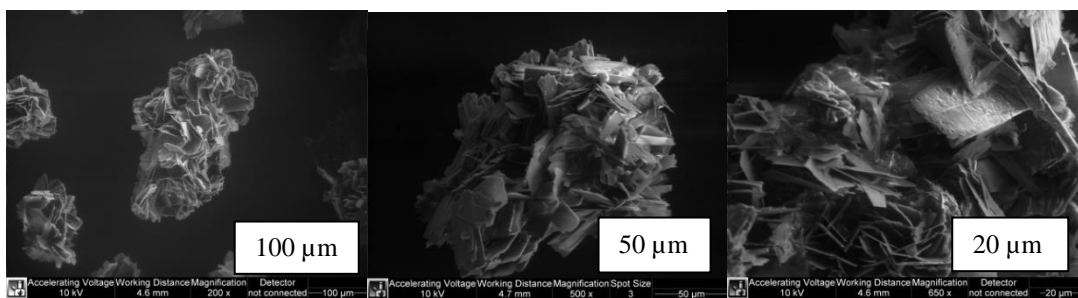


Fig 5.15: ESEM images of NTO at varying magnification. Observations include the plate-like morphology of the crystals.

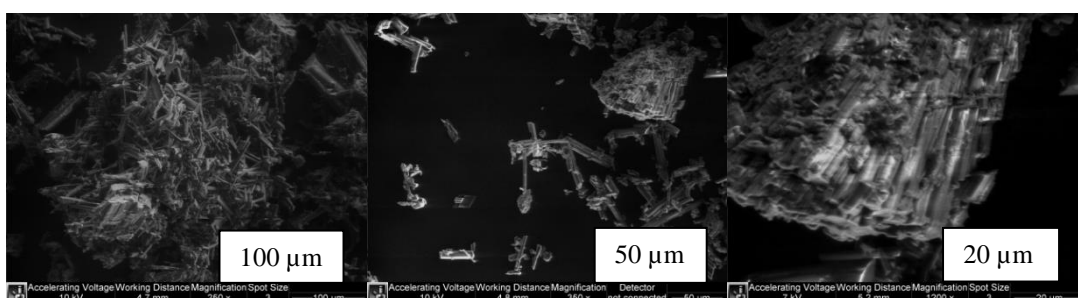


Fig 5.16: ESEM images of 3,5-DAT.NTO at varying magnification. Crystals are observed to be small and cluster together.

Differential scanning calorimetry

The thermal behaviour of 3,5-DAT.NTO was analysed by DSC with a linear heating rate of 10 K min^{-1} . The plot is shown in Figure 5.17 and shows an exothermic process that began at 205.4°C with a maximum at 247.1°C . The appearance of this peak is at a temperature not much lower than that for NTO ($253\text{-}279^\circ\text{C}$) [16]. The relatively high thermal stability is possibly attributed to extensive hydrogen bonding in the solid state. The DSC showed no endothermic peak, indicating that the material does not melt before decomposition nor undergo a solid-solid phase transition. The single peak also indicates that the material does not dissociate into the two starting components that then decompose separately, but instead decomposes as a single entity. Integration of the peak gives a value for the heat of decomposition of 789.4 J/g , which corresponds to $180.8 \text{ kJ mol}^{-1}$. In comparison, NTO has a heat of decomposition of 1760 J/g [17], corresponding to $228.8 \text{ kJ mol}^{-1}$.

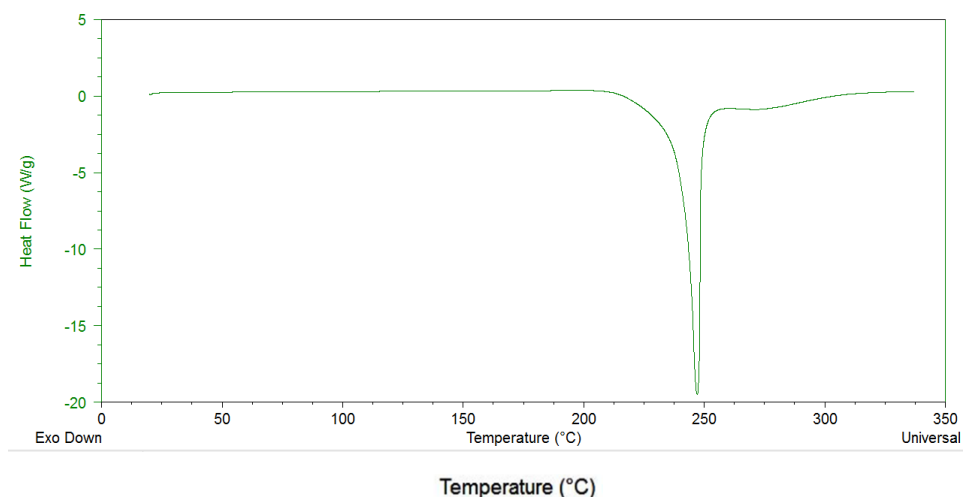


Fig 5.17 DSC graph of 3,5-DATNTO

BAM fall hammer Testing

3,5-DAT.NTO and NTO did not initiate with an impact of 100 J using the conventional device set up of impact device 1. Conducting an identical experiment with a change in impact device to a file plate adapter, allows for the addition of friction and delivery of more energy. With such a set-up, NTO demonstrated scorch marks, as seen in Fig 5.18; this illustrates a partial initiation. In contrast, 3,5-DAT.NTO showed no sign of discolouration nor scorch marks. This suggests that it is less sensitive to impact and friction. Of course, this is not an unequivocal conclusion, on account of the effective dilution of the energetic component NTO by the incorporation of the less energetic component, 3,5-DAT. Nonetheless the layered structure of 3,5-DAT.NTO is a likely contribution to the decrease in sensitivity.



Fig 5.18 White NTO with scorch marks (100 J) and yellow 3,5-DAT.NTO (100 J)

This layered motif, has previously been linked to insensitivity to stimuli in the energetic materials, such TATB and FOX-7. Both TATB and FOX-7 show considerable intermolecular hydrogen bonding between the -NH_2 and -NO_2 groups [18, 19], which form 2D sheets that stack in layers. Initially FOX-7 was expected to be as insensitive to impact as TATB, given the structural similarities, however, this is not the case. For TATB and FOX-7 $H_{50} = 490$ cm, impact energy = 120 J and $H_{50} = 126$ cm, impact energy = 31 J, respectively. As mentioned both systems are layered, but the layers within FOX-7 are zig-zag whilst the TATB layers are planar, which suggests that FOX-7 is more susceptible to shear strain. There are a few theories as to why layered materials would be less sensitive to impact. One of which is the concept that the hydrogen bonded sheets are capable of dissipating energy throughout the system rather than localising the energy into specific primary bonds that subsequently break.

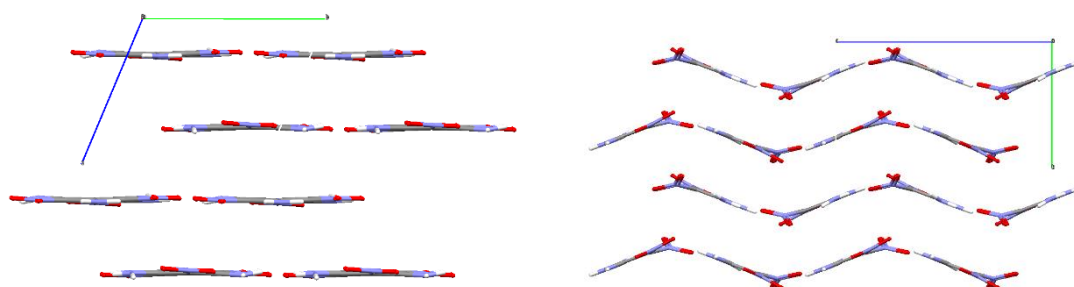


Fig 1.19 Crystal structure packing of TATB and FOX-7.

Detonation Velocity Calculations

From the experimentally determined density, chemical composition, and energy of formation (shown in Table 5.4) the detonation pressures and velocities were predicted using the EXPLO5 program [10]. The detonation parameters were calculated using the following values for the empirical constants in the Becker-Kistiakowsky-wilson equation of state (BKWN-EOS): $\alpha = 0.5$ $\beta = 0.154$ $\kappa = 9.37$ $\theta = 3650$ were used for 3,5-DAT.NTO. The detonation parameters calculated for 3,5-DAT.NTO are inferior to pure NTO. In addition to altering the detonation parameters, the addition of 3,5-DAT increases the nitrogen content, but decreases the oxygen balance.

Table 5.4 Physiochemical properties of 3,5-DAT.NTO and α -NTO

	3,5-DATNTO	NTO
Formula	C ₄ H ₇ N ₉ O ₃	C ₂ H ₂ N ₄ O ₃
Mr [g mol⁻¹]	229.2	130.0
T_m [°C]	-	-
T_d [°C]	247	267
N [%]	55	43
O [%]	-59.34	-24.60
ρ [g cm⁻³]	1.702	1.931
ΔH_L [kJ mol⁻¹K⁻¹]	492.9	-
ΔH_f° [kJ mol⁻¹K⁻¹]	-418.9	-100.0
T_{ex} [K]	1310	2862
V₀ [Lkg⁻¹]	808.2	733.6
P [GPa]	15.31	30.67
D [ms⁻¹]	6622	8369
Impact [J]	>100	>100

T_m, chemical melting point. T_d, decomposition point (DSC). N, nitrogen percentage. O, oxygen percentage balance. ρ , density from x-ray measurements. ΔH_L , lattice enthalpy. ΔH_f° , standard enthalpy of formation. T_{ex}, temperature of the explosion gases. V₀, Volume of the explosion gases. P, Detonation pressure. D, Detonation velocity. Impact, Tests according to BAM methods.

5.3.2 Salt of NTO and 3,4-Diamino-1,2,4-triazole

5.3.2.1 Introduction

The 3,4-DAT.NTO salt was first described by Zhang [4] in 2013 and has been reported to have a relatively high density (1.693 g/cm³) a high decomposition temperature, and a high calculated detonation velocity and pressure. However, the salt has also been described to be very sensitive to impact, flame and friction (3.18 J, 18.43 cm (H₅₀) and 70 %, respectively) [4]. It is of great interest for the current work on the basis that it possesses the same chemical composition as 3,5-DAT.NTO, which as just described, shows high density, decomposition temperature and VoD values, whilst being

particularly insensitive to impact. This large difference in results could arise from the difference in features of the crystal structure, such as 3,4-DAT.NTO does not have a layered structure.

Therefore an investigation into 3,4-DAT.NTO was initiated in order to further to compare its properties with 3,5-DAT.NTO using identical instrumentation.

5.3.2.2 Structural Properties of 3,4-Diamino-1,2,4-triazole.NTO

Initial Characterisation

Similar to the studies on 3,5-DAT.NTO, a combination of techniques was used to determine whether the product was a new material, such as a salt or co-crystal. Through slow solvent evaporation of an aqueous mixture of NTO and 3,4-DAT, yellow crystals were produced. PRXD measurements were conducted and the diffraction patterns are shown in Fig 5.20. The crystal structure of the previously reported 3,4-DAT.NTO (known as DATrNTO) [4] was kindly provided by the Zhang group to confirm whether the target material had been obtained. It is clear that the target material 3,4-DAT.NTO had been successfully synthesised. However, it appears that the sample is not pure. A small number of peaks could be assigned to the starting material, diamino-1,2,4-triazolium.chloride hydrate.

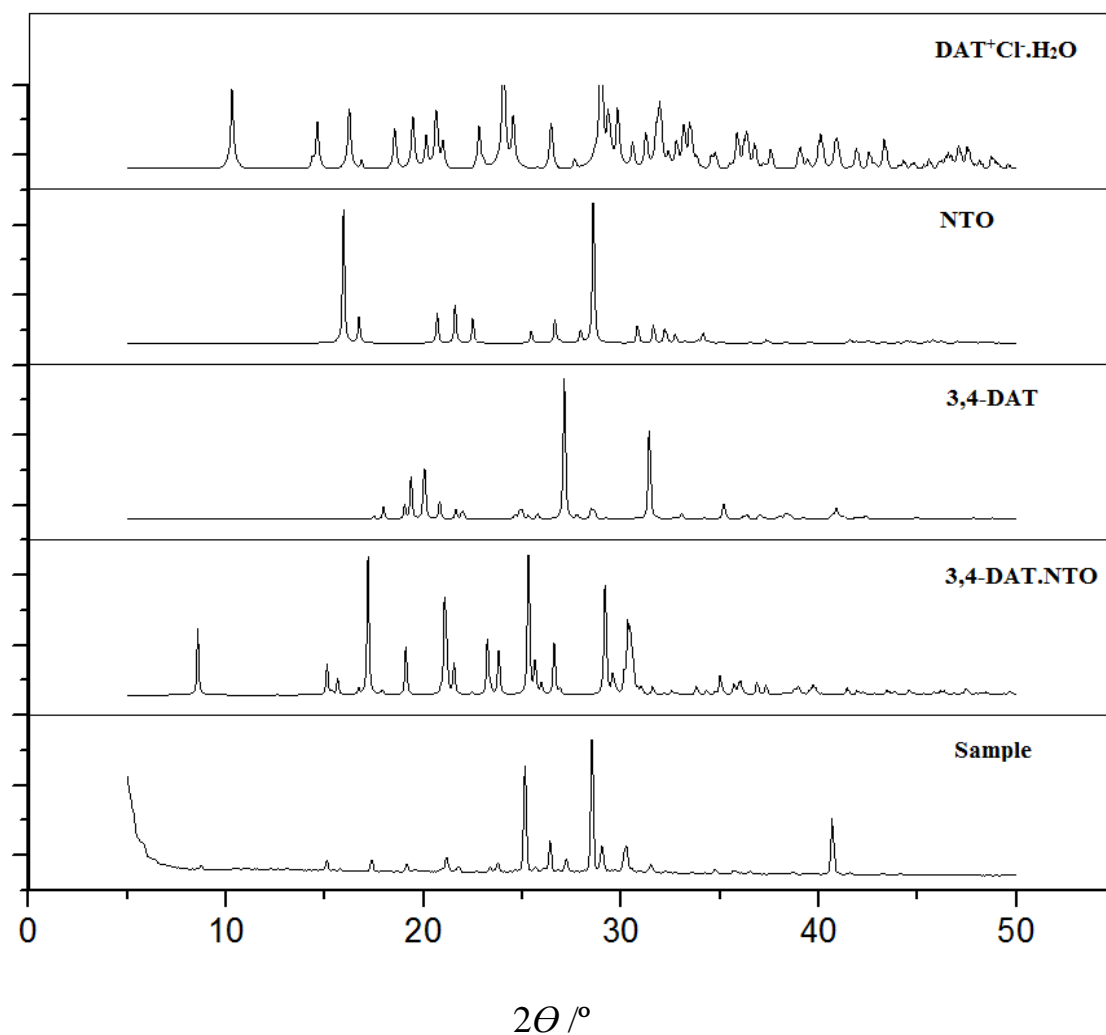


Fig 5.20 Simulated powder pattern of 3,4-DAT.NTO collected via single crystal X-ray diffraction [4], powder X-ray diffraction pattern of polycrystalline 3,4-DAT, NTO and sample (3,4-DAT.NTO), and starting materials: 3,4-DAT, NTO and $\text{DAT}^+.\text{Cl}^-.\text{H}_2\text{O}$ [20]

Rietveld refinements were performed on the powder pattern of the sample, using TOPAS, to wR_p of 11.38 %. The main component of the sample is the target material 3,4-DAT.NTO with a ratio of 85.9 %, as shown in Fig 5.21. In addition it was confirmed that $3,4\text{-DAT}^+.\text{Cl}^-.\text{H}_2\text{O}$ is present (9.6 %).

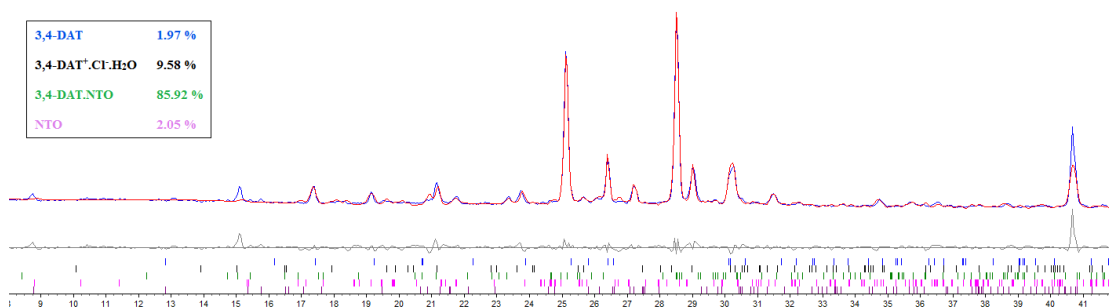


Fig 5.21 Rietveld refinement on the powder pattern of 3,4-DAT.NTO in TOPAS

Single Crystal X-Ray Diffraction

A few block-shaped, yellow crystals were screened and found to have different lattice parameters to those of the previously reported 3,4-DAT.NTO. The structure was subsequently solved and found to be a new polymorph of 3,4-DAT.NTO. From here onwards the polymorph described by Zhang will be denoted as α -3,4-DAT.NTO whilst the new polymorph is denoted as β -3,4-DAT.NTO.

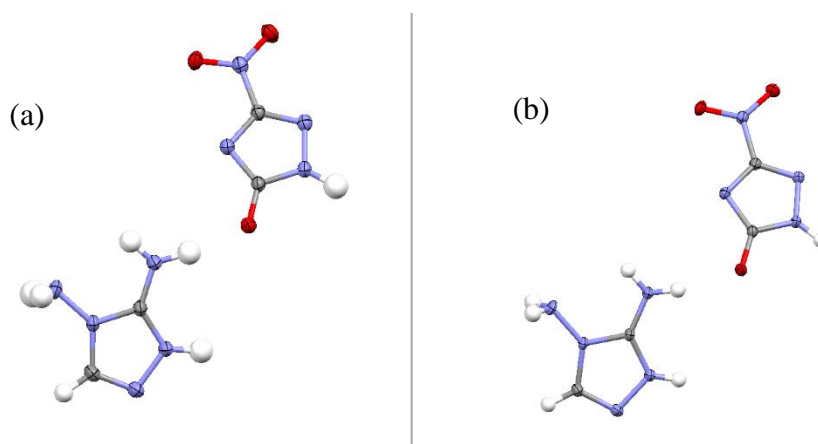


Fig 5.22 Asymmetric unit of **a** α -3,4-DAT.NTO and **b** β -3,4-DAT.NTO

β -3,4-DAT.NTO is a 1:1 salt of NTO and 3,4-diamino-1,2,4-triazole (3,4-DAT) crystallising in the $P2_1/n$ space group with one deprotonated nitrotriazolone (NTO^-) and one protonated 3,4-diamino-1,2,4-triazole (3,4-DAT^+) molecule in the asymmetric unit. The asymmetric unit is very similar to the α -form, with analogous hydrogen bonding connecting each molecule.

Table 5.5 Crystal structure parameters for polymorphs α - and β -3,4-DAT.NTO

	α-3,4-DAT.NTO	β-3,4-DAT.NTO
Empirical formula	C ₄ H ₇ N ₉ O ₃	C ₄ H ₇ N ₉ O ₃
Formula mass /g.mol⁻¹	229.19	229.19
Temperature /K	153	120
Crystal Size /mm	0.40 x 0.29 x 0.22	0.30 x 0.28 x 0.21
Crystal System	Monoclinic	Monoclinic
Space Group	<i>P</i> 2 ₁ / <i>c</i>	<i>P</i> 2 ₁ / <i>c</i>
Z	4	4
<i>a</i> /Å	10.323 (6)	12.305 (1)
<i>b</i> /Å	6.186 (4)	6.095 (2)
<i>c</i> /Å	14.080 (8)	12.521 (1)
β /°	91.047 (6)	110.179 (4)
Cell Volume /Å³	899.0 (9)	881.41 (6)
Density calculated / g.cm⁻³	1.693	1.727
Absorption coefficient /mm⁻¹	0.711	0.147
F(000) / Å	472	472
Final R₁ and wR₂ [I > 2σ(I)]	0.0460 0.1079	0.0460 0.1055
Largest diff. peak and hole /e.Å⁻³	0.26, -0.24	0.51, -0.37
Radiation type	Mo	Mo

When comparing the powder patterns simulated from the collected single crystal data, both patterns look similar (Fig 5.23). Hence, in the experimental powder pattern of the polycrystalline sample of 3,4-DAT.NTO it was difficult to distinguish visually which polymorph was present and in what ratio. After performing Rietveld refinements in TOPAS, it was shown that β -3,4-DAT.NTO was not present in the sample. In some cases small amounts of β -form is present. There is a potential that α -3,4-DAT.NTO is the thermodynamically stable form, given that DSC patterns of α -3,4-DAT.NTO was conducted by Zhang and no peak corresponding to a phase change was observed. However, a competitive slurry experiment would help determine which

form is the thermodynamic and kinetic product. It is possible that the grinding process of the larger single crystals, prior to powder diffraction resulted in interconversion to the α -3,4-DAT.NTO, is responsible for the lack of β -3,4-DAT.NTO.

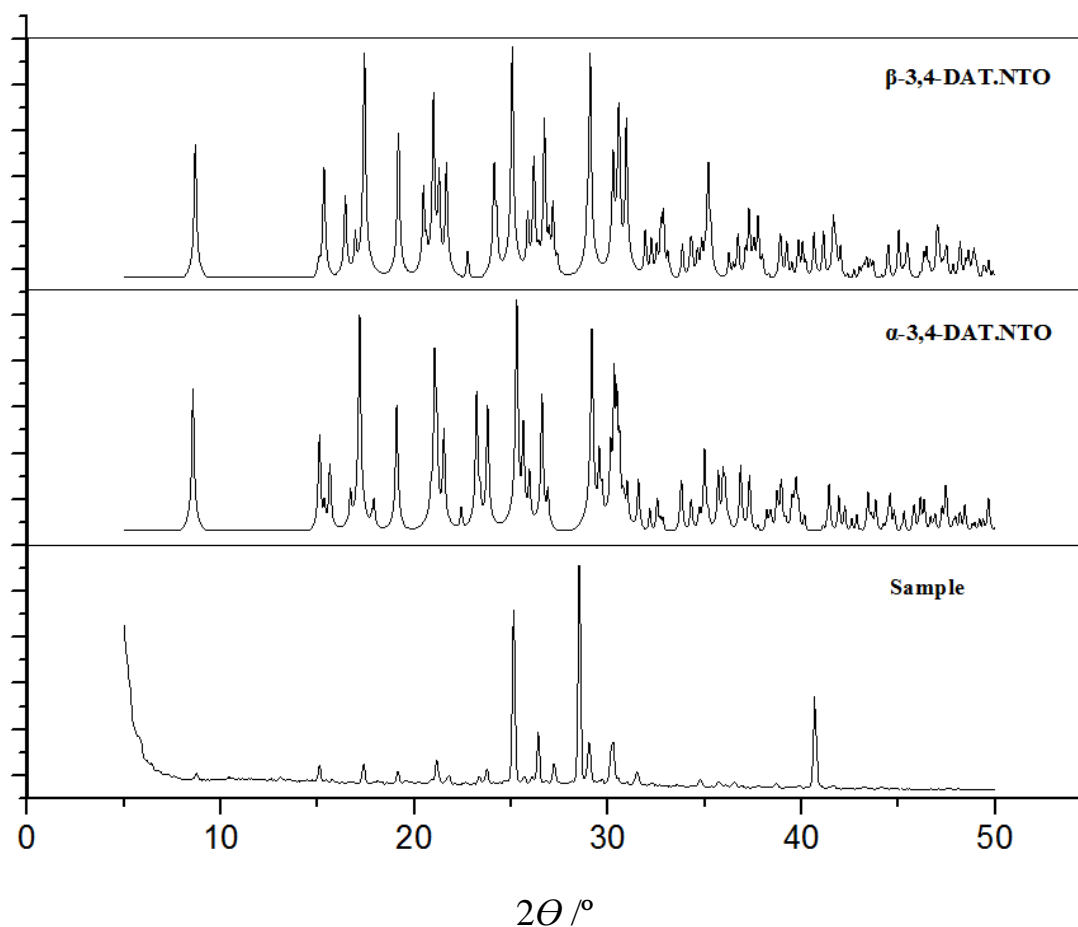


Fig 5.23 Simulated powder patterns of both forms of 3,4-DAT.NTO and collected powder X-ray diffraction pattern of 3,4-DAT.NTO sample.

When comparing the bond lengths and torsion within the NTO anion of each polymorph, it appears no significant difference occurs in planarity. Lengths of covalent bonds within $-\text{NO}_2$ are similar.

Table 5.6 Bond lengths and torsion angles of bonds within NTO- molecule for α - and β -3,4-DAT.NTO

	$C5-N7$ (Å)	$N7-O8$ (Å)	$N7-O9$ (Å)	$O9-N7-C5-N4$ (°)	$O8-N7-C5-N6$ (°)
<i>Alpha</i>	1.449 (2)	1.224 (2)	1.233 (2)	-9.3 (2)	-8.4 (2)
<i>Beta</i>	1.448 (2)	1.231 (2)	1.226 (2)	-9.3 (2)	-8.8 (2)

Intermolecular Contacts

One strong hydrogen bond is present between NTO^- and $3,4\text{-DAT}^+$ that relates to the direction of the proton transfer, $\text{N-H}\cdots\text{N}$. For the α -form, the $\text{N}\cdots\text{N}$ bond length and $\text{N-H}\cdots\text{N}$ angle are $2.820(2)$ Å and $167(1)^\circ$. For the β -form the corresponding values are $2.799(2)$ Å and $168.0(1)^\circ$. This indicates that the β -form has a slightly shorter and stronger H-bond. Unlike in the case of $3,5\text{-DAT.NTO}$, the two molecular ions do not create dimers, nor are they planar to one another. NTO^- and $3,4\text{-DAT}^+$ form an angle of 32.6° (correlated/calculated *via* planar rings of the molecules). For both polymorphs, one other strong hydrogen bond exists between NTO^- and $3,4\text{-DAT}^+$ and that is an $\text{N-H}\cdots\text{O}$ interaction.

The hydrogen bond networks surrounding the asymmetric units comprise a mixture of moderate and weak hydrogen bonds, all listed in Table 5.7. Overall, the β -form has a higher number of stronger H-bonding interactions than the α -form. These interactions are a likely contribution to the increased density of the β -form.

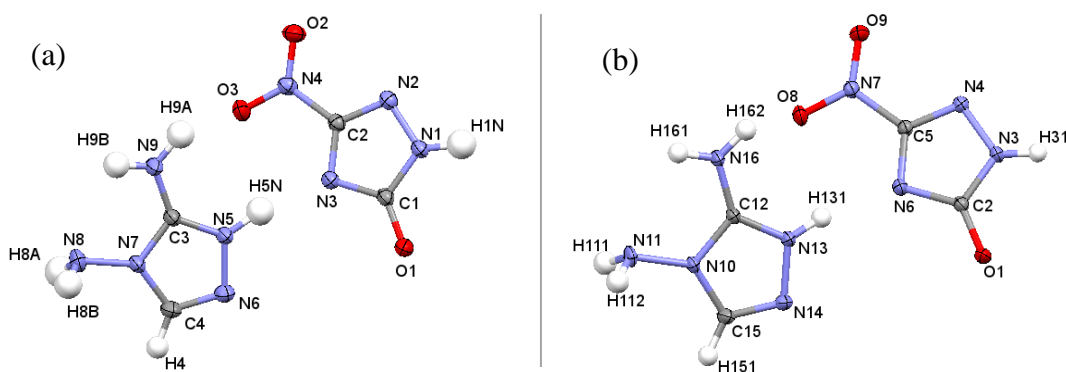


Fig 5.24 Molecular structure of **a** α -3,4-DAT.NTO and **b** β -3,4-DAT.NTO

Table 5.7 Hydrogen bonding lengths and angles within dimers and chains of NTO⁻ with 3,4-DAT⁺

	<i>D-H</i> ⋯ <i>A</i>	<i>D-H</i> [Å]	<i>H</i> ⋯ <i>A</i> [Å]	<i>D</i> ⋯ <i>A</i> [Å]	<i>D-H</i> ⋯ <i>A</i> [°]
α-3,4-DAT.NTO	N5-H5N ⋯ N3	1.00 (2)	1.83 (2)	2.820 (2)	167 (1)
	N9-H9A ⋯ O1	0.99 (2)	1.85 (2)	2.815 (2)	165 (1)
	N9-H9B ⋯ N6	0.90 (2)	2.17 (2)	3.000 (2)	153 (2)
	N8-H8A ⋯ N3	0.91 (2)	2.69 (2)	3.599 (2)	171 (2)
	N8-H8B ⋯ O1	0.95 (2)	2.08 (2)	2.982 (2)	158 (2)
β-3,4-DAT.NTO	N16-H162 ⋯ O1	0.871 (2)	1.933 (1)	2.791 (2)	168.2 (1)
	N13-H131 ⋯ N6	0.878 (2)	1.934 (2)	2.799 (2)	168.0 (1)
	N16-H161 ⋯ N14	0.892 (1)	2.108 (1)	2.950 (2)	157.1 (1)
	N11-H112 ⋯ N4	0.885 (2)	2.206 (1)	2.984 (2)	146.4 (1)
	N11-H111 ⋯ O8	0.878 (1)	2.398 (1)	3.019 (2)	127.9 (1)
	N11-H112 ⋯ O9	0.885 (2)	2.707 (1)	3.273 (2)	122.9 (1)

Packing/ electrostatic interactions

The packing arrangements of both polymorphs are very similar, but with a few key differences. The main difference is the arrangement of NTO⁻ molecular ions; this can be best seen along the *b*-axis, shown in Figure 5.25. Nitro-groups point towards each other in one polymorph (β-3,4-DAT.NTO), whilst in the other they are pointing in the same direction. Expanding upon the hydrogen bonding along the *a*-axis, it is clear that this small difference creates a big difference in the overall packing network (Fig 5.26).

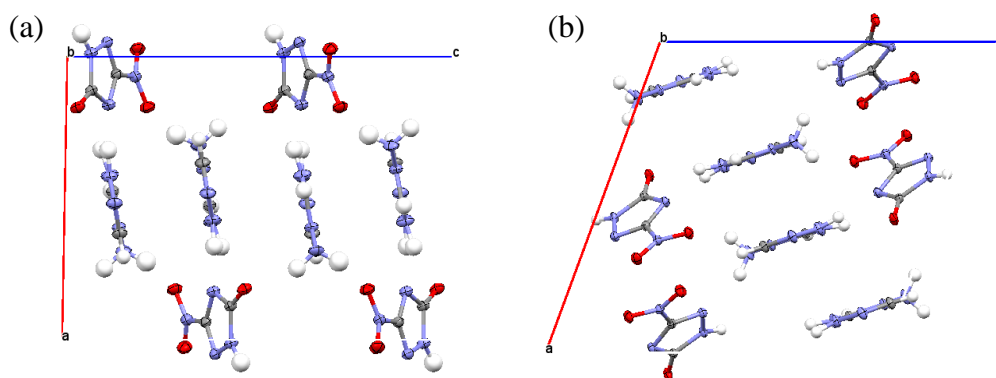


Fig 5.25 Unit cell of **a** α -3,4-DAT.NTO and **b** β -3,4-DAT.NTO

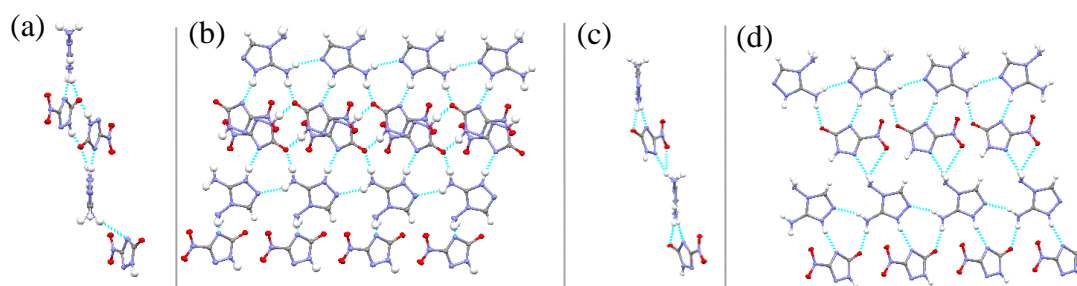


Fig 5.26 Hydrogen bonding network within **a, b** α -3,4-DAT.NTO and **c, d** β -3,4-DAT.NTO

NTO⁻ anions are arranged in a herring-bone formation in both polymorphs, but the hydrogen bonding connecting NTO⁻ ions is different (Fig 5.27). This is shown more evidently when observing the NTO stacks. The β -form has a distance between stacks of 3.056 Å; whilst the α -form has a distance between stacks of 3.064 Å. It seems this small increase in distance within the α -form slightly prohibits (or could be a result of lack of) hydrogen bonding that is seen in the β -form. This contributes further evidence as to how the β -form possesses a higher density.

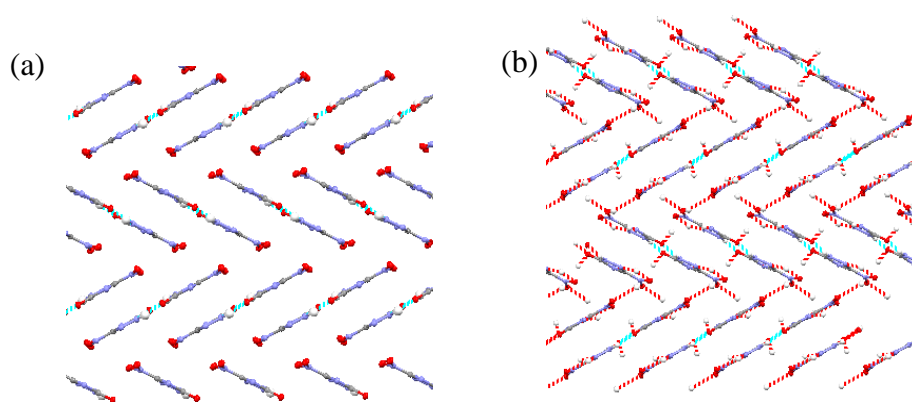


Fig 5.27 Packing of NTO^- within **a** α -3,4-DAT.NTO and **b** β -3,4-DAT.NTO

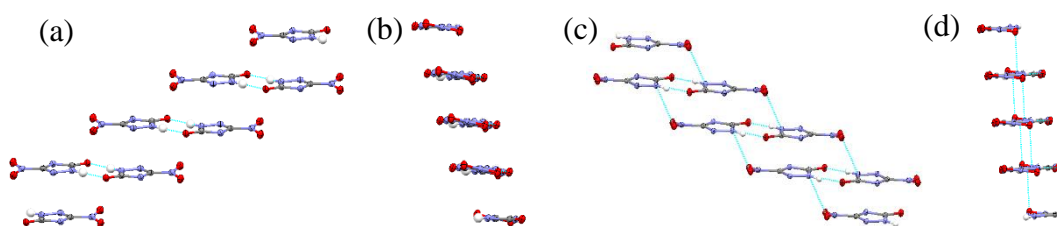


Fig 5.28 Packing of NTO^- within **a, b** α -3,4-DAT.NTO and **c, d** β -3,4-DAT.NTO

Similar to many other salts and co-crystals of NTO, the crystal density of both polymorphs of 3,4-DAT.NTO lie approximately midway between the densities of the co-formers, as shown in Fig 5.29. The unit cell volumes are very similar for both polymorphs, however beta is slightly denser, therefore could have a greater VoD which is favourable of the two polymorphs.

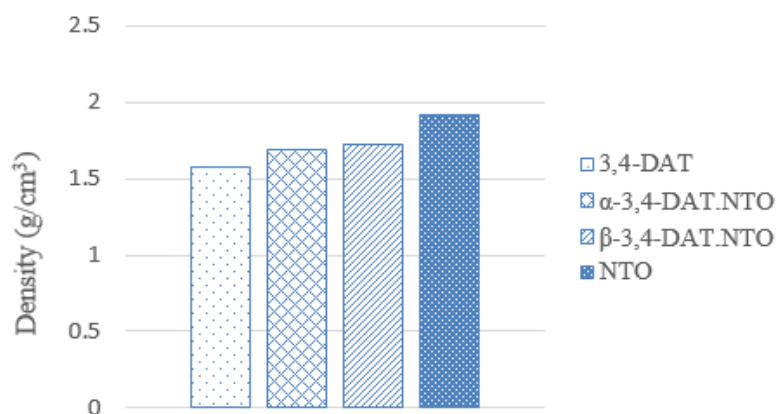


Fig 5.29 Density plots of starting material, 3,4-DAT and α -NTO at room temperature, and salts α -3,4-DAT.NTO and β -3,4-DAT.NTO at 153 and 120 K, respectively [4, 15, 21]

5.3.2.3 Physical Properties of 3,4-Diamino-1,2,4-triazole.NTO

To assess the energetic and physical properties of 3,4-DAT.NTO the thermal stability (DSC) and sensitivity to impact were experimentally determined. In addition, the heat of formation was calculated from the lattice enthalpy and heat of formation of cation and anion, in order to determine the detonation parameters using the program EXPLO5 V6.03.

Differential scanning calorimetry

DSC measurements of α -3,4-DATNTO were performed at the Cavendish Laboratory, Cambridge with a linear heating rate of 10 K min^{-1} . The plot, Fig 5.30, indicates that the sample is potentially not completely pure at the time of testing. Given the powder patterns recorded during initial characterisation it is likely that small amounts of $\text{DAT}^+\text{Cl}^-\text{H}_2\text{O}$ is still present even after purification methods. Peak at $220.4 \text{ }^\circ\text{C}$ is slightly lower than the peak ($236.7 \text{ }^\circ\text{C}$) seen by Zhang [4], yet the peak shape is similar for both. The unusual peak at $220.9 \text{ }^\circ\text{C}$ within the exothermic peak could be indicative of the β -form or possibly another form of impurity, presumably the starting material $\text{DAT}^+\text{Cl}^-\text{H}_2\text{O}$.

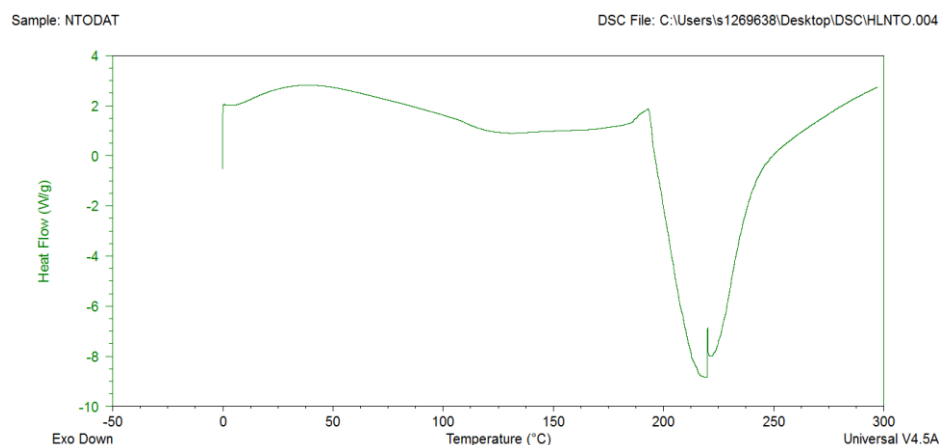


Fig 5.30 DSC plot of α -3,4-DAT.NTO

BAM Fall Hammer

BAM impact testing was conducted, at the Cavendish Laboratory, Cambridge, on α -3,4-DAT.NTO. Due to difficulties in synthesising a large enough sample of α -3,4-DAT.NTO during scale up, the method of 6-in-1 was used to establish the impact sensitivity of the material. At 30 J the sample initiated. As low as 12.5 J the material did not decompose, but discolouration took place. At 10 J the material did not give any indication of a “go” result for 6 attempts. In comparison to the results gathered by Zhang [4] which indicated the sample is sensitive to impact at 3.18 J this is a rather different result. There are numerous reasons for such an observation; firstly the device for testing both results is different and secondly the sample tests here could potentially have a small amount of the β -form present. Furthermore the lack of full 30-trial Bruceton testing may have resulted in a less accurate result.

Due to difficulties separating the two polymorphs, insufficient quantities of pure β -3,4-DAT.NTO were obtained, and so it was not possible to gain impact sensitivity data for this form. Further work is required to isolate this polymorph on a larger scale.

Table 5.8 BAM hammer impact testing, 1-in-6 method for α -3,4-DAT.NTO

Mass/ Height (kg/cm)	Drop Energy (J)	1	2	3	4	5	6
5/60	30	X					
5/40	20	X					
5/35	17.5	O	O	X			
5/30	15	O	X				
5/25	12.5	O*	O	O*	O*	O	O*
5/20	10	O	O	O	O	O	O

* Colour change

Overall, 3,4-DAT.NTO is much more sensitive than 3,5-DAT.NTO (> 100 J). This difference is likely due to the structure, especially as chemical composition is identical and other parameters are similar. As previously mentioned, the crystal structure of 3,5-DAT.NTO is layered whilst 3,4-DAT.NTO is not. Granted there is a small difference in testing, 3,5-DAT.NTO full Bruceton testing was conducted. In addition there is a small difference in hydrogen bonding, 3,4-DAT.NTO has less H-bonds and that are weaker. It is possible that the weak intermolecular bonding and packing structure are responsible for the increased impact sensitivity of the material.

Detonation Velocity Calculations

From the experimentally determined density, chemical composition, and energy of formation the detonation pressure and velocity were predicted using EXPLO5 V6.03 code [10] and shown in Table 5.9. Both detonation velocity and pressure are calculated to be higher in EXPLO5 than previously published work. The following values for the empirical constants in the Becker-Kistiakowsky-Wilson equation of state (BKWN-EOS): $\alpha = 0.5$ $\beta = 0.38$ $\kappa = 9.32$ $\theta = 4120$ were used for α - and β -3,4-DAT.NTO.

Zhang has reported that α -3,4-DAT.NTO has a detonation velocity of 6320 m/s. This value was calculated through equations by Keshavarz [4]. The detonation pressure was also calculated to be 17.1 GPa. When comparing these with values calculated through EXPLO5 (7983 m/s and 23.44 GPa) it is clear the different calculations result in very different values. Some calculations over-compensate in comparison to actual experimental values. However, to confirm the accuracy of EXPLO5, NTO was calculated alongside with a of ΔH_f° -100 kJ mol⁻¹K⁻¹ (average value reported for NTO) [16]. The output values of 8369 m/s and 30.67 GPa correspond to reported values for NTO [16].

Table 5.9 Physiochemical properties of α -3,4-DAT.NTO, β -3,4-DAT.NTO and α -NTO

	α -3,4-DATNTO	β -3,4-DATNTO	NTO
Formula	C ₄ H ₇ N ₉ O ₃	C ₄ H ₇ N ₉ O ₃	C ₂ H ₂ N ₄ O ₃
M_r [g mol⁻¹]	229.17	229.17	130.06
T_d [°C]	219.6	-	267
N [%]	55	55	43
O [%]	-59.34	-59.34	-24.60
ρ [g cm⁻³]	1.693	1.727	1.931
ΔH_L [kJ mol⁻¹K⁻¹]	494.6	497.2	-
ΔH_f° [kJ mol⁻¹K⁻¹]	280	278	-100
T_{ex} [K]	2841	2817	2862
V₀ [Lkg⁻¹]	818.0	816.5	733.6
P [GPa]	23.44	24.41	30.67
D [ms⁻¹]	7983	8141	8369
Impact [J]	10	-	>100

T_m, chemical melting point. T_d, decomposition point (DSC). N, nitrogen percentage. O, oxygen percentage balance. ρ , density from x-ray measurements. ΔH_L , lattice enthalpy. ΔH_f° , standard enthalpy of formation. T_{ex}, temperature of the explosion gases. V₀, Volume of the explosion gases. P, Detonation pressure. D, Detonation velocity. Impact, Tests according to BAM methods.

5.4 Conclusions

Two triazolium salt of NTO were synthesised and characterised using single-crystal X-ray diffraction. From the crystal structure, 3,5-DAT.NTO adopts a layered structure, comprising multiple hydrogen-bonded sheets. The synthons on DAT match well with NTO to form acceptor donor pairs. Layered structures are also seen in TATB. Moreover, it is also less sensitive to impact, than NTO using a non-standard testing device (impact device 2) which involves friction. The decomposition temperature of 3,5-DAT.NTO is slightly lower than NTO and calculations using EXPLO5 indicate promising detonation parameters, although considerably less power than NTO.

Upon repeating the synthesis of 3,4-DAT.NTO, a new polymorph was obtained and its crystal properties were studied. Both polymorphs are very similar, but β -3,4-DAT.NTO has a higher crystal density, with stronger hydrogen bonding. Due to difficulties in synthesising a large quantity of the β -form it was not possible to obtain the physical properties of the β -form. Physical property testing was carried out on the α -form to compare with data previously reported [4]. It appears the sample is not as pure as the materials reported by Zhang. Small quantities of the β -form or starting material could be present in the sample, causing an extra broadening of the exothermic peak during DSC testing, or be responsible for the endothermic peak at the base. Calculation of VoD contrasted with the values calculated by Zhang, 6320 m/s [4]. It is possible that one method of calculating detonation parameters overestimates the results.

Overall, calculated values of the detonation parameters indicate that 3,4-DAT.NTO has more favourable detonation velocity and pressure than 3,5-DAT.NTO. However, 3,5-DAT.NTO is much less sensitive to impact and better thermal stability. These properties are not distinctly attributed to the crystal packing alone. The chemistry of the co-former does also contribute to the sensitivity. For example, 3,4-DAT does possess an N-N covalent bond, whilst 3,5-DAT does not, this could be a factor for the increased impact sensitivity of 3,4-DAT.NTO compared to 3,5-DAT.NTO.

5.5 Suggestions for Further Work

Although this investigation into NTO.triazolium salts yielded interesting results, more questions are raised. The isolation and scale up of β -3,4-DAT.NTO for property testing is required for comparisons with α -form. Further sensitivity data, such as friction and shock or electrostatic discharge are required on all materials. Once these values are obtained, material could be regarded as insensitive or sensitive and placed in a class and division that can be understood by UN Recommendations on the Transport of Dangerous Goods.

TGA experiments alongside DSC testing is required to fully understand the endothermic and exothermic peaks. Currently it is unclear when the materials begin to decompose and whether some peaks are due loss of solvent. In addition, it would be

beneficial to investigate thermal processes on the heat stage to visualise melting and decomposition.

Furthermore, a continuation into triazole co-formers, such as 1,3-diamino-1,2,4-triazole, potential 3,4,5-triamino-1,2,4-triazole should be explored.

5.6 References

1. Y. H. Ren, F. Q. Zhao, J. H. Yi, K. Z. Xu, H. X. Ma, R. Z. Hu, J. R. Song, J. *Iran Chem Soc*, 2012, **9**:407-414
2. J-R. Li, B-R. Chen, Y-X. Ou, X-S. Cui, Z-C. Lui, *Acta Cryst*, 1992, **C48**:1540-1542
3. H. Xue, H. Gao, B. Twamley, J. M. Shreeve, *Chem Mater*, 2007, **19**(7):1731-1739
4. J-T. Wu, J-G. Zhang, X. Yin, M. Sun, T-L. Zhang, *Z Anor Allg Chem*, 2013, **639**(12-13):2354-2358
5. Agilent (2014). *CrysAlis PRO*. Agilent Technologies Ltd, Yarnton, Oxfordshire, England.
6. R.H. Blessing, *Acta Cryst.*, 1995. **A51**, 1-6
7. P. W. Betteridge, J. R. Carruther, R. I. Cooper, K. Prout, D. J. Watkin, *J. Appl. Cryst.*, 2003, **36**:1487.
8. L. J. Farrugia, *J. Appl. Cryst.* 2012, **45**, 849-854.
9. C. D. Fuh, J. S. Lee and C. M. Liaw, *Journal of Data Science*, 2003, **1**, 83-101
10. M. Sućeska, EXPLO5, v. 6.03, (2015), Brodarski Institute, Zagreb, Croatia.
11. C. F. Kroeger, W. Freiburg, *Z. Chem.*, 1965, **5**, 381.
12. I. Matulková, J. Cihelka, M. Pojarová, K. Fejfarová, M. Dušek, P. Vaněk, J. Kroupa, R. Krupková, J. Fábry and I. Němec, *Cryst Eng Comm*, 2012, **14**, 4625-4636
13. Macrae CF, Edgington PR, McCabe P, Pidcock E, Shields GP, Taylor R, Towler M, Van de Streek J (2006) *J. Appl. Cryst.* **39**:453-457.
14. G. L. Starova, O. V. Frank-Kamenetskaya, V. V. Makarskii, V. A. Lopirev *Kristallografiya, Crystallogr.Rep.*, 1980, **25**, 1292
15. N. Bolotina, K. Kirschbaum and A. A. Pinkerton, *Acta Cryst.* (2005). **B61**, 577-584

16. M. W. Smith, M. D. Cliff, *NTO-Based Explosive Formulations*, DSTO Aeronautical and Maritime Research Laboratory, Australia, 1999
17. G. T. Long, B. A. Brems, and C. A. Wight, *J. Phys. Chem. B*, 2002, **106**, 4022-4026
18. H. H. Cady, A. C. Larson, *Acta Crystallogr.*, 1965, **18**, 48
19. U. Bemm, H. Ostmark, *Acta Crystallogr.*, 1998, **C54**, 1997
20. A.D.Naik, B.Tinant, A.Leonard, J.Marchand-Brynaert, Bao-Lian Su, Y.Garcia, *Cryst.Growth Des.*, 2011, **11**, 4034
21. I. S. Konovalova, S. V. Shishkina, B. V. Paponov, O. V. Shishkin, *Cryst Eng Comm*, 2010, **12**, 909

Chapter 6

High-Pressure Structural Studies of 3,4-DATNTO and 3,5-DATNTO

6.1 Introduction

6.1.1 Structure and Polymorphism of 3,4-DAT.NTO and 3,5-DAT.NTO

Previous chapters within this thesis have described a variety of NTO salts and co-crystals, some of which have exhibited interesting polymorphism induced by choice of solvent or by temperature changes.

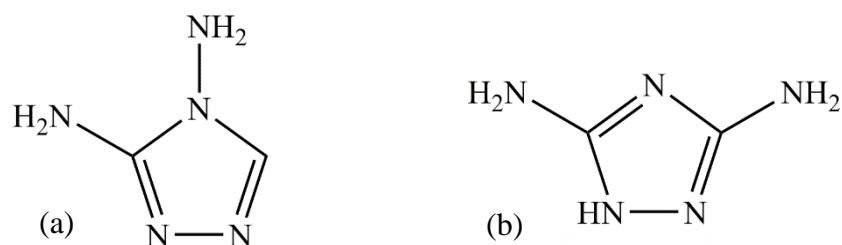


Fig. 6.1 Molecular structures of 3,4-DAT (a) and 3,5-DAT (b)

In particular, two polymorphs of 3,4-DAT.NTO were identified (α - and β -forms). By contrast, only one polymorph of 3,5-DAT.NTO was observed under ambient conditions. The very different packing arrangements observed for the polymorph of 3,4-DAT.NTO and 3,5-DAT.NTO have been highlighted in Chapter 5. At the same time, the two salts have very different impact sensitivities, with 3,5-DAT.NTO being insensitive to an impact of 100 J.

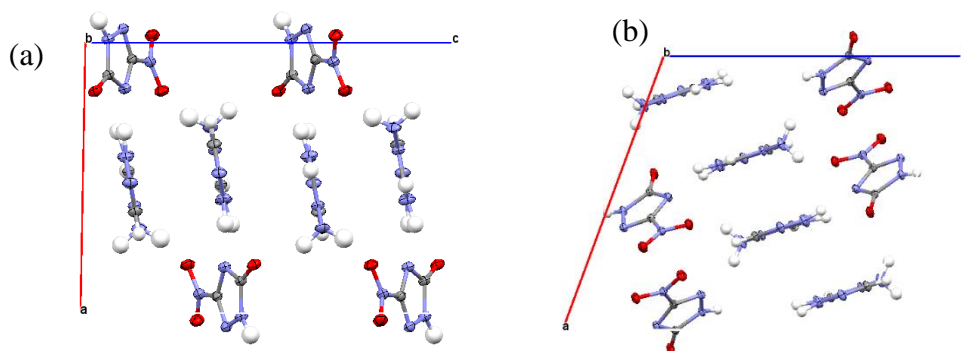


Fig 6.2 Unit cell of **a** α -3,4-DAT.NTO and **b** β -3,4-DAT.NTO

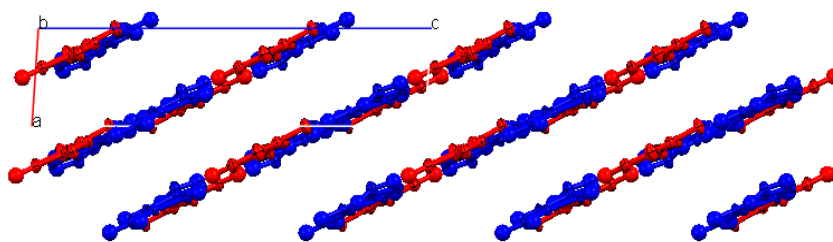


Fig 6.3 Layered structure of 3,5-DAT.NTO

Given the interesting layered structure of 3,5-DAT.NTO and the potential of finding an even more dense form of 3,5-DAT.NTO, in addition to the polymorphism observed for 3,4-DAT.NTO the aims of this work were:

- To obtain equations of state for 3,5-DAT.NTO and 3,4-DAT.NTO
- To investigate the high-pressure structural behaviour of both 3,5-DAT.NTO and 3,4-DAT.NTO.
- To determine the structure of any new high-pressure polymorphs and observe whether polymorphs can be retrieved at ambient conditions.

High pressure experiments were carried out using a DAC and X-ray diffraction at Diamond Light Source, and PEARL with neutron diffraction at ISIS Neutron Source. Neutron diffraction experiments were carried out for two main reasons; (1) to utilise the Paris-Edinburgh Press Cell for more precise loadings (in tonnes), and in-situ pressure measurements, in comparison to the sporadic diamond-anvil pressure steps, and (2) for improved identification of the “hydrogen” (deuterium) atom positions. Samples and pressure-transmitted medium are deuterated to remove large incoherent scattering produced by hydrogen atoms.

6.2 Experimental

6.2.1 Materials

Crystalline samples of 3,5-DAT.NTO and 3,4-DAT.NTO were obtained as described in Chapter 5. Deuterated powder samples of each salt, required for neutron diffraction studies, were prepared by re-crystallisation from D₂O. The phase purity of such samples of 3,4-DAT.NTO, 3,5-DAT.NTO and their deuterated analogues were confirmed by X-ray powder diffraction.

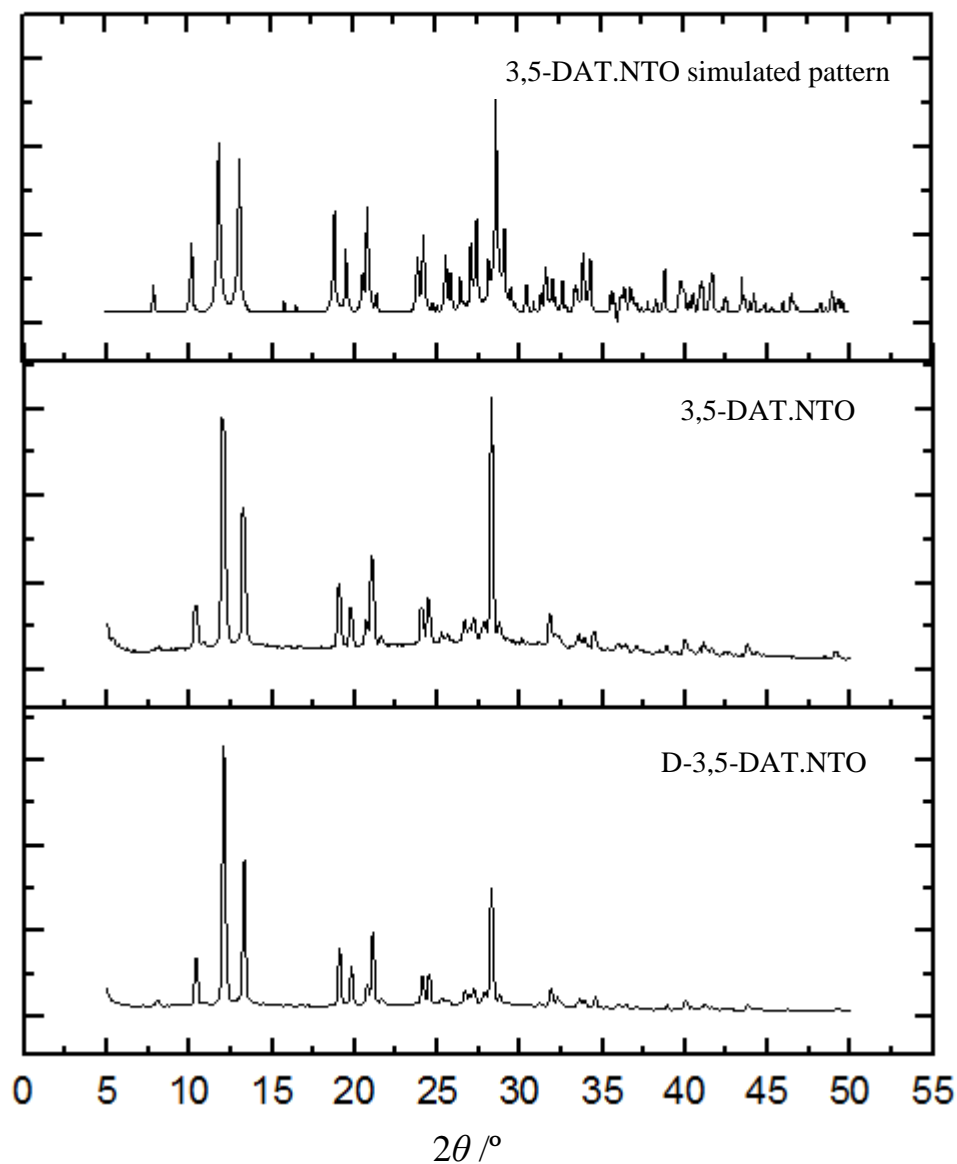


Fig. 6.4 Simulated pattern of 3,5-DAT.NTO from single crystal data and powder X-ray diffraction patterns of polycrystalline 3,5-DATNTO and deuterated 3,5-DAT.NTO ($\lambda = 1.54056$)

6.2.2 High-Pressure X-ray Powder Diffraction

High-pressure X-ray powder diffraction experiments were performed using a Merrill-Bassett diamond anvil cell (DAC) equipped with 600 μm culet diamonds and a 250 μm thick tungsten gasket (pre-indented to a thickness of 100-150 μm) with a 300 μm hole. Pressure measurements were made by monitoring the R1 fluorescence line of ruby spheres; methanol:ethanol was used as a pressure-transmitting medium. Data

were collected at the Extreme Conditions Beamline (I15) at the Diamond Light Source ($\lambda = 0.4134 \text{ \AA}$). The X-ray beam was collimated to a diameter of $50 \text{ }\mu\text{m}$ and samples were exposed for 60 s. 2D diffraction patterns were collected using a Mar345 image plate, and the data were processed using FIT2D [2].

6.2.3 High-Pressure Neutron Powder Diffraction

High-pressure neutron powder diffraction data were collected using the PEARL-HiPr diffractometer at the UK Spallation Neutron Source, ISIS, at the STFC Rutherford Appleton Laboratory. A lightly ground sample of each salt was loaded into an encapsulated TiZr gasket with pre-deuterated methanol:ethanol (4:1) as pressure-transmitting medium and a Pb sphere as the pressure calibrant. The capsule assembly was then compressed with a type V3b Paris-Edinburgh (P-E) press equipped with standard single toroid anvils with cemented ZTA anvils (Ni binder). The P-E press ram pressure was monitored and varied by means of a computer-controlled hydraulic system.

Time of flight (ToF) neutron powder diffraction data were collected using the $2\theta = 90^\circ$ detectors with a transverse (through-anvil) scattering geometry. The resulting summed pattern was then normalised with respect to the incident beam monitor and the scattering from a standard vanadium calibration sample. Lastly, the diffraction pattern intensity scale was corrected for the wavelength and scattering-angle dependence of the neutron attenuation by the anvil (ZTA) and gasket (TiZr) materials.

6.2.4 Ambient-Pressure Single-Crystal X-Ray Diffraction

Ambient-pressure, single-crystal X-ray diffraction data were collected by Dr. G. Nichol (crystallography service, university of Edinburgh) using Cu- K_α radiation on an Oxford Diffraction SuperNova dual wavelength diffractometer equipped with an Atlas CCD detector and an Oxford Cryostream-Plus low-temperature device (120 K). Data were integrated and a multi-scan absorption correction [3] was applied using ChrysAlisPro software package [4]. Structures were solved and refined using CRYSTALS [5]. All non-hydrogen atoms were refined anisotropically. The hydrogen atoms were found *via* Fourier difference/intensity.

6.3 Results and Discussion

6.3.1 Compression of the salt 3,5-diamino-1,2,-triazole.NTO

The initial focus of this study was to investigate the structural response of 3,5-DAT.NTO to compression and obtain an equation of state. X-ray powder diffraction patterns are shown in Fig. 6.5. It was possible to perform fullprofile Rietveld refinements on all of the patterns collected up to 2.12 GPa, demonstrating that the ambient-pressure phase remains stable up to this pressure. At the next pressure point, 2.89 GPa, a significant change was observed in the powder diffraction pattern, indicative of a phase transition. Notable differences in the pattern were observed at d -spacings of approximately 5 Å and 7 Å.

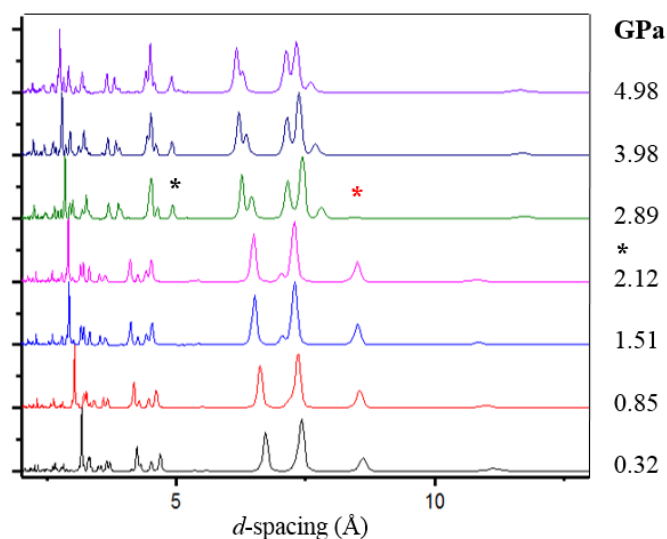


Fig. 6.5 Multiplot of the X-ray powder diffraction patterns collected during 3,5-DAT.NTO in MeOH/EtOH

Upon further compression to 4.98 GPa, no further changes in the diffraction patterns were observed. Decompression of the sample to ambient pressure, from the maximum pressure of 4.98 GPa, was performed in 2 steps. At 1.54 GPa, the diffraction pattern indicates that the sample had transformed back to its original phase. This suggests that the new phase is stable only at elevated pressures at ambient temperature.

In order to obtain complementary structural data and more pressure points, a neutron powder diffraction study was performed using PEARL-HiPr beamline (ISIS) using a Paris-Edinburgh Cell up to a maximum pressure of 5.33 GPa.

A multi-plot of a selection of the neutron powder diffraction patterns collected is presented in Fig 6.4. It should be noted that the intense peak at 2.8-3.2 Å dominates the pattern. When focusing on a smaller d-spacing range, as shown in Fig 6.5, there is clear evidence of a phase transition occurring between 2.18 and 2.37 GPa. New peaks appear at ~3.9 Å and ~3.05 Å whilst peaks at ~ 3.19 Å disappear. Upon further compression to 5.334 GPa, no further changes in the diffraction patterns were observed, this is in agreement with the results obtained from powder X-ray diffraction.

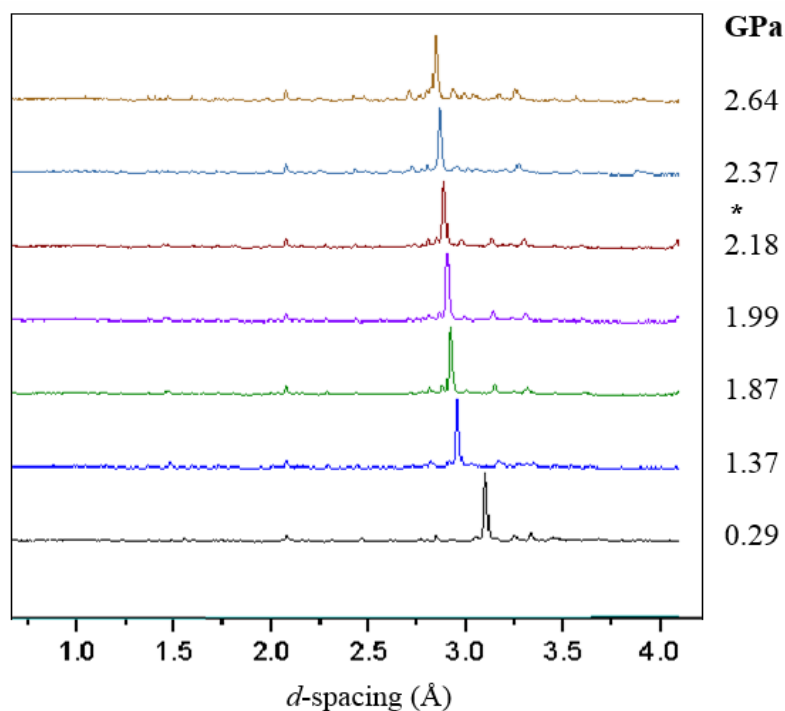


Fig. 6.6 Multi-plot of the neutron powder diffraction patterns collected for D-3,5-DAT.NTO in MeOD/EtOD

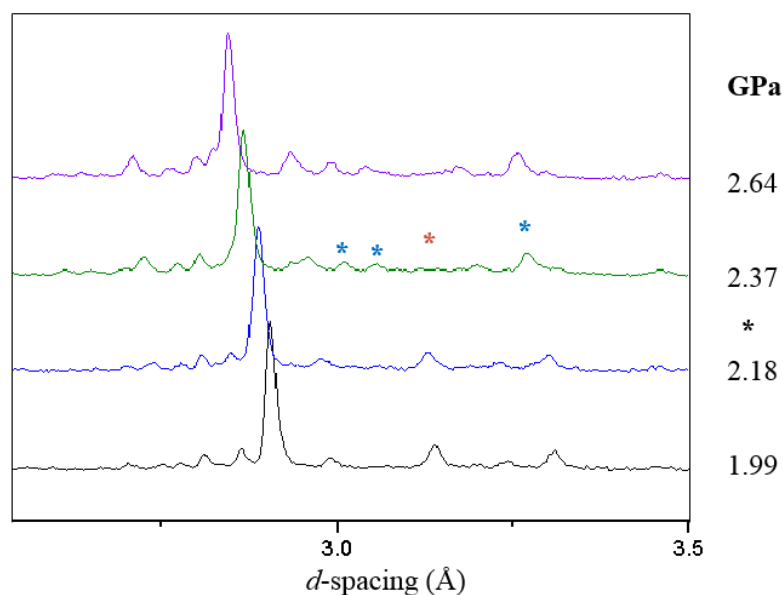


Fig. 6.7 Multi-plot of the neutron powder diffraction patterns collected for D-3,5-DAT.NTO in MeOD/EtOD

The variations in the unit cell parameters (a , b , c , β and V) of the ambient-pressure phase of 3,5-DAT.NTO are represented graphically in Fig 6.8. The a -axis and c -axis are the most compressible axes (reduced by $\sim 4\%$ and $\sim 2.3\%$, respectively); whilst the b -axis compresses very little ($\sim 0.05\%$). These observations can be rationalised by consideration of the crystal structure, (Fig 6.9) in which the strong hydrogen bonded 2D sheets extend along the b -axis with the weaker π -stacking layers forming in the a - c direction. In addition, it is worth noting the reflection corresponding to interlayer spacing with Miller indices (1 0 2) shifts substantially to shorter d-spacing with increased pressure.

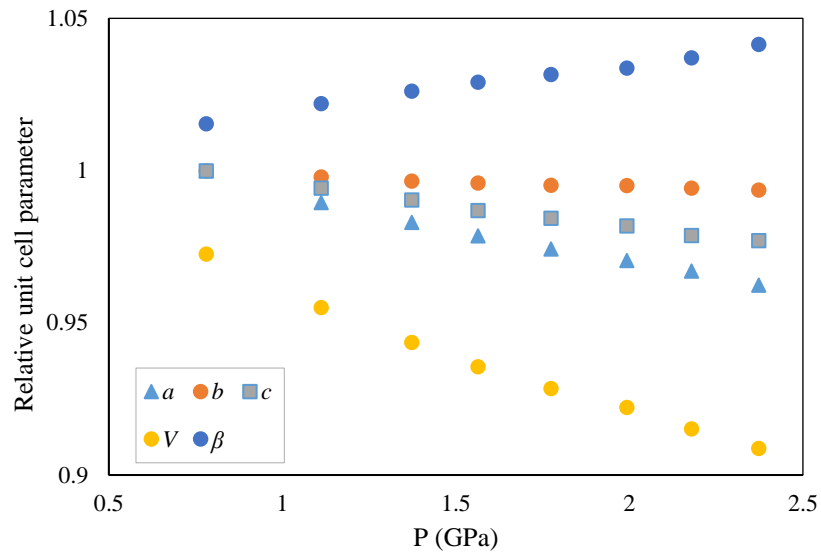


Fig. 6.8 Relative compression of the unit cell axes of D-3,5-DAT.NTO, between 0.3 and 2.4 GPa, highlighting the shortening of the *a*- and *b*-axes

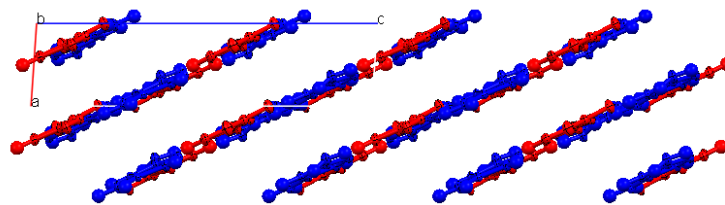


Fig 6.9 The packing observed in 3,5-DAT.NTO viewed down the *b*-axis

The compression behaviour of the unit cell volume for phase I of 3,5-DAT.NTO has been fitted to a 3rd-order Birch-Murnaghan equation of state (EoS) with $V_0 = 925.7 \text{ \AA}^3$, $B_0 = 8.2 \text{ GPa}$ and $B'_0 = 14.7$. In comparison to the values obtained from the equation of state for NTO (unpublished work), $V_0 = 909.25 \text{ \AA}^3$, $B_0 = 11.2 \text{ GPa}$ and $B'_0 = 10.6$, it appears that 3,5-DAT.NTO is slightly more compressible than NTO. This is significant since the compressibility can be potentially linked to processability and sensitivity to impact – cushioned effect. In addition the increased compressibility is most likely due to the layered structure of 3,5-DAT.NTO.

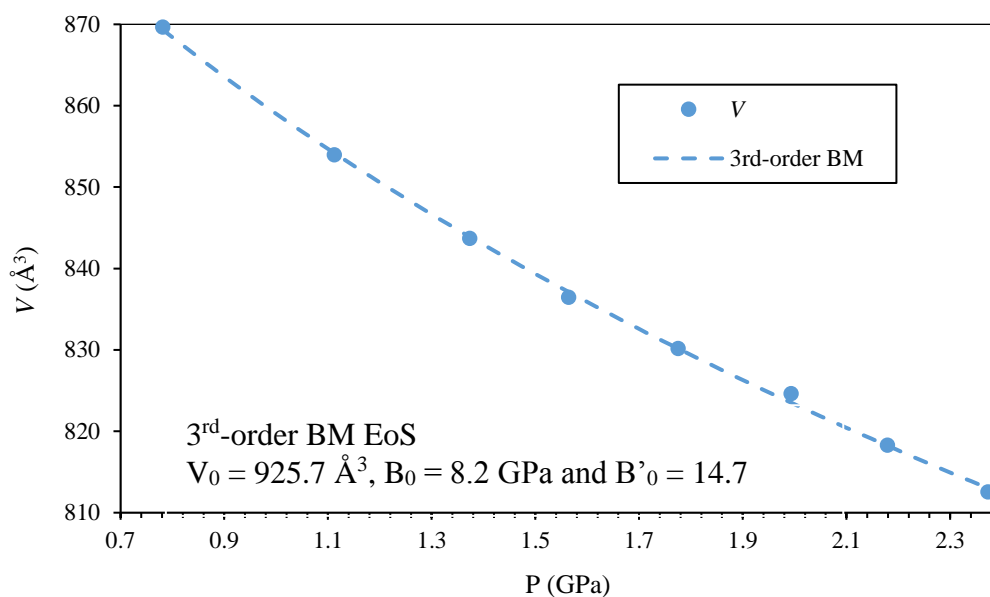


Fig 6.10 the B-M EoS that has been fit to the PV-plot

The high-pressure phase of 3,5-DAT.NTO was observed in both the X-ray and neutron studies. The phase change was observed between 2.12 GPa and 2.87 GPa in the X-ray experiment and between 2.18 GPa and 2.37 GPa in the neutron experiment. Phase II of 3,5-DAT.NTO persists to 5.33 GPa. Attempts were made to index these patterns using DASH and FOX. The most reasonable parameters determined through indexing are shown in Table 6.1.

Table 6.1 Unit cell parameters of 3,5-DAT.NTO at ambient, 2.37 and 4.98 GPa.

Values for phase II have been calculated through various methods.

Pressure (GPa)	Phase	Space group	Volume (Å ³)	<i>a</i> (Å)	<i>b</i> (Å)	<i>c</i> (Å)	α (°)	β (°)	γ (°)
Ambient	I	$P2_1/c$	894.13	3.55	17.23	14.65	90	93.9	90
2.37	I	$P2_1/c$	812.56	3.38	17.03	14.11	90	97.8	90
4.98 ^a	II ^a	$P2_1/c$	713.80	15.450	3.1657	14.849	90	100.64	90
4.98 ^b	II ^b	$P2_1/c$	719.514	14.893	3.178	15.471	90	100.66	90
4.98 ^c	II ^c	$P2_1/m$	736.648	14.904	3.225	15.591	90	100.58	90

a) DASH indexing, b) FOX indexing, c) DASH indexing with space group as $P2_1/m$

The crystal system remains monoclinic, with possibly a retention of space group. Prior to the phase transition the unit cell volume and beta angle were steadily decreasing and increasing, respectively, with pressure at a difference of ~6% and 3% respectively, this trend appears to continue into phase II. The compression of the unit cell volume (V) has been graphically represented separately in Fig 6.11 along with the two possible volumes obtained through indexing of the new phase at 4.89 GPa.

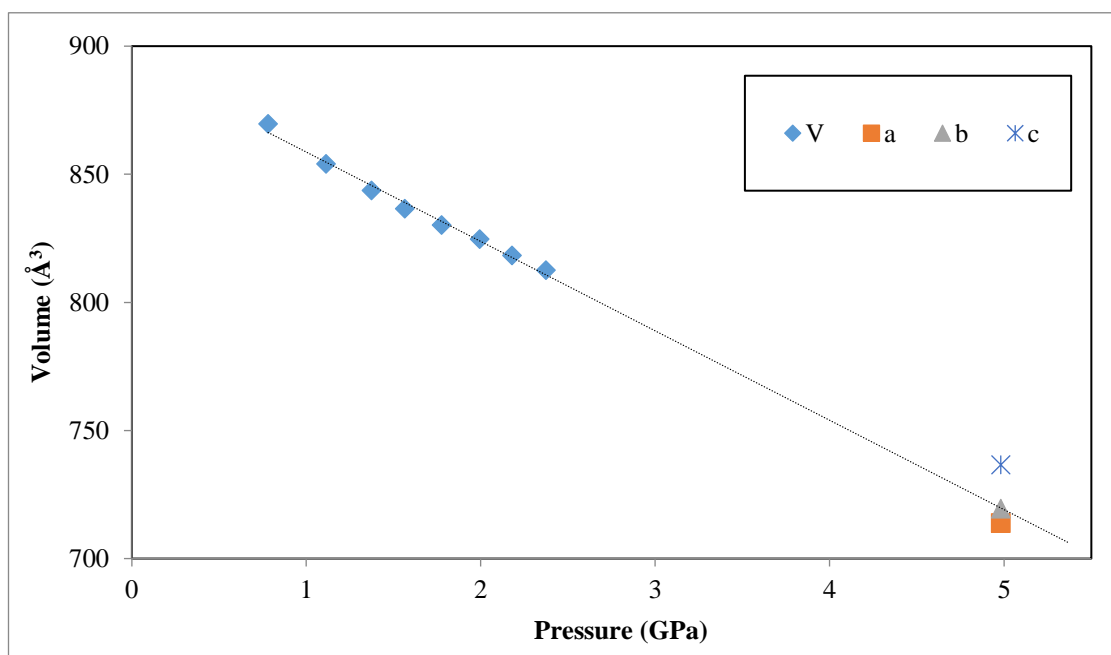


Fig. 6.11 Graphical illustration of the compression of 3,5-DAT.NTO, plot of the unit cell volume, as determined by X-ray powder diffraction, and potential unit cell volumes calculated from indexing of X-ray powder diffraction collected at 4.98 GPa. a) DASH indexing, b) FOX indexing, c) DASH indexing with space group of $P2_1/m$

The similarity in peak intensities and positions between the two phases suggests that the two phases have similar structures. Although structure solution has not been successful, it is clear that phase II of 3,5-DAT.NTO retains its layered packing arrangement; this can be inferred by the intense peak at $\sim 3 \text{ \AA}$ that is retained in the pattern. Structure solution using DASH provides a variety of possible structures, for phase II of 3,5-DAT.NTO at 4.98 GPa, not all of which make chemical sense on the basis of intermolecular contacts. The most sensible structure is shown in Fig 6.12, in which the layered packing structure is apparent.

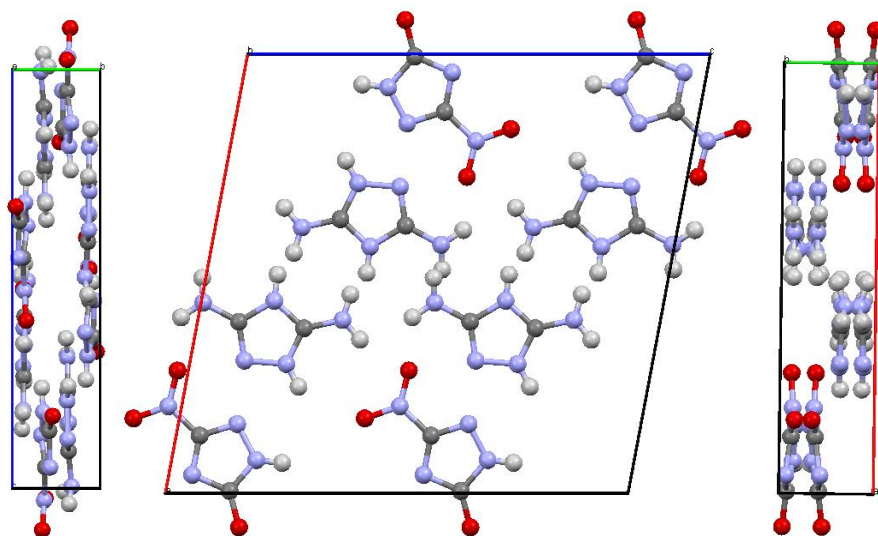


Fig. 6.12 Possible crystal Structure of phase II of 3,5-DAT.NTO, solved using DASH, viewed along the a-, b- and c-axes.

The compression behaviour of 3,5-DAT.NTO provides some insight into the potential impact and shock sensitivities of energetic materials that comprise layered structures. The facile compression of the layers provides an additional mechanism for the dissipation of energy when the material is shocked or subjected to impact. Hence this has relevance for the unusually low sensitivities of materials, such as TATB and FOX-7 that have layered structures. Although shock sensitivities measurements have not yet been recorded for 3,5-DAT.NTO, it is perhaps significant that the impact sensitivities of 3,5-DAT.NTO is substantially lower than that of 3,4-DAT.NTO, and that this may also be a consequence of the layered structure and its response to pressure. The fact that in the phase transitions to phase II of 3,5-DAT.NTO the layered structure is retained, suggests that 3,5-DAT.NTO would also be much less shock sensitive than 3,4-DAT.NTO.

6.3.2 Compression of the salt 3,4-diamino-1,2,-triazole.NTO

3,4-DAT.NTO has two polymorphs which are described in Chapter 5. The initial polymorph, α , was originally studied by Zhang [6] and found to be highly sensitive to impact in comparison to NTO. During attempts to prepare α -3,4-DAT.NTO at the University of Edinburgh a second polymorph, β -form was characterised. Therefore the

initial focus of this study was to investigate the polymorphism of α -3,4-DATNTO and compare its compressibility to that of the isomeric material 3,5-DAT.NTO.

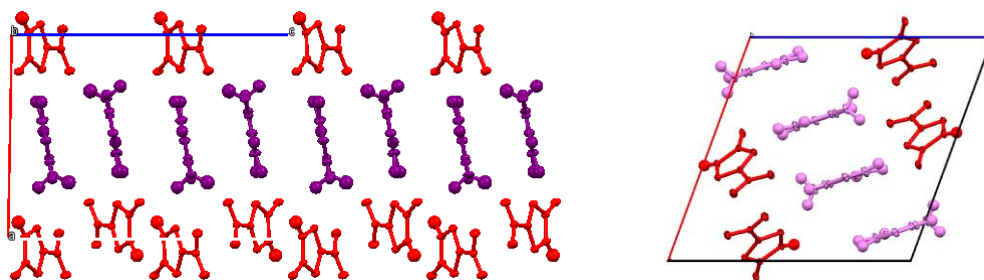


Fig. 6.13 Crystal packing of α -3,4-DAT.NTO and β -3,4-DAT.NTO, coloured by molecule type

Polycrystalline D- α -3,4-DATNTO was loaded into the anvils of a Paris-Edinburgh cell with methanol:ethanol (4:1) as a pressure transmitting medium. It was possible to perform Rietveld refinements on all patterns collected up to 6.08 GPa (Fig 6.14). This demonstrates that no phase transition occurs up to this pressure.

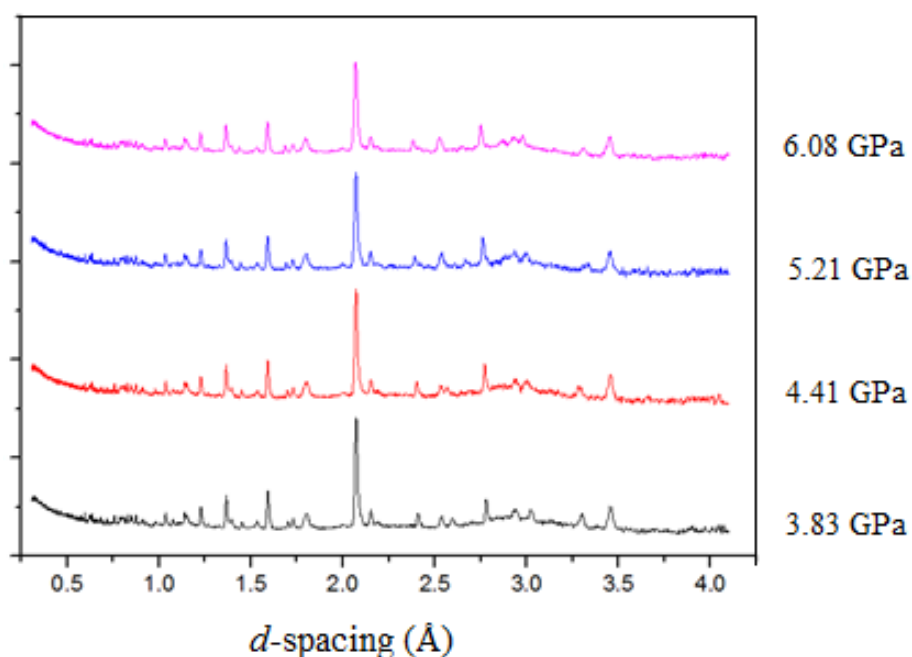


Fig. 6.14 Series of neutron powder diffraction patterns collected during the compression of D- α -3,4-DAT.NTO to a maximum pressure of 6.08 GPa,

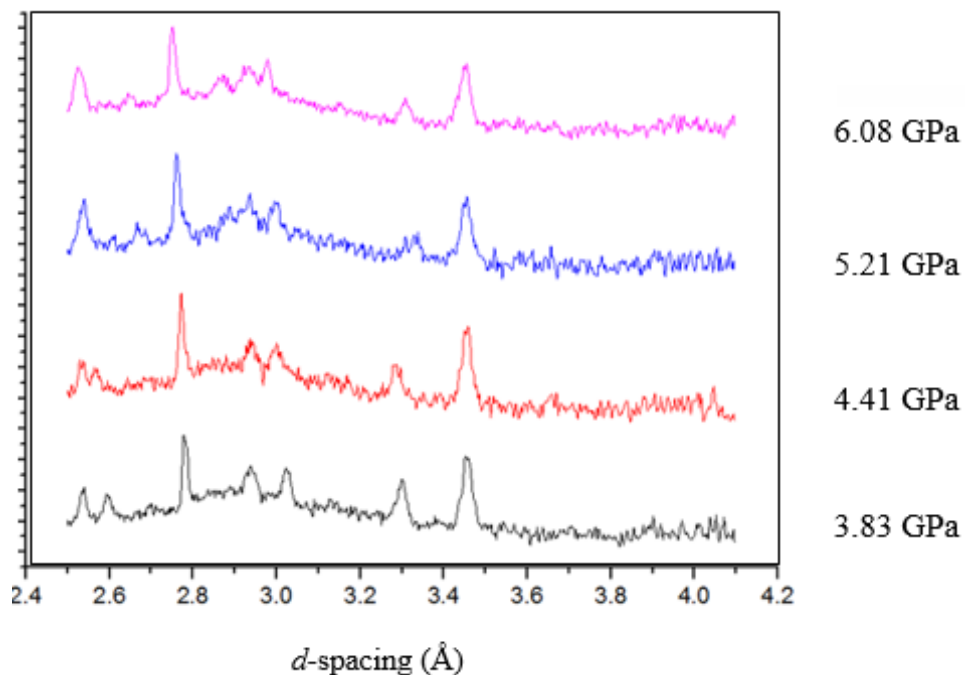


Fig. 6.15 Expanded view of neutron powder diffraction patterns collected during the compression of D- α -3,4-DAT.NTO,

The variations in the unit-cell parameters, are represented graphically in Fig 6.16 and 6.17. The unit cell volume decreases steadily with pressure and has been fitted to a 3rd-order order Birch-Murnaghan equation of state, as shown in Fig. 6.18. The V_0 value was not fixed. The coefficients of the Birch-Murnaghan EoS have been determined as $V_0 = 915.9 \text{ \AA}^3$, $B_0 = 12.6 \text{ GPa}$ and $B'_0 = 6.5$. No decompression study was conducted in this instance, and so no ambient pressure refinement has been obtained. The values for 3,4-DAT.NTO indicate that 3,4-DAT.NTO is slightly less compressible than 3,5-DAT.NTO.

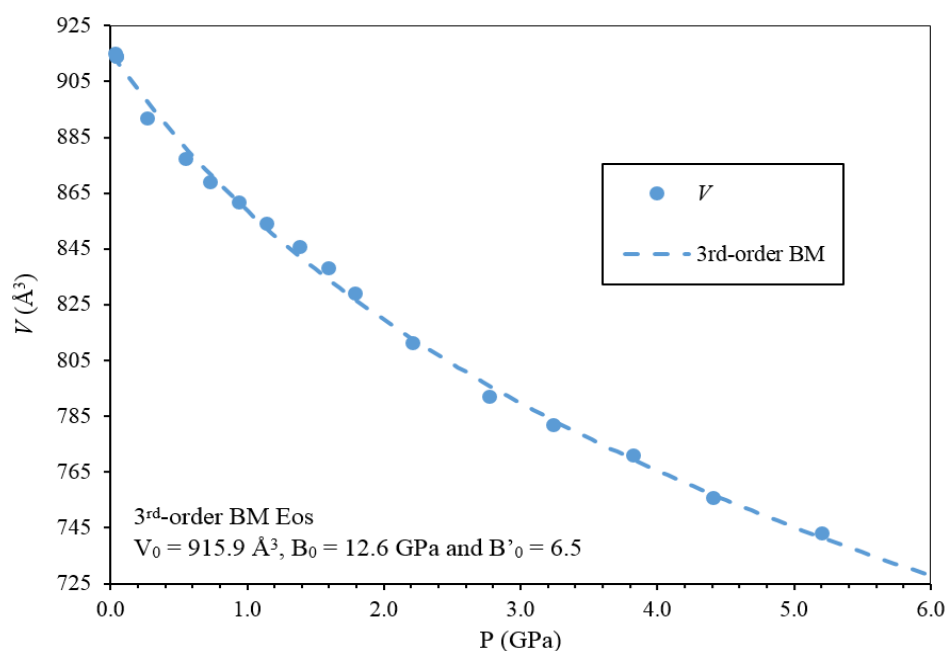


Fig. 6.18 The 3rd-order Birch-Murnaghan EoS that has been fit to the PV -plot for compression of D- α -3,4-DAT.NTO

Fig 6.16 clearly shows the anisotropic behaviour of the lattice parameters, a , b and c . The c -axis is the most compressible axis, $\sim 11.2\%$; whilst both the a - and b -axes are equally compressible at $\sim 6\%$. These observations can be rationalised by reference to the crystal structure, (Fig 6.13), in which there are voids along the c -axis.

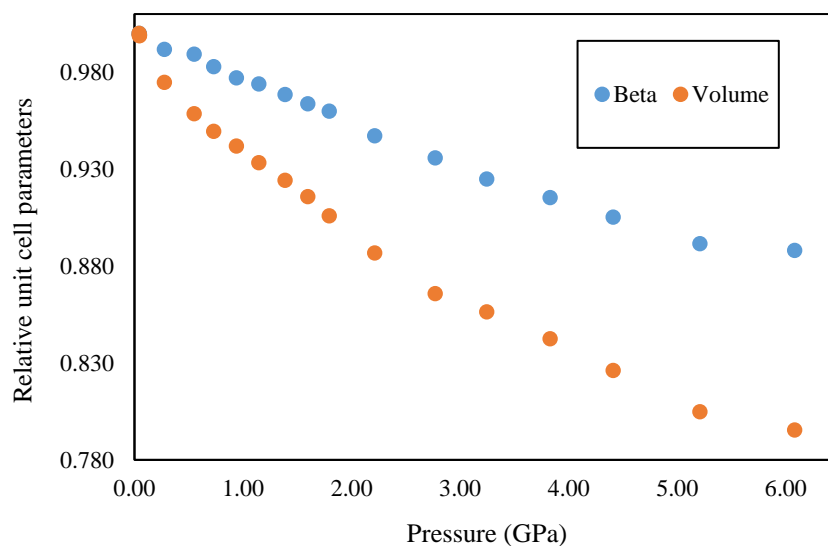


Fig. 6.16 The relative contraction of the unit cell parameters (β angle and volume), normalised to 0 GPa

As illustrated in Figure 6.16, the β angle decreases with pressure. The initial value for β is 91.6° and in 81.3° at 6.08 GPa. As the value decreases with pressure it is worth noting that the value passes through 90° at approximately 0.729 GPa, where the unit cell would formally be classed as an orthorhombic crystal system rather than monoclinic. However, this appears to be a smooth transition and so cannot be classified as a phase transition.

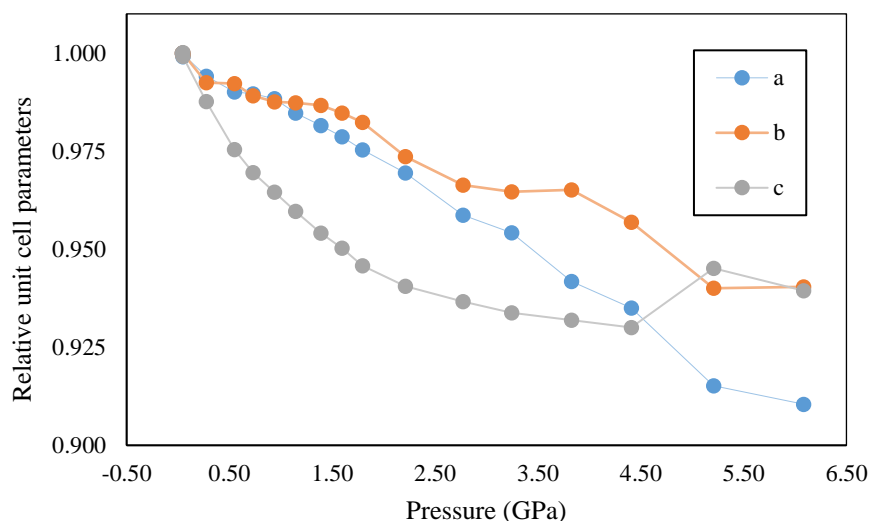


Fig. 6.17 The relative contraction of the unit cell parameters (*a*-, *b*-, *c*-axis), normalised to 0 GPa

6.4 Conclusions

The structural data presented herein represent a significant contribution to understanding of NTO salts under extreme conditions. 3,5-DATNTO and 3,4-DAT.NTO are the first energetic salts of NTO to be studied under high-pressure. Both DAT.NTO salts compress anisotropically, this is unsurprising given the layered structure of 3,5-DAT.NTO and the presence of voids in the structure of 3,4-DAT.NTO. The equation of state for both α -3,4-DAT.NTO and α -3,5-DAT.NTO give the bulk moduli to be 12.6 and 8.2 GPa respectively. In comparison with the bulk modulus of NTO (11.2 GPa), 3,4-DAT.NTO is less compressible and 3,5-DAT.NTO is more so.

A high-pressure phase change of 3,5-DAT.NTO has been observed between 2.18 and 2.37 GPa. This phase remained stable up to the pressure of 5.33 GPa.

However, the new polymorph was not recoverable upon decompression. This phase change was observed in both X-ray and neutron experiments. In addition, the behaviour of both the protonated and deuterated samples of 3,5-DAT.NTO was similar, therefore ruling out any effects of deuteration. It is assumed that form II of 3,5-DAT.NTO has maintained a layered structure and is similar in features to the ambient phase. The transition between both of the layered ambient and high-pressure phase is analogous to that of that displayed in the high-pressure behaviour of FOX-7.

For 3,4-DAT.NTO no phase change was observed for deuterated α -3,4-DAT.NTO up to 6.08 GPa. The compressibility of each axis is similar with c-axis being the most compressible axis, $\sim 11.2\%$ and both the a- and b-axes at $\sim 6\%$.

6.5 Suggestions for Future Work

Suggested work to be completed in the future consists of further compression studies, with a focus on the decompression behaviour of both materials in further detail. Moreover, the decompression of 3,5-DAT.NTO should be conducted at low temperature to see whether the high-pressure phase can be recovered. If the high-pressure phase is recoverable, there is a potential for solving the structure using ambient X-ray methods. An interesting investigation to conduct would be to apply pressure at a different rate, to see whether this alters the EoS data and possibly even the phase change point.

In addition to pressure, variable temperature studies at Diamond Light Source can be performed to potentially find β -3,5-DAT.NTO from α -form, by increasing beta angle within the crystal structure.

Furthermore shock sensitivity testing on both 3,4-DAT.NTO and 3,5-DAT.NTO should be completed to compare with impact sensitivities and crystal structure properties.

6.6 References

1. A. P. Hammersley, *ESRF Internal Report*, 1997, **ESRF97HA02T**
2. A. P. Hammersley, S. O. Svensson, and A. Thompson, *Nucl. Instr. Meth.*, 1994, **A346**, 312-321

3. Agilent (2014). *CrysAlis PRO*. Agilent Technologies Ltd, Yarnton, Oxfordshire, England.
4. R. H. Blessing, *Acta Cryst.*, 1995. **A51**, 1-6
5. P. W. Betteridge, J. R. Carruthers, R. J. Cooper, K. Prout, D. J. Watkin, *J. Appl. Cryst.*, 2003, **36**:1487.
6. J-T. Wu, J-G. Zhang, X. Yin, M. Sun, T-L. Zhang, *Z. Anor. Allg. Chem.*, 2013, **639** (12-13):2354-2358

Summary

In summary, the crystal structures of 13 salts and co-crystals of NTO with a range of non-energetic co-formers were obtained. Two of which were co-crystals of NTO and are the first NTO co-crystals to be reported. NTO co-crystals exhibit distinguishable physical properties, such as colouration (NTO salts are generally yellow, NTO co-crystals are white).

Polymorphism was seen in a salt, 3,5-DAT.NTO, and co-crystal/salt BiPy.NTO. The polymorph of 3,5-DAT.NTO was obtained through high-pressure studies, whilst the salt and co-crystal of BiPy.NTO was gained from different solvents. It is possible to convert between the salt and co-crystal of BiPy.NTO through increasing the temperature to 60°C. It is also suggested that the conversion between polymorphs of BiPy.NTO can occur at low pressures (~ 0.4 GPa), which was seen during impact sensitivity testing. This control and understanding of polymorphs is important. This is especially so when there is a large difference in physical properties, such as impact sensitivity – BiPy.NTO salt is insensitive to impact whilst the co-crystal is very sensitive. Furthermore, comprehension of the stabilities of salts and co-crystals, through high-pressure and high-temperature studies have been obtained.

A selection of co-formers which can interact with nitro-groups have been identified. Strong hydrogen bonding and planar layered structures were observed, in addition to interesting halogen bonding. Within the salts containing N-heterocyclic co-formers, a common hydrogen bond was present between the co-former and NTO. This interaction was observed against ΔpK_a displaying a trend between the two features. With decreasing ΔpK_a produce a salt with reducing hydrogen bond distance between the two co-formers.

Through changing the chemical composition it was possible to alter the oxygen balance and nitrogen content. Other physical properties such as thermal stability, morphology, impact sensitivity, and calculated detonation parameters were also gathered and compared. Appears it was possible to completely alter physical properties. In some salts and co-crystals the impact sensitivity was increased and reduced in comparison to NTO. In one salt the thermal stability was increased to a value greater than pure NTO. Whilst with other the thermal decomposition pathway was greatly reduced and altered.

This work has confirmed the importance of collecting full data on crystal structure and on physical properties of salts and co-crystals, in order to determine trends for design and prediction. With all the information gathered within this work, a suggestion for the ideal NTO co-former is listed:

- High density
- Planar or rigid molecule (ideal for forming layers)
- Multiple nitrogen atoms (tertiary or secondary amines within a ring) with good distance between (such as in piperazine and bipyridine)
- Increased amount of nitrogen and oxygen
- Similar shape to NTO
- Match H-bonding synthons and π -stacking
- Soluble in water or ethanol/methanol. Can be supersaturated.
- Halogens not useful for density but are for unique interactions
- ΔpK_a rule for NTO salts and co-crystals is ~ -0.85 (> -0.85 salt, < -0.85 co-crystal)
- Following the ΔpK_a with H-bond distance can generally estimate N \cdots N distance between NTO and co-former

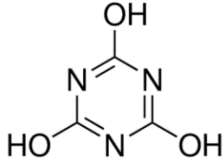
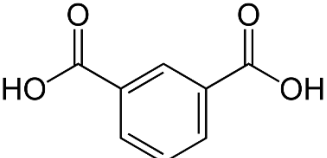
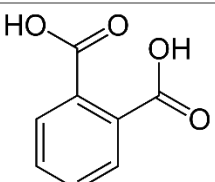
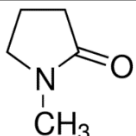
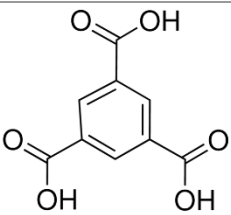
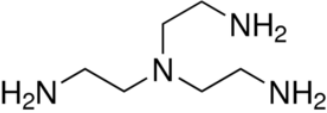
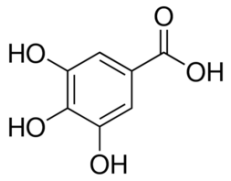
There are still gaps in knowledge and a larger catalogue is required to create further predictive capabilities, however this is the initial step towards this increasingly useful concept. Key future directions include the development of crystal structure predication methods and the advancement of a robust theoretical model for relationship between sensitivity and crystal structure.

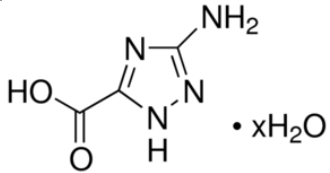
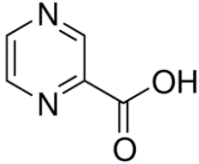
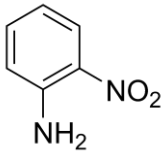
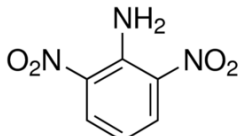
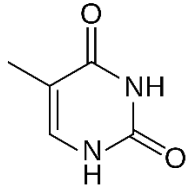
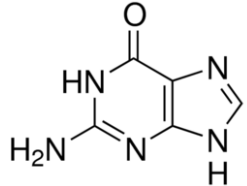
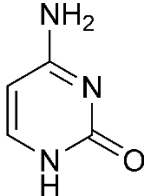
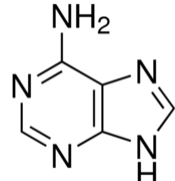
Finally, it is significant to recognize that co-crystallisation of two components that are both energetic (e.g. CL-20/TNT) may not in fact be the optimum strategy for the design of new energetic materials with enhanced properties. The reasoning is as follows. Energetic compounds that are currently used (e.g. HMX, CL-20, TNT, *etc.*) have been developed and optimised for performance on their own (or on occasions as physical mixtures). Whilst co-crystallisation of two of these individual components *may* result in enhancement of properties, this may not necessarily be so. As demonstrated in this work a salt or co-crystal with two components that have *not* been optimised for performance when acting alone, but when combined in a co-crystal they

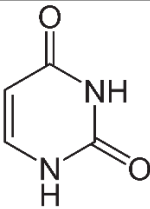
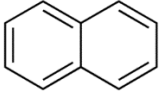
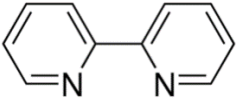
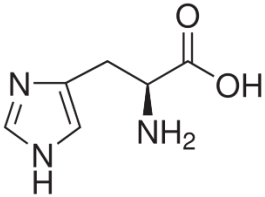
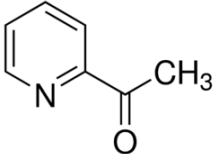
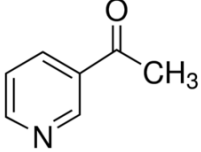
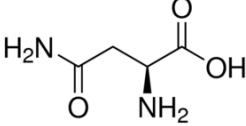
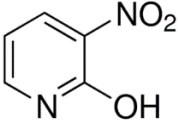
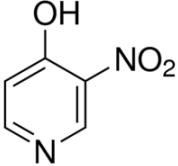
act synergistically and result in a material with properties that are significantly altered. Essentially the overall concept suggests combining two components to give a product that is “more than the sum of its two parts.”

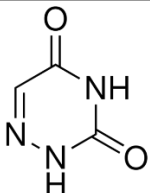
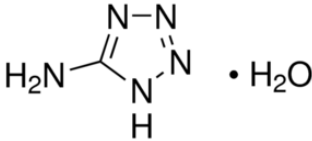
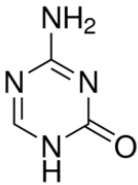
Appendices

Further experimental attempts of NTO with selection of co-formers. All co-formers and NTO were attempted in water, ethanol and methanol. Chloroform, THF, acetone, acetonitrile, ethanol/methanol etc. were used for a variety of co-formers. In addition a selection of temperatures were selected for the evaporation process.

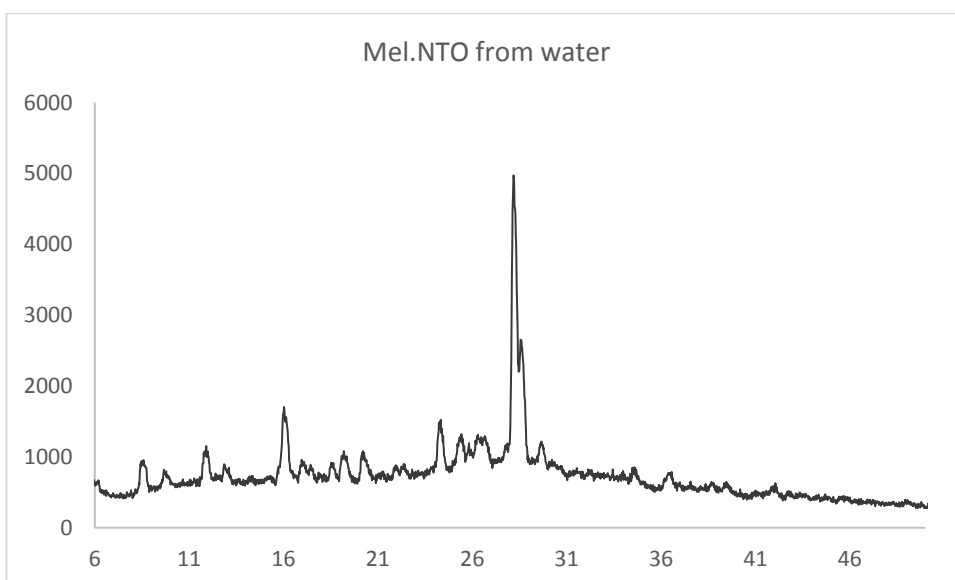
Co-former	Chemical Structure
Cyanuric acid	
Isophthalic acid	
Phthalic acid	
1-Methyl-2-pyrrolidinone	
Trimesic acid	
Tris(2-aminoethyl)amine	
Gallic acid	

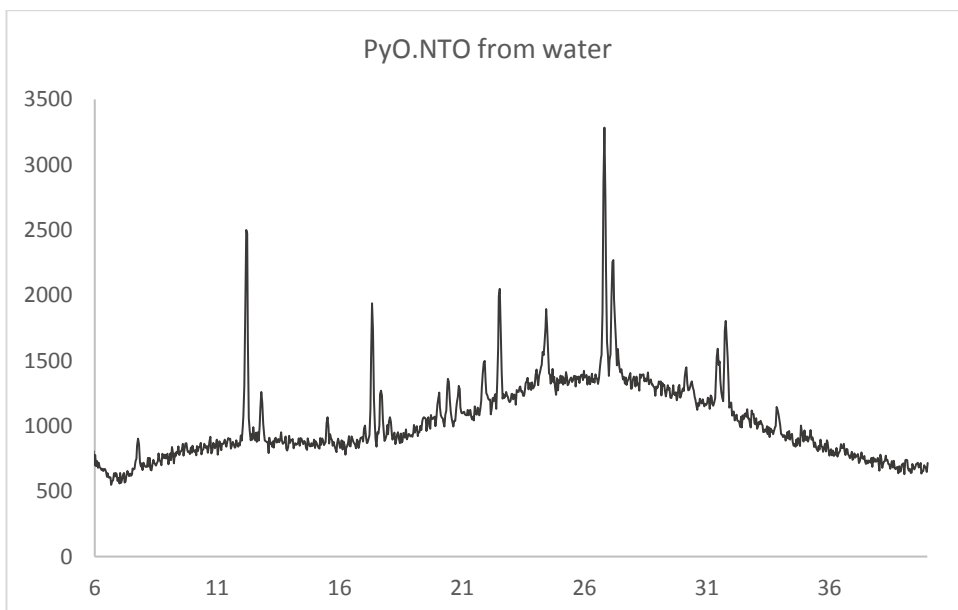
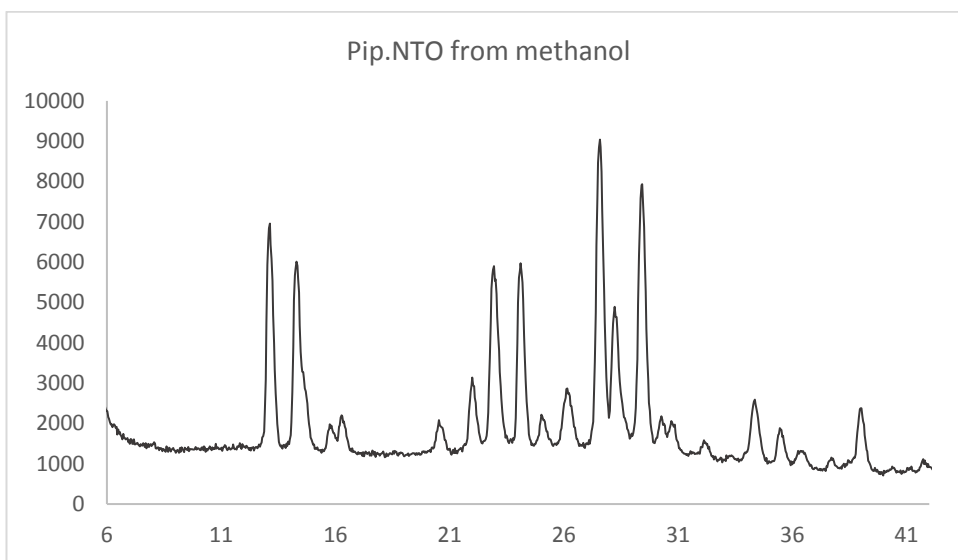
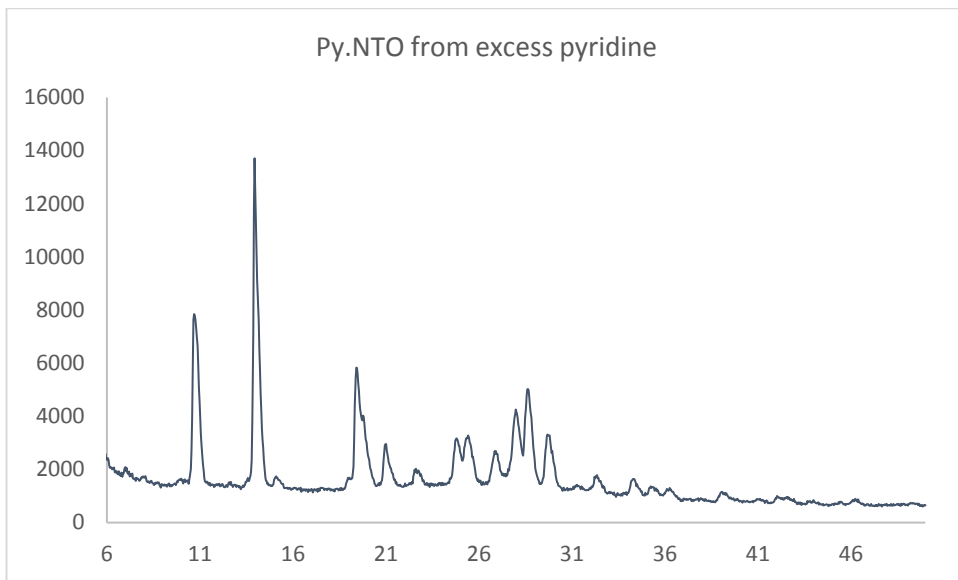
3-Amino-1,2,4-triazole-5-carboxylic acid hydrate	
2-Pyrazine carboxylic acid	
2-Nitroaniline	
2,6-Dinitroaniline	
Thymine	
Guanine	
Cytosine	
Adenine	

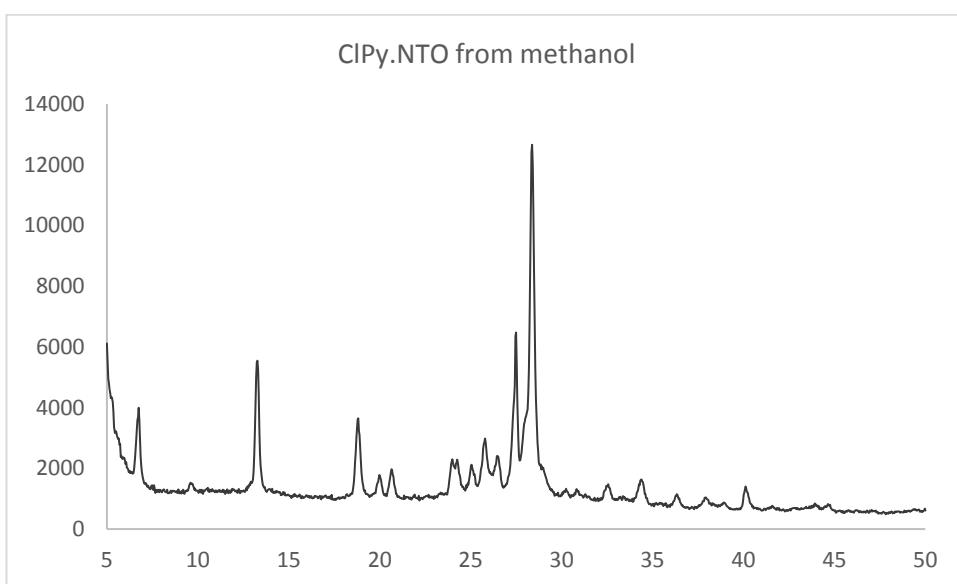
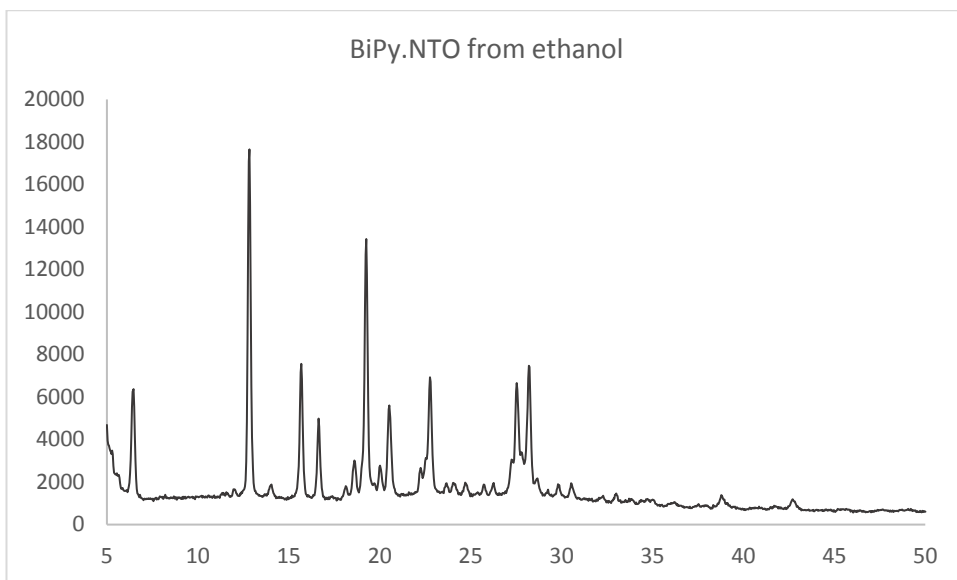
Uracil	
Naphthalene	
2,2-Bipyridine	
L-Histidine	
2-Acetylpyridine	
3-Acetylpyridine	
L-Asparagine	
2-Hydroxy-3-nitropyridine	
4-Hydroxy-3-nitropyridine	

6-Azauracil	
5-Aminotetrazole. monohydrate	
5-Azacytosine	

D2 Powder patterns of materials prior to property testing

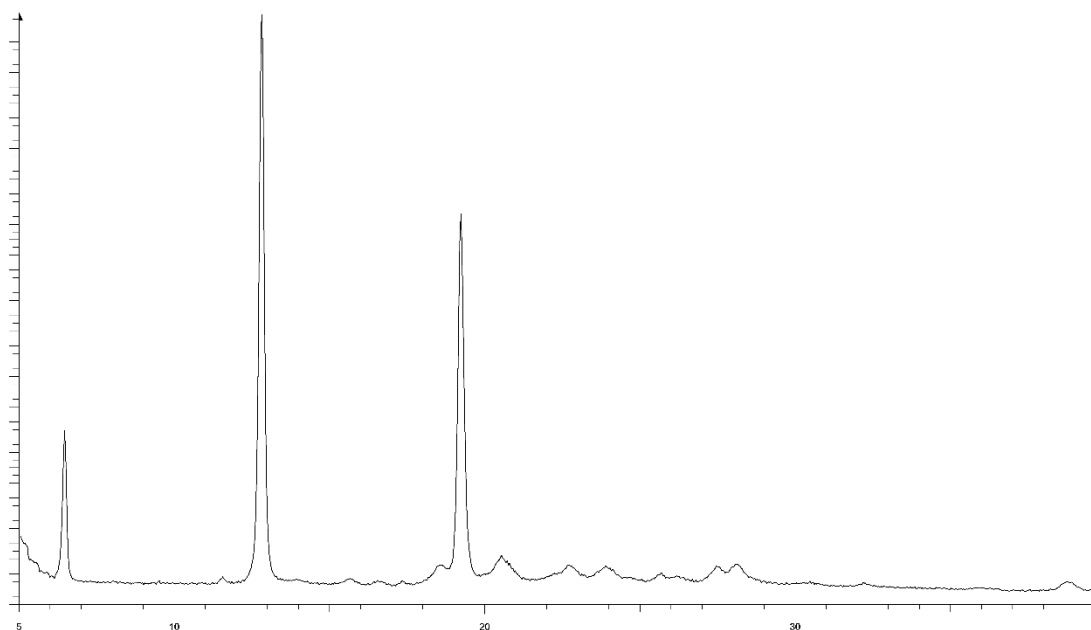






KBr Press powder pattern

BiPy.NTO from ethanol – after application of 8 tonnes of pressure.



Full crystallographic tables

Aniline.NTO	
Empirical formula	C ₈ H ₁₁ N ₅ O ₄
Formula mass /g.mol⁻¹	241.20
Temperature /K	120
Crystal Size /mm	-
Crystal System	Monoclinic
Space Group	<i>P</i> 2 ₁
Z	2
<i>a</i> /Å	5.07368(7)
<i>b</i> /Å	8.22943(14)
<i>c</i> /Å	12.49280(19)
<i>β</i> /°	90.3054
Cell Volume /Å³	521.61
Density calculated / g.cm⁻³	1.536
Absorption coefficient /mm⁻¹	1.076
F(000) / Å	252
Number of reflections [<i>I</i> > 2σ(<i>I</i>)]	1833

Final R₁ and wR₂ [I > 2σ(I)]	0.0234 0.0615
Largest diff. peak and hole /e.Å⁻³	0.13, -0.16
Goodness of Fit	0.9899
Radiation type	Cu

	<i>p</i>-Toluidine.NTO
Empirical formula	C ₉ H ₁₁ N ₅ O ₃
Formula mass /g.mol⁻¹	237.21
Temperature /K	120
Crystal Size /mm	0.026, 0.253, 0.706
Crystal System	Orthorhombic
Space Group	<i>Pca</i> 2 ₁
Z	4
<i>a</i> /Å	10.1104(5)
<i>b</i> /Å	14.9380(7)
<i>c</i> /Å	7.1785(3)
Cell Volume /Å³	1084.16
Density calculated / g.cm⁻³	1.453
Absorption coefficient /mm⁻¹	0.113
F(000) / Å	496
Number of reflections [I > 2σ(I)]	1287
Final R₁ and wR₂ [I > 2σ(I)]	0.0410 0.0952
Largest diff. peak and hole /e.Å⁻³	0.25, -0.29
Goodness of Fit	1.0133
Radiation	Mo

	<i>p</i>-Anisidine.NTO
Empirical formula	C ₉ H ₁₁ N ₅ O ₄
Formula mass /g.mol⁻¹	253.21

Temperature /K	120
Crystal Size /mm	-
Crystal System	Orthorhombic
Space Group	<i>Pbca</i>
Z	8
a /Å	10.4966 (5)
b /Å	6.6750 (3)
c /Å	31.6050 (17)
Cell Volume /Å³	2214.41
Density calculated / g.cm⁻³	1.519
Absorption coefficient /mm⁻¹	0.122
F(000) / Å	1056
Number of reflections [I> 2σ(I)]	2540
Final R₁ and wR₂ [I> 2σ(I)]	0.0508 0.0999
Largest diff. peak and hole /e.Å⁻³	0.38, -0.41
Goodness of fit	1.0555
Radiation	Mo

	2,3-Aminopicoline.NTO
Empirical formula	C ₈ H ₁₀ N ₆ O ₃
Formula mass /g.mol⁻¹	238.20
Temperature /K	150
Crystal Size /mm	powder
Crystal System	Monoclinic
Space Group	<i>P2₁/n</i>
Z	
a /Å	15.767
b /Å	9.237
c /Å	7.074
β /°	77.801

Cell Volume /Å³	1006.93
Density calculated / g.cm⁻³	1.57
Absorption coefficient /mm⁻¹	-
F(000) / Å	-
Final R₁ and wR₂ [I > 2σ(I)]	0.0900
Largest diff. peak and hole /e.Å⁻³	-

	Melamine.NTO
Empirical formula	C ₅ H ₁₀ N ₁₀ O ₄
Formula mass /g.mol⁻¹	274.20
Temperature /K	120
Crystal Size /mm	0.077, 0.153, 0.305
Crystal System	Monoclinic
Space Group	<i>P2₁/m</i>
Z	4
a /Å	9.194 (10)
b /Å	6.137 (7)
c /Å	9.385 (10)
β /°	95.860 (10)
Cell Volume /Å³	526.80
Density calculated / g.cm⁻³	1.729
Absorption coefficient /mm⁻¹	0.148
F(000) / Å	284
Number of reflections [I > 2σ(I)]	1236
Final R₁ and wR₂ [I > 2σ(I)]	0.0750 0.1925
Largest diff. peak and hole /e.Å⁻³	0.33, -0.32
Goodness of fit	1.0648
Radiation	Mo

	Pyridine.NTO
--	---------------------

Empirical formula	C ₇ H ₇ N ₅ O ₃
Formula mass /g.mol⁻¹	209.16
Temperature /K	120
Crystal Size /mm	0.053, 0.021, 0.400
Crystal System	Monoclinic
Space Group	<i>C2/c</i>
Z	8
a /Å	18.618 (16)
b /Å	3.720 (3)
c /Å	25.845 (2)
β /°	103.050 (9)
Cell Volume /Å³	1743.69
Density calculated / g.cm⁻³	1.586
Absorption coefficient /mm⁻¹	0.129
F(000) / Å	864
Number of reflections [I > 2σ(I)]	1559
Final R₁ and wR₂ [I > 2σ(I)]	0.0536 0.1103
Largest diff. peak and hole /e.Å⁻³	0.56, -0.50
Goodness of fit	1.0106
Radiation	Mo

	3-Chloropyridine.NTO
Empirical formula	C ₇ H ₆ N ₅ O ₃ Cl
Formula mass /g.mol⁻¹	243.61
Temperature /K	120
Crystal Size /mm	
Crystal System	Triclinic
Space Group	<i>P1-</i>
Z	2
a /Å	3.665 (2)

<i>b</i> / Å	9.657 (4)
<i>c</i> / Å	13.863 (7)
	102.007 (4)
β / °	95.525 (5)
	100.007 (4)
Cell Volume / Å³	468.61
Density calculated / g.cm⁻³	1.728
Absorption coefficient / mm⁻¹	3.696
F(000) / Å	248
Number of reflections [<i>I</i> > 2σ(<i>I</i>)]	1829
Final R₁ and wR₂ [<i>I</i> > 2σ(<i>I</i>)]	0.0451 0.1302
Largest diff. peak and hole / e.Å⁻³	0.55, -0.43
Goodness of fit	1.0575
Radiation	Cu

	3-Bromopyridine.NTO
Empirical formula	C ₇ H ₆ N ₅ O ₃ Br
Formula mass /g.mol⁻¹	288.06
Temperature /K	120
Crystal Size /mm	
Crystal System	Triclinic
Space Group	<i>P</i> 1-
Z	2
<i>a</i> / Å	6.563 (4)
<i>b</i> / Å	7.016 (4)
<i>c</i> / Å	10.829 (7)
	94.871 (5)
β / °	104.672 (5)
	93.319 (5)
Cell Volume / Å³	478.95

Density calculated / g.cm⁻³	1.997
Absorption coefficient /mm⁻¹	4.293
F(000) / Å	284
Number of reflections [I> 2σ(I)]	2636
Final R₁ and wR₂ [I> 2σ(I)]	0.0239 0.0515
Largest diff. peak and hole /e.Å⁻³	0.63, -0.38
Goodness of fit	0.9640
Radiation	Mo

	Piperazine.NTO
Empirical formula	C ₄ H ₇ N ₅ O ₃
Formula mass /g.mol⁻¹	173.13
Temperature /K	120
Crystal Size /mm	
Crystal System	Monoclinic
Space Group	<i>P2₁/n</i>
Z	4
a /Å	6.666 (3)
b /Å	12.522 (6)
c /Å	8.556 (4)
β /°	108.461 (2)
Cell Volume /Å³	677.42
Density calculated / g.cm⁻³	1.70
Absorption coefficient /mm⁻¹	0.145
F(000) / Å	360
Number of reflections [I> 2σ(I)]	4343
Final R₁ and wR₂ [I> 2σ(I)]	0.0303 0.0837
Largest diff. peak and hole /e.Å⁻³	0.57, -0.30
Goodness of fit	0.9755

Radiation	Mo
------------------	----

	4,4-Bipyridine.NTO
Empirical formula	C ₁₂ H ₁₀ N ₆ O ₃
Formula mass /g.mol⁻¹	286.25
Temperature /K	120
Crystal Size /mm	0.039, 0.047, 0.148
Crystal System	Monoclinic
Space Group	<i>P2₁/n</i>
Z	4
a /Å	7.821 (2)
b /Å	5.786 (1)
c /Å	27.336 (5)
β /°	92.192 (2)
Cell Volume /Å³	1236.07
Density calculated / g.cm⁻³	1.538
Absorption coefficient /mm⁻¹	0.982
F(000) / Å	592
Number of reflections [I > 2σ(I)]	2352
Final R₁ and wR₂ [I > 2σ(I)]	0.0338 0.0892
Largest diff. peak and hole /e.Å⁻³	0.26, -0.28
Goodness of fit	0.9933
Radiation	Cu

	2-Pyridone.NTO
Empirical formula	C ₇ H ₇ N ₅ O ₄
Formula mass /g.mol⁻¹	225.16
Temperature /K	120
Crystal Size /mm	
Crystal System	Monoclinic

Space Group	<i>P2₁/c</i>
Z	4
<i>a</i> / Å	11.810 (9)
<i>b</i> / Å	5.568 (5)
<i>c</i> / Å	14.753 (2)
β / °	104.086 (9)
Cell Volume / Å³	940.99
Density calculated / g.cm⁻³	1.589
Absorption coefficient / mm⁻¹	0.133
F(000) / Å	464
Number of reflections [<i>I</i> > 2σ(<i>I</i>)]	1274
Final R₁ and wR₂ [<i>I</i> > 2σ(<i>I</i>)]	0.0695 0.1620
Largest diff. peak and hole / e.Å⁻³	0.47, -0.49
Goodness of fit	0.9904
Radiation	Mo

	3,5-Diamino-1,2,4-triazole.NTO
Empirical formula	C ₄ H ₇ N ₉ O ₃
Formula mass / g.mol⁻¹	229.17
Temperature / K	120
Crystal Size / mm	0.12 x 0.03 x 0.02
Crystal System	Monoclinic
Space Group	<i>P2₁/c</i>
Z	4
<i>a</i> / Å	3.5501 (2)
<i>b</i> / Å	17.2271 (8)
<i>c</i> / Å	14.6537 (5)
β / °	93.903 (4)
Cell Volume / Å³	894.13 (3)
Density calculated / g.cm⁻³	1.702

Absorption coefficient /mm⁻¹	1.267
F(000) / Å	472
Number of reflections [I > 2σ(I)]	1542
Final R₁ and wR₂ [I > 2σ(I)]	0.0437 0.0378
Largest diff. peak and hole /e.Å⁻³	0.33, -0.32
Goodness of fit	1.0214
Radiation	Cu

	3,4-Diamino-1,2,4-triazole.NTO
Empirical formula	C ₄ H ₇ N ₉ O ₃
Formula mass /g.mol⁻¹	229.19
Temperature /K	120
Crystal Size /mm	0.30 x 0.28 x 0.21
Crystal System	Monoclinic
Space Group	<i>P2₁/c</i>
Z	4
a /Å	12.305 (1)
b /Å	6.095 (2)
c /Å	12.521 (1)
β /°	110.179 (4)
Cell Volume /Å³	881.41 (6)
Density calculated / g.cm⁻³	1.727
Absorption coefficient /mm⁻¹	0.147
F(000) / Å	472
Number of reflections [I > 2σ(I)]	2377
Final R₁ and wR₂ [I > 2σ(I)]	0.0603 0.1551
Largest diff. peak and hole /e.Å⁻³	0.86, -0.48
Goodness of fit	0.9944
Radiation	Mo

